EUROPEAN ORGANIZATION FOR NUCLEAR RESEARCH
(C.E.R.N)

UNIVERSITAT POLITECNICA DE CATALUNYA
(U.P.C)
INSTITUT DE TECNIQUES ENERGETIQUES
(I.N.T.E)

DESIGN AND HIGHER ORDER OPTIMISATION OF FINAL FOCUS SYSTEMS FOR LINEAR COLLIDERS

Doctoral Program in Nuclear Engineering and Ionizing Radiation

Dissertation presented for the degree of Philosophiae Doctor (PhD)

Author:

Eduardo Marin

UPC Supervisor:

Prof. Youri Koubychine

CERN Supervisor:

Dr. Rogelio Tomás

November, 2012

Universitat Politècnica de Catalunya

ACKNOWLEDGMENTS

It is a pleasure to thank those who have contributed to the successful completion of this project. My foremost thanks go to my thesis advisors Yuri Koubychine (UPC-INTE) and Rogelio Tomás (CERN), they have been guiding me with patience and constant support during the last 3 years. Without their help it would have been next to impossible to complete this thesis.

I had the pleasure of working in the Beam Physics Division at CERN. I extensively benefited from the fruitful discussions during the uncountable Beam Physics and CLIC meetings that I have attended.

My heartfelt gratitude to the ATF2 collaboration, who received me with open arms and helped me very much during not only the experimental work at the control room, but also in making my stay in Japan unforgettable (despite the Earthquake). Special thanks go to Philip Bambade and Glen White for their motivation, encouragement and interesting discussions during day and night at ATF2.

I must also thank the CC3 Section at CERN who let me continue my beam based alignment studies at the CTF3 facility during the last year, I appreciate all the help provided by the whole working group, specially to Steffen Doebert and Guido Sterbini.

Most importantly I have to express my deep thankfulness to my wife for her endless support, infinite encouragement and for believing in me all this time.

Contents

List of Figures

List of Tables

Nomenclature

ATF	Accelerator Test Facility
ATF2	Accelerator Test Facility Extension
BBA	Beam-based alignment
BDS	Beam Delivery System
BPM	Beam position monitor
CLIC	Compact Linear Collider
CTF3	CLIC Test Facility
DFS	Dispersion free steering
FD	Final Doublet
FFS	Final Focus System
FFTB	Final Focus Test Beam
ILC	International Linear Collider
IP	Interaction Point
LHC	Large Hadron Collider
QD0	Last defocusing quadrupole magnet before the IP of a FFS
QF1	Last focusing quadrupole magnet before the IP of a FFS
SR	Synchrotron radiation
SVD	Singular value decomposition
TBL	Test Beam Line

Preface

The accelerator and particle physics communities are considering a lepton linear collider as the most appropriate machine to carry out high precision particle physics research in the TeV energy regime. The Compact Linear Collider (CLIC) and the International Linear Collider (ILC) are the two proposals for the future e^+e^- Linear Collider, which are both at the stage of intensive development by two wide international collaborations with strong overlap between them. Both designs achieve a luminosity $\mathcal{L}$ above 10^{34}cm^{-2}s^{-1} at the interaction point (IP), satisfying the particle physics requirements.

The e^+e^- Linear Collider consists of different systems. The Beam Delivery System (BDS) is the last one before the beam arrives at the IP. It comprises of diagnostics, collimation and Final Focus System (FFS) sections. The FFS designs of the CLIC and ILC projects are based on a new local chromaticity correction scheme proposed by P. Raimondi and A. Seryi. This scheme has never been experimentally tested before. In the FFS the beam is focused at the IP by means of two strong quadrupole magnets, the so-called final doublet (FD). To reach the challenging luminosity it is necessary to reduce the horizontal and vertical beam sizes at the IP, σ_x^* and σ_y^* respectively, achieving vertical spot sizes in the order of the nanometres.

The test facilities play an important role in studying the feasibility issues of the e^+e^- Linear Collider projects. For example, the Accelerator Test Facility (ATF) and its extension (ATF2) at KEK (Japan) aim to experimentally verify that the ultra-low beam emittances can be obtained and assess the feasibility of the FFS based on the novel local chromaticity correction scheme. The main goal of the CLIC Test Facility (CTF3) at CERN (Switzerland) is to demonstrate the two beam acceleration scheme in which CLIC is based on.

The present thesis is devoted to the design and high order optimisation of FFS for linear colliders based on the local chromaticity correction scheme. The tuning study of the design lattice determines its feasibility. By tuning we understand the process that brings the system to its design performance in terms of $\mathcal{L}$ and $\sigma_{x,y}^*$ under realistic error conditions. This problem is also one of the subjects of this thesis.

One of the problems studied in this thesis is the optimisation of the crab cavity for the CLIC BDS with $L^*= 3.5$ m design. The design luminosity is $\mathcal{L}_0= 5.9\cdot10^{34}$cm^{-2}s^{-1}. The beams cross each other at the IP forming an angle of 20 mrad in order to provide safe extraction of the spent beams. Due to this crossing scheme the geometric luminosity would be reduced by 90%. Crab cavities are dedicated to tilt the bunches in order to provide head-on like collisions preserving the design $\mathcal{L}_0$. However this solution does not fully recover the design luminosity for the CLIC BDS with $L^*= 3.5$ m design. In this thesis the causes of the observed luminosity loss despite the implementation of the crab cavity are identified, moreover several solutions to recover the CLIC nominal luminosity are proposed.

The ATF2 Nominal and the ATF2 Ultra-low β^* lattices are designed to test the feasibility of the FFS of ILC and to make experiments with a larger chromaticity lattice, comparable to the one of CLIC, respectively. The design IP vertical beam sizes for these lattices are 38 nm and 23 nm respectively, without including any field errors in the model. At this beam size regime the chromatic and geometric aberrations of the beam line may preclude to focus the beam to the required spot sizes. The magnetic field quality of FFS magnets is a concern. The vertical spot size at the IP with the measured multipole components is well above the design value for both lattices. The study of the high order aberrations performed in this thesis is crucial for identifying which multipole components are most relevant for the emittance growth, and exceed their tolerances and for proposing possible solutions. Replacing the FD by better field quality magnets would considerably improve the performance of the ATF2 facility. However the impact of the multipole components of the remaining ATF2 magnets is still noticeable.

Swapping the ATF2 quadrupole magnets according to their skew sextupole component provides some further beam size reduction. Another complementary solution is to modify the lattice optics. The strategy consists in designing a new lattice in which the value of the horizontal β-function at the IP is increased, therefore the horizontal β-function along the beam line is decreased and consequently the impact of the multipole components is minimized. In this thesis a new design ATF2 Bx2.5By1.0 lattice, that features a value of β_x^*= 10 mm is obtained. This lattice was used during the experimental session of ATF2 in December 2010. The new ATF2 Ultra-low β_y^* lattice is proposed for experiments with a vertical chromaticity comparable to that of the CLIC FFS. This new lattice includes a new FD, swapping of the quadrupoles and a increase of the value of β_x^* up to 6 mm. Both new designs effectively minimise the detrimental effect of the multipolar components of the ATF2 magnets reaching a σ_y^* equal to 38 nm and 27 nm respectively.

The tuning studies for the alternative CLIC BDS design with L*= 6 m and the new ATF2 Bx2.5By1.0 and ATF2 Ultra-low β_y^* lattices are also studied in this thesis. The tuning algorithm applied in the case of CLIC comprises orbit correction, dispersion free steering and scanning a set of pre-computed orthogonal knobs. The misalignment errors of the magnets, BPM resolution and the effect of synchrotron radiation are included in the tuning simulations. From the results of the study the critical impact of the quadrupole alignment on the tuning performance is derived. The motion of the magnetic centre when shunting the quadrupole magnet might represent a limiting factor for further improvement of the alignment of the quadrupole magnets. This issue is also addressed in the present thesis. In particular simulations and experimental measurements at the test facilities ATF2 and CTF3 have been performed and their results are discussed.

To study the tuning convergence in case of the ATF2 lattices, a tuning algorithm based on a set of pre-computed orthogonal knobs is used. The errors included in this study are misalignments, tilts and miss-powering of the ATF2 FFS magnets. The simulated tuning results for the ATF2 Bx2.5By1.0 lattice are compared with experimental results obtained during the experimental tuning session of ATF2 in December 2010.

At the present time the CLIC project has recently published its Conceptual Design Report which will be followed by the preparation of the Technical Design Report. In the case of the ATF2 facility, the regular operation of the machine was resumed by the end of 2011 after the big earthquake that occurred in March 2011. Presently the ATF2 team works intensively in order to achieve the design values of the ATF2 Nominal lattice in the near future. The CTF3 accelerator is continuing its operation with the aim to demonstrate the two beam acceleration scheme under the CLIC specifications.

The results of the present thesis have been published in 7 articles in the Proceedings of PAC'09, IPAC'10, IPAC'11, PAC'11 and IPAC'12, and were also presented in talks at 9 international conferences.

Objectives and Structure of the thesis

The general goal of the studies presented in this thesis is to contribute to the development and final demonstration of the Final Focus Systems based on the local chromaticity correction scheme. It is expected that the results derived from this thesis will help to bring the CLIC project and the ATF2 and CTF3 facilities closer to their challenging objectives. To be more concrete, the objectives of the studies carried out in the thesis are the following:

1. Optimization of the implementation of the CLIC crab cavity with the aim to recover the design luminosity,
2. High order optimization of the ATF2 Nominal and Ultra-low β^* lattices in order to minimize the detrimental effect of the multipole components of the magnets,
3. Study of the tuning performance of the CLIC BDS with $L^*= 6$ m design and the ATF2 lattices,
4. Experimental study of the tuning of the ATF2 Bx2.5By1.0 lattice,
5. Study of effects limiting the precision of FFS quadrupole alignment, in particular the motion of the magnetic centre.

In **Chapter 1** an introduction to the main concepts of the future lepton linear colliders is given and motivations and requirements provided by the particle physics community are discussed. A brief description of the main components and principle of operation of the e^+-e^- LCs is given. Special attention is paid to the baseline and alternative designs of the CLIC Beam Delivery System.

The main concepts of beam dynamics that will be used in the studies of the FFS are introduced in **Chapter 2**. Limiting factors to be taken into account in the design of the FFS are discussed and a description of the beam based alignment techniques for aligning quadrupoles is given. In the final section of this chapter a definition of the FFS tuning process is introduced. In addition different tuning algorithms are described in detail.

Chapter 3 is devoted to the description of the Final Focus Test Beam (FFTB), ATF2 and CTF3 test facilities. The FFTB achieved the smallest ever measured vertical beam size σ_y^*. The ATF2 and CTF3 test facilities are of crucial importance to the future LC projects aimed to demonstrate the performance of the novel FFS chromaticity correction scheme and the two beam acceleration concept underlying the CLIC design, respectively.

In **Chapter 4** we address the design and optimization of CLIC and ATF2 lattices. In the case of CLIC, we study the effect of the loss of luminosity related to the crab crossing angle of the beams at the IP and propose different solutions to the problem. This study was carried out using an extended version of the MAPCLASS code developed in the thesis. In the case of ATF2 we analyse the effect of high order aberrations on the IP beam size and present different solutions minimizing the detrimental effect of multipole components of the ATF2 magnets. As a result new ATF2 Bx2.5By1.0 and ATF2 Ultra-low β_y^* lattices were proposed.

Chapter 5 is devoted to tuning simulations of the CLIC and ATF2 lattices. The results are compared with previous studies performed by means of a different tuning algorithm. In the case of CLIC BDS with $L^*= 6$ m a comparison with tuning of the CLIC BDS with $L^*= 3.5$ m is discussed. The study also includes tuning simulations of the new ATF2 lattices using a tuning algorithm based on orthogonal knobs. In the case of the ATF2 Bx2.5By1.0 lattice, experimental tuning results obtained during the session carried out in December 2010 are reported and their detailed comparison to the simulations are discussed.

Chapter 6 is dedicated to the beam based alignment measurements performed at the ATF2 and CTF3 test facilities. Results of two experimental studies of the magnetic centre position are reported. These allow us to estimate the magnetic centre motion with magnet coil current. Results of beam based alignment measurements conducted at ATF2 and CTF3 are given.

Chapter 7 contains a summary of results obtained in the thesis and the most relevant conclusions and considerations.

In the Appendices, complementary information that may help to follow the content of the thesis is given. Appendix A gives the definition of the beam emittance and its relation to the Twiss parameters. In addition the description of the bending, quadrupole and sextupole magnets and their matrix representation can be found. The full set of magnetic centre measurements carried out at ATF2 is given in the Appendix B. It complements the measurements discussed in Section 6.3. In Appendix C a comparison between the characteristics of the QFR300, QFR800 and PXMQMAHNAP35 magnets is made. In addition the conversion from magnet coil current to normalised integrated strength for the mentioned magnets is explained.

1 The future generation of Linear Colliders

During the lasts decades, particle accelerators have become highly effective machines to discover and study new particle physics. They have contributed to the formation and consolidation of the Standard Model of particle physics [1]. However this model is not yet complete, to fill in the missing knowledge experimental data is required. The Large Hadron Collider (LHC) [2] is the world's largest and highest-energy particle accelerator, designed to collide beams with a centre-of-mass energy E_{CM} of 14 TeV and delivering a luminosity $\mathcal{L}$ in the order of 10^{34} $\mathrm{cm}^{-2}\mathrm{s}^{-1}$. The luminosity is the parameter that relates the rate of useful events $\frac{dR}{dT}$ with the cross section σ_p of the process, as it is indicated by the following relation

$$\frac{dR}{dT} = \sigma_p \cdot \mathcal{L}. \tag{1}$$

The scope of the LHC [3] is to help the scientists to better understand the physics beyond the Standard Model. Studies of special interest are: (i) to find the predicted Higgs boson, a key particle that is essential for the Standard Model to work, (ii) to shed light into the understanding of the role of dark matter [4] in the universe, (iii) to study the matter–antimatter imbalance present in the universe and (iv) to seek for evidences of additional spatial dimensions [5].

The precision of the measurement in a hadron colliders is limited due to the fact that the initial energy of the two colliding hadron partons cannot be known. In contrast, in a lepton collider each particle has a well known energy and so precision measurements of interactions are possible. In addition a lepton collider provides cleaner interactions between the beams than the hadron collider.

Among the two possibilities of building either a circular or a linear lepton collider, the circular machines are limited in energy due to the synchrotron radiation emission in the required bending magnets (see Appendix A.2) to close the loop. This energy loss increases the cost of running the machine during its operation. The power emitted by a single particle is:

$$P_\gamma = \frac{2}{3}\frac{e^2 c}{4\pi\epsilon_0}\frac{\beta^4\gamma^4}{\rho_r^2}, \tag{2}$$

where e is the electron charge, ϵ_0 is the electric permittivity of vacuum, β is the relativistic velocity defined as the ratio between the particle velocity v and the speed of light c, γ is the Lorentz factor defined as the ratio between the particle energy and its rest energy (E/m_0c^2) and ρ_r is the bending radius of the particle trajectory. Therefore the emitted power in a circular machine scales as the fourth power of γ and inversely proportional to the square of the machine radius.

The cost of construction and running a circular $\mathrm{C}_{\mathrm{circ}}$ and a linear accelerator $\mathrm{C}_{\mathrm{lin}}$, assuming that the cost of construction is equivalent for both accelerators and goes linearly with the length of the machine l_m by the scale factor a is given by:

$$\mathrm{C}_{\mathrm{circ}} = a \cdot 2\pi\rho_r + b \cdot P_\gamma \tag{3}$$

$$\mathrm{C}_{\mathrm{lin}} = a \cdot l_m, \tag{4}$$

where b is a constant. Figure 1 shows that the energy frontier at which the cost of a linear and a circular machine become comparable is about 200 GeV center-of-mass energy. For higher energies, a lepton circular collider is economically less favourable than a lepton linear collider. Therefore a linear lepton collider is the most efficient facility to study the particle physics at the TeV energy regime with high precision.

The main challenges of a future linear collider are to deliver high beam energies with a single pass

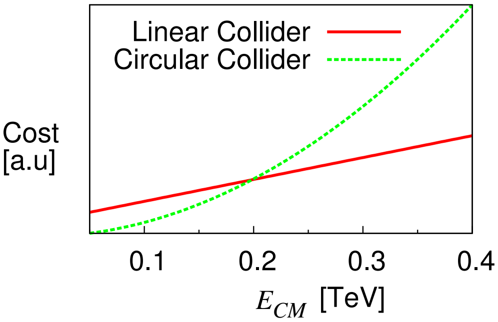

Figure 1: Qualitative illustration of the cost for linear and circular lepton colliders as a function of the centre-of-mass collision energy.

and to achieve a luminosity larger than 10^{34} cm^{-2}s^{-1}. Furthermore the requirement from the physics experiments is that the peak luminosity $\mathcal{L}_{1\%}$, defined as the luminosity within 1% of the energy peak, has to be larger than 10^{34} cm^{-2}s^{-1} [6]. At the TeV energy regime the cross-section of many processes of interest is extremely small. In Ref [7] it is shown that σ_p generally decreases quadratically with the center-of-mass energy. Therefore in order to keep a good event rate large luminosities in the order of 10^{34} cm^{-2}s^{-1} are required.

In general, the luminosity of two colliding beams can be expressed by

$$\mathcal{L} = \frac{N_p^2 \, n_b \, f_{\text{rep}}}{A} \, \mathcal{H}_D, \tag{5}$$

where N_p are the number of particles per bunch, n_b is the number of bunches per train, f_{rep} is the repetition frequency of the trains, the $\mathcal{H}_D$ factor takes into account the luminosity enhancement that eventually occurs when colliding bunches of opposite charge (see Ref. [8]) and A is the effective overlap area between the colliding beams at the IP. Assuming Gaussian bunch distributions, head-on collisions between the bunches and neglecting an eventual offset of the bunches, Eq. (5) can be written as

$$\mathcal{L} = \frac{N_p^2 \, n_b \, f_{\text{rep}}}{4\pi \, \sigma_x^* \, \sigma_y^*} \, \mathcal{H}_D, \tag{6}$$

where σ_x^* and σ_y^* are the horizontal and vertical beam size of the bunch at the interaction point[*], thus by reducing the transverse beam sizes at the interaction point the $\mathcal{L}$ is increased.

1.1 Future e$^+$-e$^-$ Linear Colliders

There exists two proposals for an e$^+$-e$^-$ linear collider, the International Linear Collider (ILC) [9] promoted by a global International collaboration of laboratories and universities, and the Compact Linear Collider (CLIC) led by CERN with an important collaboration with different laboratories and universities worldwide presented in Section 1.2.

The main subsystems of an e$^+$-e$^-$ linear collider are the following:

---

[*] The asterisk over the σ indicates that it is evaluated at the IP

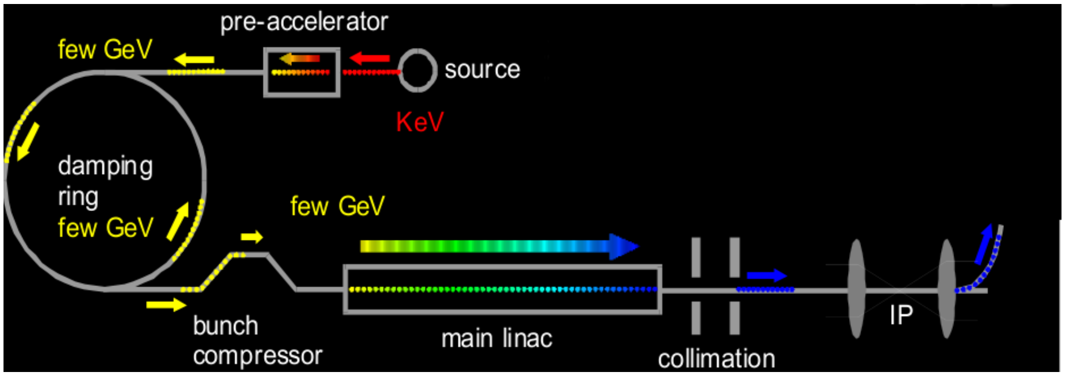

Figure 2: Scheme of a linear collider. The red, orange, green and blue colours correspond to the source, damping ring, main linac and BDS subsystems respectively (Figure taken from [12]).

		Unit	S	DR	ML	BDS
Beam Energy	E	[GeV]	2.86	2.86	1500	1500
Horizontal beam size	σ_x	[nm]	$3{\cdot}10^5$	$3{\cdot}10^4$	$4{\cdot}10^3$	45
Vertical beam size	σ_y	[nm]	$4{\cdot}10^5$	$3{\cdot}10^3$	$4{\cdot}10^2$	1
Luminosity	$\mathcal{L}$	$[10^{34}\mathrm{cm}^{-2}\mathrm{s}^{-1}]$	10^{-9}	10^{-6}	10^{-4}	5.9

Table 1: Approximative values of luminosity, beam energy and transverse beam size at the end of each subsystem of the CLIC linear collider.

1. Source (S): Particles coming from a source are bunched, pre-accelerated and transported in such a way that the beam fits into the dynamic aperture [10] of the Damping Ring.

2. Damping Ring (DR): Its function is to reduce the transverse emittance to the smallest possible value in the shortest time. The emittance is the region occupied by the beam in the phase-space u, u' where u can be the x and y coordinates, a detailed description can be found in Appendix A.1.

3. Main Linac (ML): It increases the energy of the particles up to the final energy keeping the emittance at the lowest possible value.

4. Beam Delivery System (BDS): It is the responsible for performing the beam diagnostics, collimation and transport the beam through the Final Focus System (FFS) towards the interaction point (IP). More details are given in [11].

Figure 2 shows a scheme of an e^+-e^- linear collider where colours red, yellow, green and blue are used to identify its main subsystems. To quantitatively estimate the function of each subsystem, Table 1 summarises the beam energy, beam sizes and luminosity evaluated if the beams would collide after each subsystem. The $\mathcal{L}$ is evaluated considering the CLIC baseline design as the e^+-e^- linear collider and assuming $\mathcal{H}_D$=1 into to Eq. (6). The BDS increases the luminosity by 4 orders of magnitude becoming a key component of the machine to reach a value of $\mathcal{L}$ above 10^{34} $\mathrm{cm}^{-2}\mathrm{s}^{-1}$.

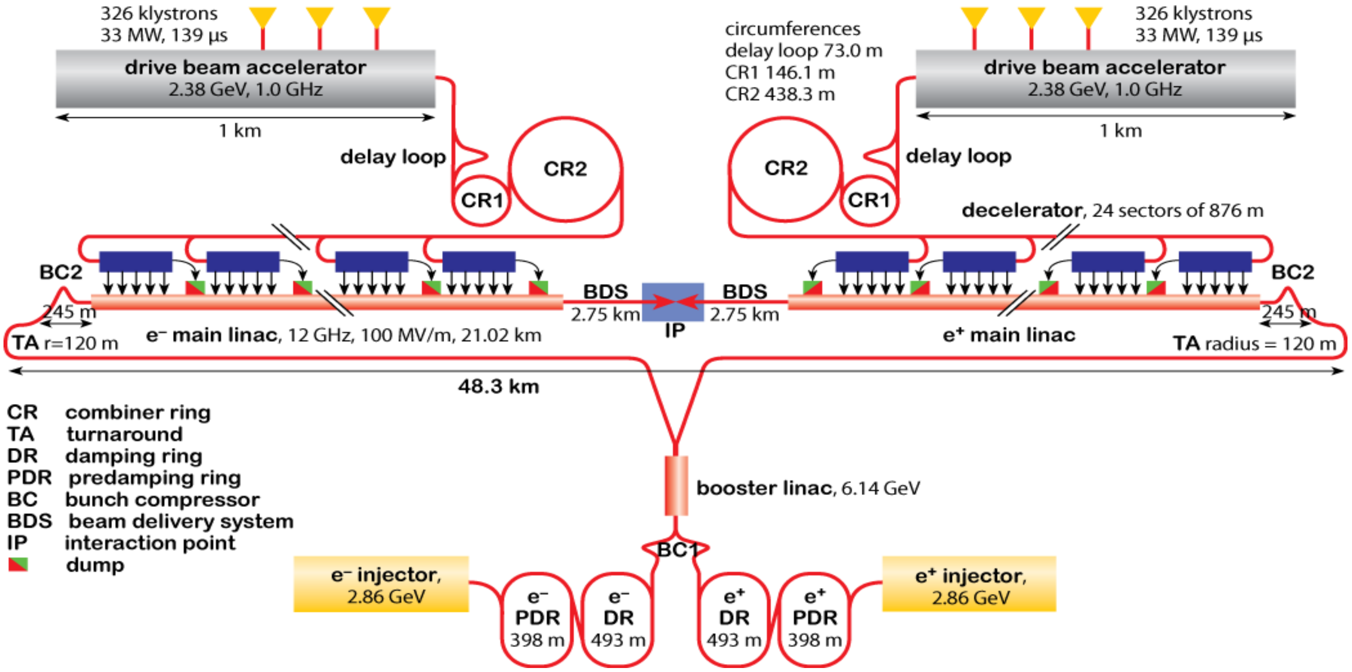

Figure 3: General scheme of the CLIC 3 TeV machine (Figure taken from [14]).

1.2 CLIC Project

The Compact Linear Collider is a proposal of the future generation of linear collider that extends over 48 km. Its goal is to collide e$^+$-e$^-$ beams with a centre-of-mass energy of 3 TeV and delivering a $\mathcal{L}$ above 10^{34} cm^{-2}s^{-1}. The physics potential of CLIC is reported in [6]. A detailed description of the CLIC accelerator baseline design can be found in Refs. [13] and [14].

The two main linacs of CLIC accelerate the beam of electrons and positrons from an energy of about 6 GeV up to 1.5 TeV in a single pass. A large accelerating gradient of 100 MV/m is foreseen to confine the footprint of the machine within a reasonable scale. The accelerating cavities are made of copper. CLIC proposes an innovative two-beam acceleration scheme (Main Beam and Drive Beam). It consists of generating first a high intensity and low energy beam (Drive Beam) that runs parallel to the main beam. The Power Extraction and Transfer Structure (PETS) extracts the radio-frequency power of the Drive Beam to build up the high accelerating gradient at the normal-conducting cavities of the main linac. The high current drive beam is obtained by recombining the bunches coming from the drive beam accelerator. This recombination is done in the delay loop and the combiner rings 1 (CR1) and 2 (CR2). Figure 3 shows a general layout of CLIC and Table 2 summarises the main parameters of CLIC. Each of the CLIC subsystems (S, DR, ML and BDS) is technically challenging and all of them are of vital importance to reach the required luminosity. In this sense, the test facilities are crucial to study the feasibility of the main linac and the beam delivery system. The CLIC test facility (CTF3) [15] is an experimental test facility built at CERN (Switzerland) that aims at demonstrating the feasibility of the two-beam acceleration scheme of CLIC, a detailed description of CTF3 is given in Section 3.3. The Accelerator Test Facilities (ATF and ATF2) are experimental test facilities built at KEK (Japan) meant to address the minimum transverse emittance that can be extracted from the damping ring, and to test the performance of the FFS based on the local chromaticity correction scheme [16].

Parameter	Symbol	Value	Unit
Centre of mass energy	E_{CM}	3.0	[TeV]
Luminosity	$\mathcal{L}$	5.9	[10^{34} cm^{-2}s^{-1}]
Peak Luminosity	$\mathcal{L}_{1\%}$	2.0	[10^{34} cm^{-2}s^{-1}]
Linac repetition rate	$\mathrm{f_{rep}}$	50	[Hz]
Number of particles / bunch	$\mathrm{N_p}$	3.72	[10^9]
Number of bunches / pulse	$\mathrm{n_b}$	312	
Bunch separation	$\Delta \mathrm{t_b}$	0.5	[ns]
Bunch train length	τ_{train}	156	[ns]
Main Linac RF Frequency	f_{RF}	12.0	[GHz]
Beam power / beam	$\mathrm{P_b}$	14	[MW]
Total site AC power	$\mathrm{P_{tot}}$	392	[MW]
Overall two linac length	$\mathrm{l_{linac}}$	42.16	[km]
Proposed site length	$\mathrm{l_{tot}}$	48.4	[km]

Table 2: The main parameters of CLIC.

1.2.1 CLIC BDS

The CLIC BDS consists of three sections: (i) diagnostics, (ii) collimation and (iii) Final Focus System. The diagnostics section measures and corrects the beam characteristics at the exit of the linac in order to avoid any mismatch between the ML and BDS subsystems and to properly transport the beam towards the FFS. More details concerning the diagnostics section can be found in [17].

The function of the CLIC collimation section is to protect the down-stream beam line (FFS) and the detector against miss-steered beams from the main linac and to remove the beam halo that enhances the background level in the detector. A detailed description of the collimation section is given in Ref. [17].

The lattice model of the CLIC beam delivery system can be found in [18].

1.2.1.1 CLIC Final Focus System

The Final Focus System is the last section of the BDS whose main function is to squeeze the horizontal and vertical beam sizes at the IP to the required values. The final part of the FFS is usually formed by a Final Doublet (FD) which is a pair of strong quadrupole magnets (see Appendix A.2) located upstream the IP. They are responsible of focusing the transverse beam sizes at the IP. The length of the drift space between the last magnet of the FD and the IP is called L^*.

The FD focuses the transverse beam size at the IP, moreover the insertion of an octupole and decapole magnets as detailed in [19] is required to deliver beam sizes of 45 nm and 1 nm in the horizontal and vertical planes respectively at the IP. Figure 5 shows the $\sigma_{x,y}$ functions along the CLIC FFS. The energy spread of the incoming beam leads to a noticeable IP beam size growth due to the fact that the FD quadrupoles focus off-momentum particles to different longitudinal position, this effect is referred as chromaticity [20] by analogy with optics. This chromatic effect is corrected by the insertion of sextupole magnets (see Appendix A.2). In order to correct the chromaticity of the lattice two different conceptual designs of FFS have been developed over the last decades. The non-local chromaticity correction scheme corrects the transverse chromaticity by two dedicated chromatic sections, see upper plot in Fig. 4, and afterwards the beam is transported to the final telescope section which demagnifies

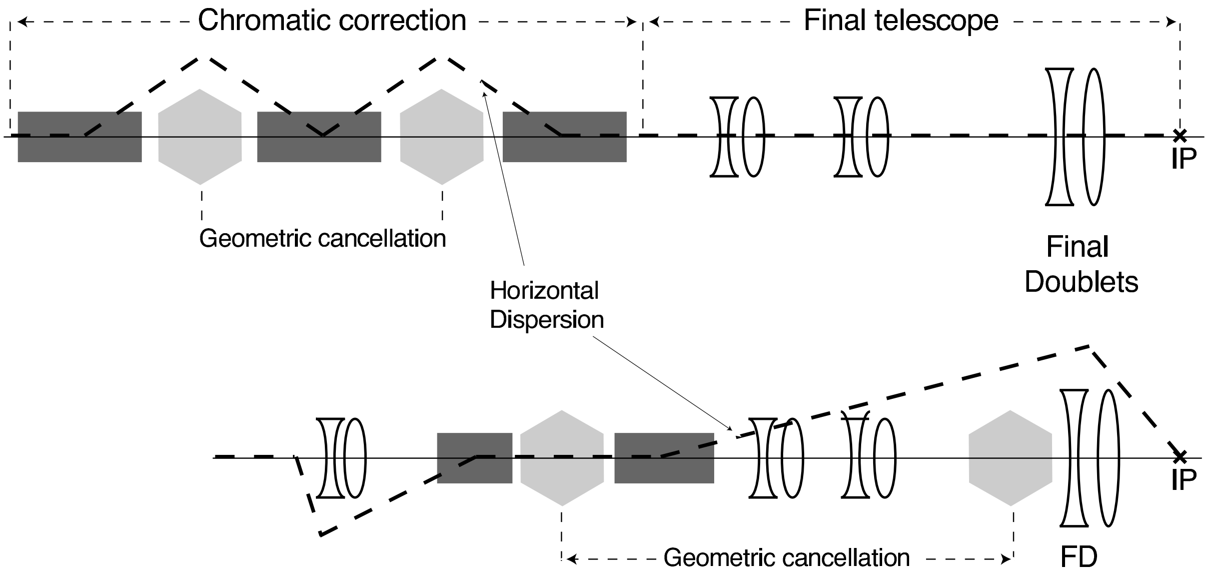

Figure 4: Scheme of the chromaticity correction with sextupoles located at regions of non zero dispersion due to the presence of dipole magnets (see Appendix A.2). Dash lines represent particle trajectories without chromaticity correction, the red and blue continuous lines represent particle trajectories with corrected chromaticity. The upper plot refers to the non-local chromaticity correction scheme, the lower plot shows the local chromaticity correction scheme (Figure taken from Ref [23]).

the beam size. Such scheme was experimentally verified by the Stanford Linear Collider (SLC) [21] and by the Final Focus Test Beam (FFTB) [22] at SLAC.
An alternative design is the local chromaticity correction proposed in [16] with interleaved sextupole magnets in which the FD in order to locally correct the chromaticity. The definition of the chromaticity and details of the local chromaticity correction scheme are given in Section 2.1.3. Figure 4 shows a scheme of both FFS designs.
The e^+ and e^- beams cross at the IP at an angle of 20 mrad to allow the extraction of the beams after collision. To preserve the luminosity obtained by head-on collision, the insertion of a crab cavity is mandatory in order to rotate the bunches at the IP recovering the $\mathcal{L}$. The optimisation of the crab cavity is addressed in this thesis in Section 4.1.
In the baseline design of the CLIC BDS 3 TeV, L^* is equal to 3.5 m. In this configuration the last quadrupole magnet (QD0) is placed inside the detector. To avoid a significant luminosity loss due to ground motion [24] and technical vibrations, the limit for the integrated root-mean-square (rms) [25] vertical displacement was set at 0.2 nm at 4 Hz for the final doublet magnets.
This requirement is extremely challenging if the quadrupole is supported on the detector, therefore it is foreseen to hold QD0 [26] by a cantilever that relies on a massive isolator located in the cavern wall as Fig. 6 shows. With this configuration QD0 avoids the noise from the detector, and vibrates within the tolerances [27].

1.2.1.2 CLIC BDS $L^* = 6$ m

Increasing L^*, as suggested in [29], allows to place QD0 outside the CLIC detector leading to a simpler, robust and stable solution of the interaction region. Different CLIC BDS designs according to L^* have been studied in [30]. Among the possible lattices, the CLIC BDS with $L^*= 6$ m is one

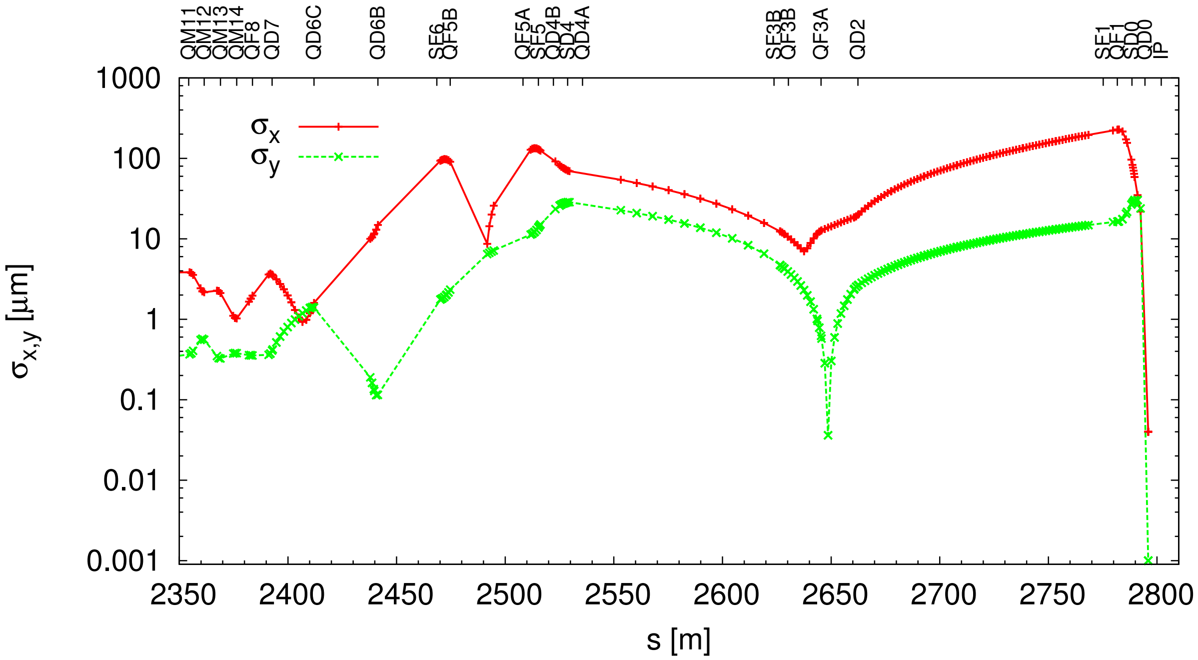

Figure 5: The red and green curves show the horizontal and vertical beam sizes respectively, along the FFS of the CLIC baseline design.

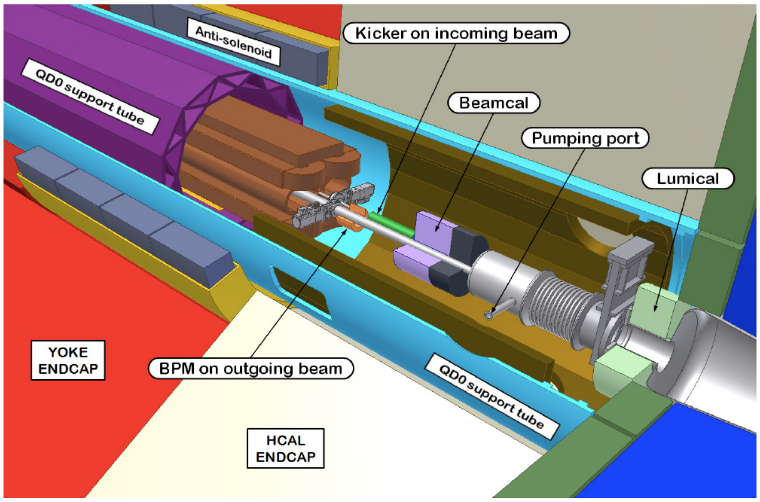

Figure 6: Machine detector interface view for CLIC BDS with $L^* = 3.5$ m, QD0 magnet (brown) is hold by the support tube (blue and violet) that isolates the magnet from the detector (white and red). Complementary elements as the anti-solenoid, kicker, beamcal, pumping port, lumical and BPM are required for other purposes (Figure taken from [28]).

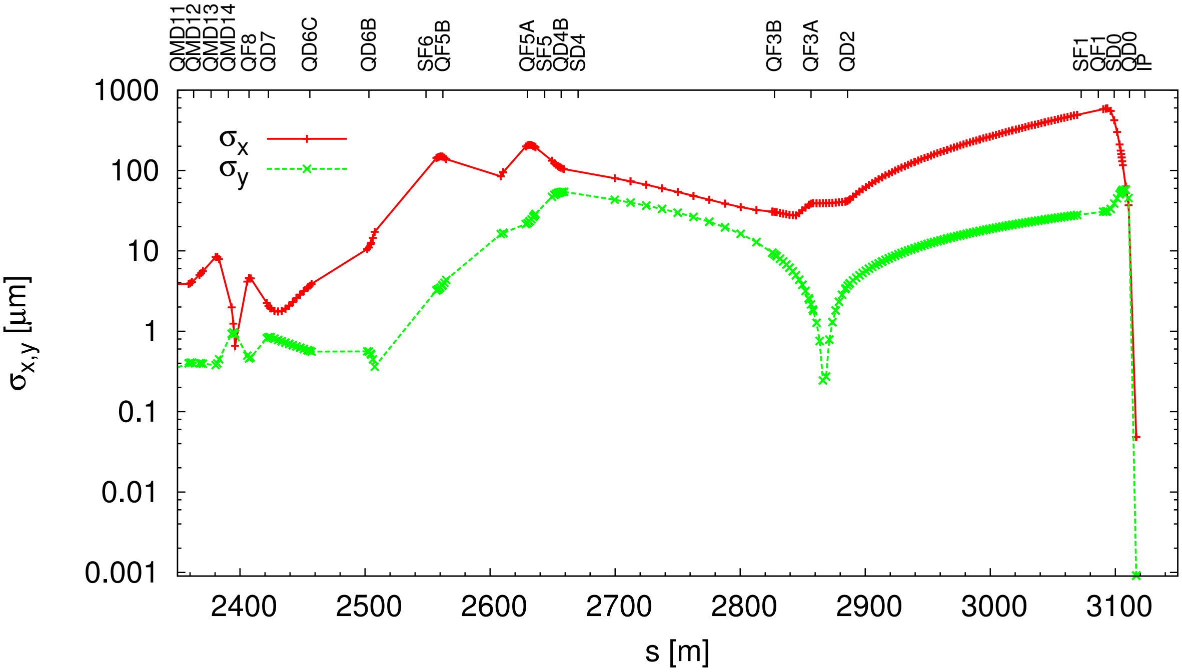

Figure 7: The horizontal (red) and vertical (green) beam sizes along the FFS of the CLIC BDS $L^* = 6$ m design.

of the most attractive solution in terms of performance. The design and optimisation processes of the CLIC BDS with $L^*= 6$ m are reported in Ref. [31]. The lattice model is available at the web repository of CLIC [32]. This design is an alternative BDS of the CLIC baseline design.

The obtained beam sizes at the IP for the CLIC BDS $L^* = 6$ m design are 57 nm and 1.1 nm in the horizontal and vertical planes, respectively, 26% and 10% larger than σ_x^* and σ_y^* for the CLIC BDS with $L^*= 3.5$ m respectively. Figure 7 shows the beam sizes along the CLIC FFS with $L^*= 6$ m. According to Eq. (6) the luminosity for the CLIC BDS $L^* = 6$ m design is smaller than the baseline design due to the larger IP beam sizes, however the peak luminosity still satisfies the requirements from the physics experiments defined in [6]. Table 3 summarises the main parameters of the alternative lattice.

The CLIC BDS $L^* = 6$ m is kept as a fall-back solution of the CLIC BDS baseline design. The feasibility performance of the alternative solution is addressed in Section 5.1.1 of the present thesis. The luminosity for the CLIC BDS baseline design is $5.9{\cdot}10^{34}$ cm^{-2}s^{-1}. Table 3 summarises the main parameters of the CLIC BDS baseline.

			CLIC L*= 3.5 m	CLIC L*= 6 m
Centre of mass energy	E_{cm}	[TeV]	3.0	3.0
Luminosity	$\mathcal{L}$	10^{34} cm^{-2}s^{-1}	5.9	5.0
Peak Luminosity	$\mathcal{L}_{1\%}$	10^{34} cm^{-2}s^{-1}	2.0	2.1
Diagnostic section length	$l_{\rm diag}$	[km]	2 x 0.37	2 x 0.37
Collimation system length	$l_{\rm coll}$	[km]	2 x 1.92	2 x 1.92
Final Focus system length	$l_{\rm FFS}$	[km]	2 x 0.46	2 x 0.67
Normalised horizontal emittance	$\gamma\epsilon_x$	[nm rad]	660	660
Normalised vertical emittance	$\gamma\epsilon_y$	[nm rad]	20	20
Horizontal IP beam size before pinch	σ_x^*	[nm]	45	57
Vertical IP beam size before pinch	σ_y^*	[nm]	1.0	1.1
Bunch length	σ_z	[μm]	44	44
RMS Energy spread	Δ_p	[%]	0.29	0.29
Crossing angle at IP	$\theta_{\rm c}$	[mrad]	20	20

Table 3: The main parameters of the CLIC BDS baseline design and the alternative solution with L* = 6 m.

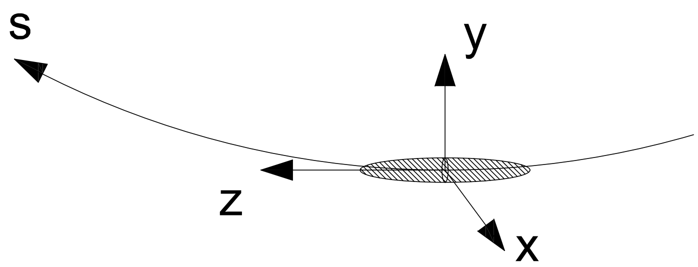

Figure 8: Illustration of the coordinate system used to describe the motion of an ensemble of particles.

2 Beam dynamics in a Final Focus System

2.1 Basic concepts of transverse beam optics

This section contains the main beam dynamics concepts which are extensively used throughout this thesis. Figure 8 shows an illustration of the coordinate system. Each particle at any location along a beam transport line is represented by a point in a six-dimensional phase space co-moving with the reference particle with coordinates x, x', y, y', z and δ_p, where x, y and z coordinates refer to the horizontal, vertical and the longitudinal coordinates respectively. The x' and y' coordinates are the horizontal and vertical slopes defined as $x' = \frac{dx}{ds}$ and $y' = \frac{dy}{ds}$ respectively, being s the distance along the reference trajectory. The relation between s and z is given by $z = s - \int v(t)dt$ where $v(t)$ is the reference particle velocity. Hence z measures deviations on the longitudinal coordinate with respect to the reference particle. Typically in a drift space, a quadrupole magnet or even a higher order multipole magnet the z direction and the s coordinate coincide, but inside of a bending magnet the coordinate s is curvilinear with a radius of curvature ρ_r, while the z coordinate is rectilinear and tangent to the reference trajectory.

The δ_p coordinate refers to the particle momentum deviation normalised to the ideal momentum p_0. The reference particle is the particle with the ideal momentum and describes the reference trajectory.

2.1.1 Twiss functions

The motion of an ensemble of particles along the beam line is usually described by the Twiss functions $\beta_{x,y}(s)$, $\alpha_{x,y}(s)$, $\gamma_{x,y}(s)$ and $\varphi_{x,y}(s)$, the dispersion function, $\eta_{x,y}(s)$, and its derivative $\eta'_{x,y}(s)$ which are defined in [10]. The horizontal and vertical emittances $\epsilon_{x,y}$ are defined as the area occupied by the beam in the phase spaces (x, x') and (y, y') over π respectively. The normalised emittance ϵ_N is defined as $\epsilon_N = \gamma \cdot \epsilon$ where γ is the Lorentz factor.

The $\beta_{x,y}(s)$ functions characterize the envelope of the beam, while $\alpha_{x,y}(s)$ refers to the divergence of the beam as described by equation (see [10]):

$$\alpha_{x,y}(s) = -\frac{1}{2}\frac{d\beta_{x,y}(s)}{ds}, \tag{7}$$

Appendix A.1 shows the relation between the Twiss functions, beam correlations and the emittances. The dispersion takes into account the effect of different deflection of the particles with energy deviating from the reference energy. The product $\delta_p\ \eta_{x,y}(s)$ determines the offset of the off-momentum particle from the reference trajectory. The x and y coordinates of an off-momentum particle are related to the Twiss functions as (see [10]):

$$x(s)_{(p\neq p_0)} = \sqrt{\hat{\epsilon}_x\beta_x(s)}\cos(\varphi_x(s)+\phi_x)+\delta_p\,\eta_x(s), \tag{8}$$

$$y(s)_{(p\neq p_0)} = \sqrt{\hat{\epsilon}_y\beta_y(s)}\cos(\varphi_y(s)+\phi_y)+\delta_p\,\eta_y(s), \tag{9}$$

where $\hat{\epsilon}_x$, $\hat{\epsilon}_y$ are the single particle emittance, ϕ_x and ϕ_y are the initial phases at s=0. The phase function $\varphi_{x,y}(s)$ is related to the $\beta_{x,y}(s)$ function as (see Ref. [10]):

$$\varphi_{x,y}(s) = \int_0^s \frac{d\hat{s}}{\beta_{x,y}(\hat{s})}. \tag{10}$$

Neglecting the synchrotron radiation present in a FFS, more details are gjven in Section 2.1.4, the particles travel under the influence of conservative forces. In this scenario Liouville's theorem [33] ensures that the density of the particles in the 6-dimensional phase space remains constant.

2.1.2 Beam size

If the particle distribution of the beam is represented by a Gaussian distribution in all 6 coordinates, the contributions to the beam size from different sources add in quadrature. The expected beam size $\sigma_{x,y}$ from the Twiss parameters is given by

$$\sigma_{x,y}(s) = \sqrt{\epsilon_{x,y}\beta_{x,y}(s)+\Delta_p^2\,\eta_{x,y}^2(s)}, \tag{11}$$

where $\epsilon_{x,y}$ are the emittances that contains 1σ of the Gaussian particle distribution of the beam and Δ_p is the relative energy spread of the beam. Nevertheless different beam size definitions may be of interest depending on the purpose of the study, in this sense the core of the beam is of special interest when referring to linear colliders, since it is the part of the beam that largely contributes to the luminosity. The Shintake beam size is used when referring to the vertical beam size at the IP obtained by a laser-interferometer or Shintake monitor [†] [34], this monitor is based on a laser interferometer [35] capable of measuring the transverse beam size by the modulation of the generated Compton signal when the electron beam is scanned by the laser interference pattern, more details are given in Section 2.1.2.1. The last beam size definition introduced in this thesis is the rms beam size $\sigma_{\rm rms}$ defined as the root mean square of the particle distribution. In the following a description of how the beam size is evaluated for the three definitions is given:

- CORE ($\sigma_{\rm core}$): Defined as the Gaussian σ obtained from the Gaussian distribution fitted to the histogram of a bunch of particles. The beam size error is the given error by the fit.
- SHINTAKE ($\sigma_{\rm Shi}$): Defined from the convolution between the bunch of particles and the interference pattern of the laser. Details can be found in Section 2.1.2.1.
- RMS ($\sigma_{\rm rms}$): It is evaluated as:

$$\sigma_{\rm rms} = \sqrt{\int_{-\infty}^{\infty}(u-\bar{u})^2\,\rho\,d\nu}, \tag{12}$$

where u stands for x, x', y, y' and ρ is the particle density distribution.

[†] A Shintake monitor is installed at the test facility ATF2 (see Section 3.2.1)

The σ_{core} is the smallest value of the three beam size definitions because it almost neglects the tails of the bunch, while σ_{rms} is the largest beam size because it takes into account the tails of the bunch. The three beam size are usually sorted as:

$$\sigma_{\mathrm{core}} \ \leq \ \sigma_{\mathrm{Shi}} \ \leq \ \sigma_{\mathrm{rms}}, \tag{13}$$

the equalities is satisfied when the beam can be represented by a Gaussian distribution, that occurs if the beam size expected from the Twiss parameters equals the σ_{rms}. The presented beam size definitions are widely used in this thesis. According to Eq. (11) the beam sizes at the IP are minimised by reducing the β-functions at the IP, $\beta^*_{x,y}$. To this end, the FD is a combination of a focusing and a defocusing quadrupole such that both β-functions are minimised at the IP. The behaviour of the β-function along the drift space between the FD and the IP is described by the known formula (see Ref. [36]):

$$\beta(s) = \beta_0 - 2\alpha_0 s + \gamma_0 s^2, \tag{14}$$

where β_0, α_0 and γ_0 are the initial conditions of the Twiss functions at the entrance of the drift space. The β-function is minimal, $\beta^*_{x,y}$, at the waist position ($s_w = \frac{\alpha_0}{\gamma_0}$), where $\alpha_{x,y}(s)$ is 0. Taking into account that $\gamma = \frac{1+\alpha^2}{\beta}$ is constant in a drift space, Eq. (14) can be written as:

$$\beta_{x,y}(s) = \beta^*_{x,y} + \frac{(s - s_w)^2}{\beta^*_{x,y}}. \tag{15}$$

The smaller the value of $\beta^*_{x,y}$ is, the larger the value of $\beta_{x,y}(s)$ is at the final doublet. As an example, the L* and β^*_y of the CLIC baseline design are 3.5 m and 0.07 mm respectively, therefore β_y at the FD is of the order of 100 km. Figure 9 shows the β-functions along the FFS of CLIC.
A limiting factor when reducing the β^*_y arises from the so-called *Hourglass* effect, see Ref. [37]. Beams with a bunch length larger than β^*_y experience an increase of the effective transverse beam size due the growth of the β-function near the waist as shown by Eq. (15) leading to a luminosity reduction. Therefore it is important to satisfy the condition $\frac{\sigma_z}{\beta^*_y} \leq 1$, as an example the CLIC BDS baseline design $\frac{\sigma_z}{\beta^*_y} \approx 0.6$.
Other limiting factors of a FFS are the Oide effect and the high order aberrations of the beam, which are discussed in Section 2.1.3.

2.1.2.1 Shintake monitor algorithm

The vertical beam size at the IP is measured by a laser wire monitor at the ATF2 facility as described in Section 3.2.1. The measurement depends on the beam and the laser profiles, and eventually may differ from the σ^*_{core} and σ^*_{rms} values defined in 2.1.2. Developing and algorithm that reproduces as close as possible the experimental measurement of the Shintake monitor allows to optimise the ATF2 FFS according to the Shintake monitor reading.
The principle behind the operation of the Shintake monitor can be found elsewhere [34] and [35]. It is based on the modulation of the Compton signal M_C generated by the interaction between the particle beam and the interference pattern of photons. The laser beam of wavelength λ_{ls} is split into two by a mirror, both laser beams are transported and cross each other at an angle θ_{ls} at the IP, forming an interference pattern characterised by its fringe pitch d_{pp} as the period between two consecutive peaks or equivalently its wave number k_y. Figure 10 shows the operation principle of the laser interferometer monitor.

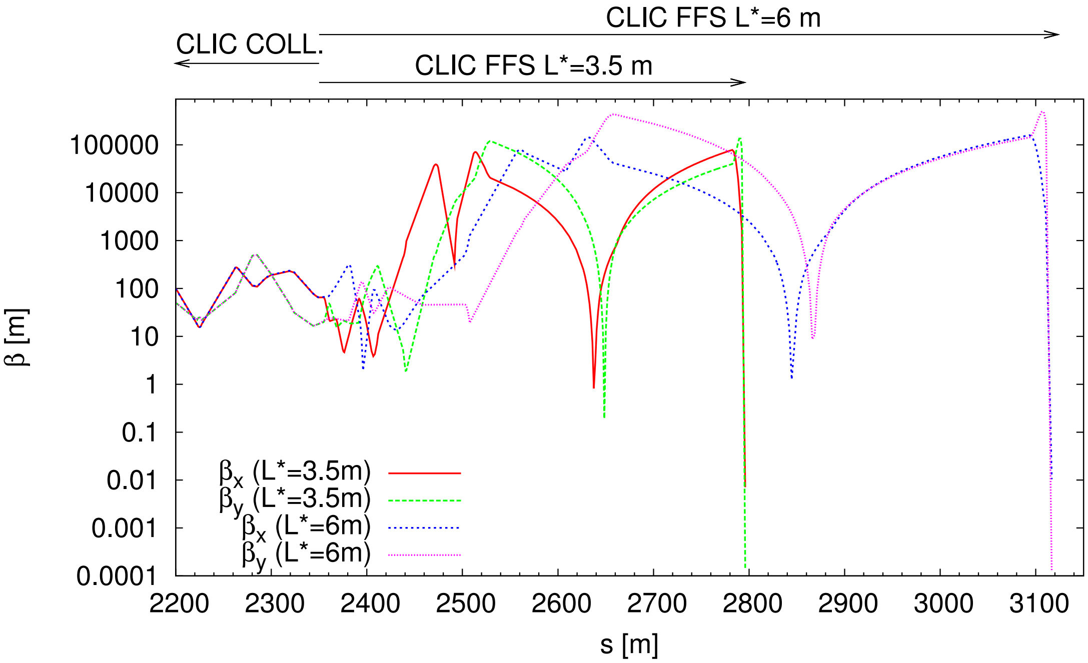

Figure 9: Comparison between the β-functions along the FFS of CLIC which starts after the CLIC collimation section (CLIC COLL) at position s= 2356 m. The read and green curves show the horizontal and vertical β-function for the CLIC BDS L*= 3.5 m scenario, while the blue and magenta curves show the horizontal and vertical β-function for the CLIC BDS L*= 6 m scenario.

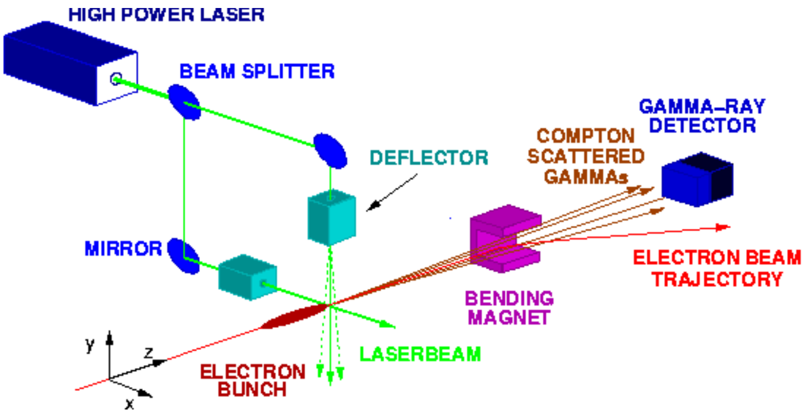

Figure 10: Scheme of the operation principle of a laser wire monitor (Figure taken from [34]).

The relation between $d_{\rm pp}$, k_y, $\lambda_{\rm ls}$ and $\theta_{\rm ls}$ is given by the following relation:

$$d_{\rm pp} = \frac{\pi}{k_y} = \frac{\lambda_{\rm ls}}{2\sin\left(\frac{\theta_{\rm ls}}{2}\right)}. \tag{16}$$

The intensity of the laser interference fringe at the IP can be written by (see Ref. [35]):

$$I_{\rm ls}(y) = 1 + \cos{(\theta_{\rm ls})}\cos(k_y\, y). \tag{17}$$

The experimental measurement consists of scanning the particle beam with the interference pattern of photons by moving the vertical position of the interference pattern by changing the relative phase between the two split laser beams. If the transverse particle beam size is smaller than the fringe pitch, the number of scattered photons at the peak of fringe $N_{\rm max}$ and that at the valley $N_{\rm min}$ differ significantly. However if the transverse beam size is larger than the fringe pitch, it interacts with the the peak and valley at the same time, leading to almost no variation of the numbers of scattered photons when scanning the beam ($N_{\rm max} \approx N_{\rm min}$). The modulation depth of the Compton can be calculated as:

$$M_C = \frac{N_{\rm max} - N_{\rm min}}{N_{\rm max} + N_{\rm min}}. \tag{18}$$

The electron beam size measured by the Shintake monitor $\sigma^*_{\rm Shi}$ can be obtained as a function of the modulation depth, the wave number and the crossing angle of the laser beams according to (derived in Ref. [35]):

$$\sigma^*_{\rm Shi} = \frac{1}{k_y}\sqrt{\frac{1}{2}\ln\left(\frac{|\cos\theta_{\rm ls}|}{M_C}\right)}. \tag{19}$$

In the following a description of the developed Shintake algorithm is given. The algorithm is written in Python and it requires two arguments, (i) the value of σ^*_y and (ii) a file containing the particles position at the IP. σ^*_y is pre-computed by the MAPCLASS code [38] and it is used to select the most appropriate $\theta_{\rm ls}$ to construct the interference pattern of photons that maximises the value of M_C, according to Fig. 11. The distribution of photons $I_{\rm ls}$ is constructed according to Eq. (17). The distribution of particles along the y coordinate is obtained from the file which contains the particles positions. Both distributions are divided into bins of width $b_w = \Delta y / n_{\rm bins}$ where Δy is chosen as the maximum width of the particle distribution. $n_{\rm bins}$ is the number of bins used in the simulation. The algorithm computes the convolution between the distribution of the interference pattern of photons with the distribution of particles. The values of $N_{\rm max}$ and $N_{\rm min}$ are obtained from the convolution, which leads to the evaluation of M_C and σ^*_y according to Eqs. (18) and (19) respectively.

The Shintake monitor installed at ATF2 allows to continuously change the crossing angle of the lasers from $\theta_{\rm ls}$= 2 to 8 degree by fine motion of its mirrors. This capability allows a beam size measurement that ranges from 6 μm to 360 nm considering a $\lambda_{\rm ls}$= 532 nm. Moreover there exists two additional operation modes according to the crossing angle of the laser beams. An intermediate crossing angle of $\theta_{\rm ls}$= 30 degree permits the adjustment of the fringe pitch to the current beam size during the process of tuning that goes from 360 nm down to 100 nm, for smaller beam sizes the $\theta_{\rm ls}$= 174 degree mode provides a suitable fringe pitch to measure beam sizes that range from 100 nm to 25 nm. Table 4 summarises the beam size regime for each operation mode of the Shintake monitor, assuming

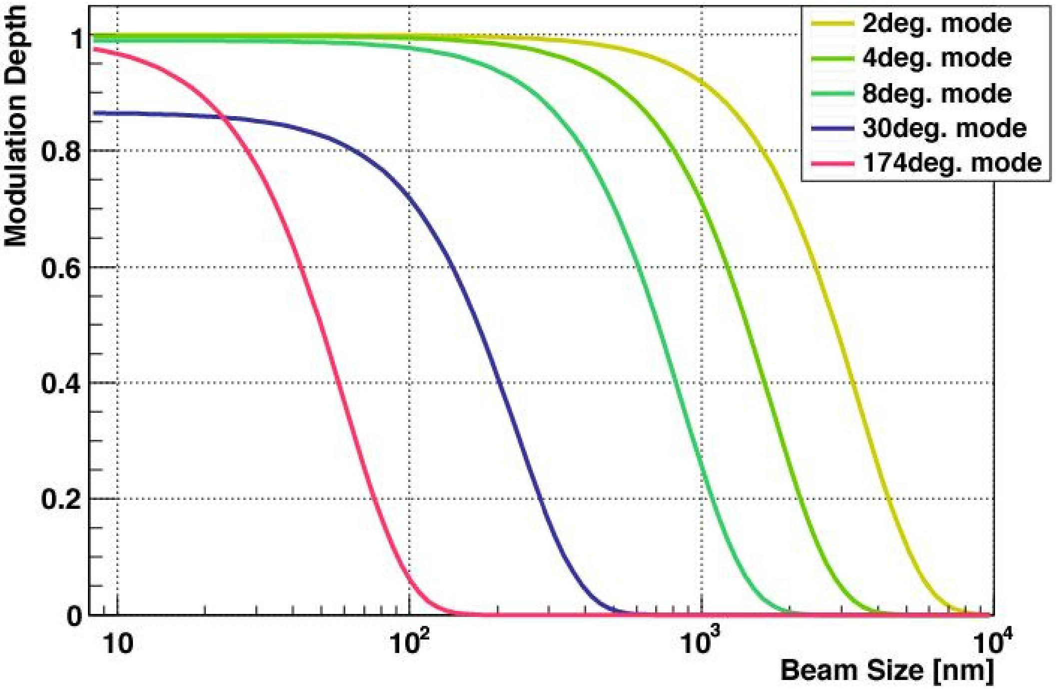

Figure 11: Modulation depth of the Compton signal as a function of σ_y^* for 5 different operation modes ($\theta_{\rm ls}$=2, 4, 8, 30, 174 degrees) of the ATF2 Shintake monitor (Figure taken from [39]).

a resolution of 4 % (see Ref. [39]).

Crossing angle ($\theta_{\rm ls}$)	[degree]	**174**	**30**	**8**	**2**
Fringe pitch ($d_{\rm pp}$)	[μm]	0.266	1.028	3.81	15.2
Upper limit ($\sigma^*_{\rm larger}$)	[nm]	100	360	1400	6000
Lower limit ($\sigma^*_{\rm smaller}$)	[nm]	25	100	360	1400

Table 4: Beam size measurement window for each operation mode of the Shintake monitor (assumed resolution 4%).

The algorithm is cross-checked by comparing the vertical beam size computed by the Shintake algorithm with the beam sizes obtained according to the core and RMS beam size definitions, given in Section 2.1.2. In addition the parameter $n_{\rm bins}$ is optimised regarding this comparison. Figure 12 shows the optimisation of $n_{\rm bins}$ considering the ATF2 Nominal lattice as an example. The red curve exhibits a flat region in the range in which the value of $n_{\rm bins}$ goes from 200 to 1400. The variation of the computed value of $\sigma^*_{\rm Shi}$ within this range indicates the error of the algorithm, which is less than 0.2%. The fact that the value of $\sigma^*_{\rm Shi}$ in this regime is in between the beam sizes according to the Core and RMS definitions, as it is expected from Eq. (13), validates the design algorithm. A value of $n_{\rm bins}$= 400 is assumed in the following calculations of $\sigma^*_{\rm Shi}$.

Neither beam jitters nor instability of the interference pattern are simulated by the algorithm. Yet a statistical study with 100 different distributions of 10000 particles is performed in order to determine the error of the value obtained by the Shintake algorithm due to the finite number of particles used in

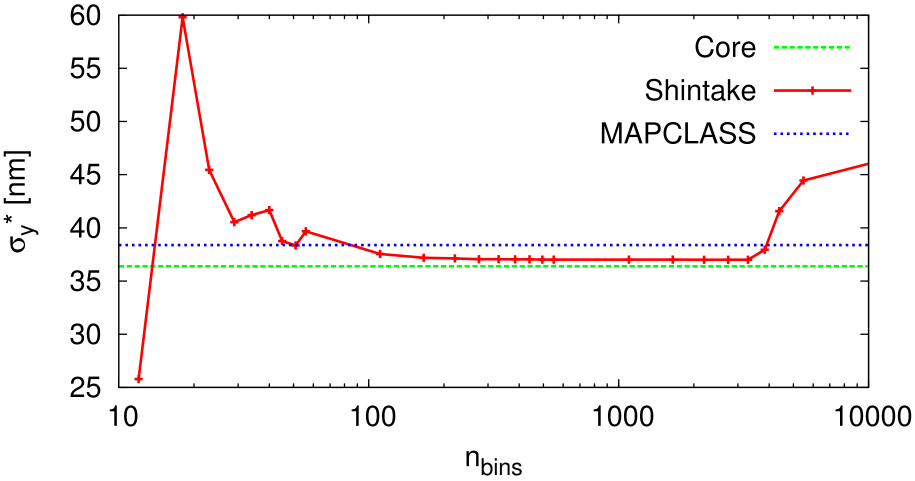

Figure 12: Simulated vertical spot size at the IP (red curve) for the ATF2 Nominal lattice as a function of the number of bins used in the simulation of the Shintake monitor. Also the expected values of σ^*_{core} and σ^*_{rms} according to the core and RMS beam size definitions are shown.

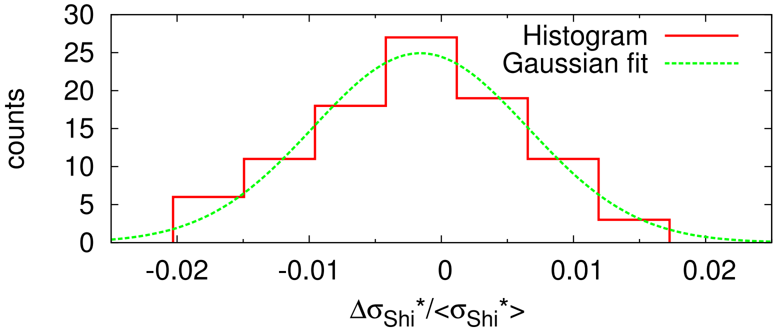

Figure 13: Histogram of 100 machines with different particle distribution at the IP. The horizontal axis is the relative deviation of the beam size from the average value over the 100 considered machines.

the calculations. Figure 13 shows the histogram of the relative difference of the computed σ^*_{Shi} with respect to the mean value over the 100 different beams. The width of the Gaussian fit at 1 sigma represents an error less than 1%. The computation of σ^*_{Shi} is extensively used in the studies presented in Sections 4.2 and 5.2.

2.1.3 Chromaticity

A quadrupole magnet focuses the particles at different longitudinal positions according to their momentum, as it is shown in Fig. 14. This effect is referred as chromaticity introduced in Section 1.2.1.1. To quantitatively estimate this effect on the beam sizes consider a quadrupole characterised by its normalised gradient K_0, (see Appendix A.2). Particles with a relative momentum deviation $\delta_p = \frac{p-p_0}{p_0}$ will see a quadrupole of normalised gradient:

$$K = \frac{e}{p}\frac{\partial B_x}{\partial y} = \frac{e}{p_0(1+\delta_p)}\frac{\partial B_x}{\partial y} \approx K_0(1-\delta_p). \tag{20}$$

The integrated normalised gradient k of a quadrupole is defined by $k = K\ l_q$. If the length of the quadrupole l_q satisfies the condition $l_q \ll (Kl_q)^{-1}$ it is a good approximation to treat the quadrupole

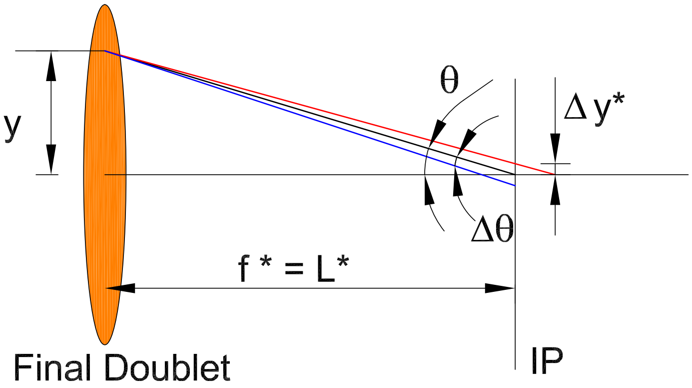

Figure 14: Scheme of the chromatic aberration induced by the final doublet which is approximate as a unique thin lens of focal length (f^*) defined by $\mathrm{f}^* = \frac{1}{K_0 l_q}$ which coincides with L^* (Figure is not to scale). The red, blue and black lines show the trajectory of particles arriving at the FD with the same y coordinate but with larger, smaller and equal momentum respectively than the reference one.

magnet as a thin lens of zero length while keeping finite its k.
The horizontal and vertical kicks $\Delta x'$, $\Delta y'$ received by an off-momentum particle into a focusing thin lens quadrupole are derived in Appendix A.3 and are given by

$$\Delta x' = -kx = -k_0(1-\delta_p)x = -k_0 x + k_0 x\delta_p, \tag{21}$$

$$\Delta y' = +ky = +k_0(1-\delta_p)y = +k_0 y - k_0 y\delta_p. \tag{22}$$

Since y is typically of the order of millimetres and L^* is of the order of meters, the IP angle $\theta \approx y/\mathrm{f}^* = y/\mathrm{L}^*$ as Fig. 14 shows. Therefore the displacement at the IP can be expressed as $\Delta y^* \approx \mathrm{L}^*\Delta\theta$. Identifying the terms proportional to δ_p in Eqs. (21) and (22) as sources of $\Delta\theta$, it can be obtained that

$$\Delta y^* \approx \mathrm{L}^* k_0 y \delta_p, \tag{23}$$

assuming $y \approx \mathrm{L}^*\theta$ and considering that $k_0 = 1/\mathrm{L}^*$, the Eq. (23) becomes

$$\Delta y^* \approx \mathrm{L}^*\theta\delta_p. \tag{24}$$

To estimate the impact of this aberration on the rms vertical beam size it is assumed that there is no correlation between the energy and the angle, the Eq. (24) becomes

$$\Delta y^*_{\mathrm{rms}} \approx \mathrm{L}^*\theta_{\mathrm{rms}}\Delta_{p\ (\mathrm{rms})}, \tag{25}$$

where θ_{rms} is the rms angle or equivalently the divergence of the beam at the IP, $\Delta_{p\ (\mathrm{rms})}$ is the energy spread. The relative vertical beam size increase at the IP is related to the design IP vertical beam size σ^*_y as

$$\frac{\Delta y^*_{\mathrm{rms}}}{\sigma^*_y} \approx \mathrm{L}^*\frac{\theta_{\mathrm{rms}}}{\sigma^*_y}\Delta_{p\ (\mathrm{rms})}. \tag{26}$$

Replacing θ_{rms} by the divergence $\sqrt{\epsilon/\beta^*}$ and since $\eta^*_{x,y} = 0$ and σ^*_y is given by $\sqrt{\epsilon_y\beta^*_y}$ therefore Eq. (26)

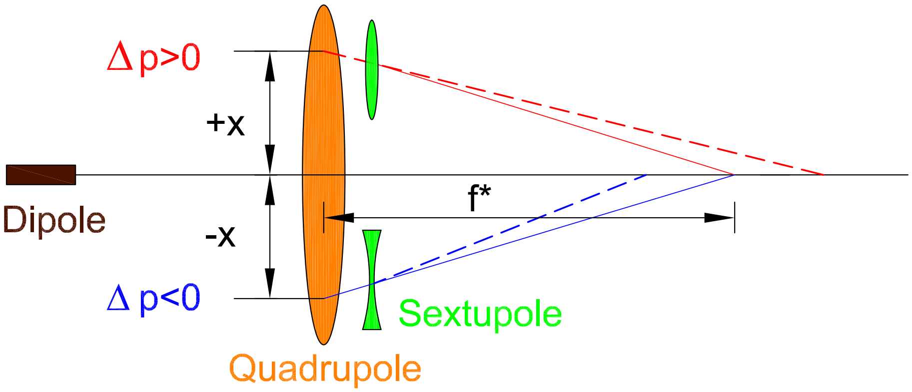

Figure 15: Scheme of the chromaticity correction by sextupoles located at a region of non zero dispersion. The dispersion generated by an upstream bending (brown colour) sorts the particles according to their energy, the sextupole (green colour) provides an extra focusing to particles with higher energy and vice-versa. Dash lines represent particle trajectories without chromaticity correction while continuous lines represent particle trajectories taking into account the effect of the sextupole field.

can be expressed as

$$\frac{\Delta y^*_{\mathrm{rms}}}{\sigma^*_y} \approx \frac{\mathrm{L}^*}{\beta^*_y}\Delta_{p\ (\mathrm{rms})} \approx \xi_y \Delta_{p\ (\mathrm{rms})}, \tag{27}$$

where $\mathrm{L}^*/\beta^*_{x,y}$ is the leading term of the natural chromaticity $\xi_{x,y}$ introduced by the FD, which in a FFS it is the most important source of chromaticity.
A more general definition of the natural chromaticity is given by

$$\left(\frac{\sigma^*}{\sigma^*_0}\right)^2 = 1 + \xi^2 \Delta^2_{p\ (\mathrm{rms})} + O(\geq\ \Delta^4_{p\ (\mathrm{rms})}), \tag{28}$$

where the natural chromaticity is identified as the coefficient of the quadratic term in the approximation.
Equation (27) can be used to estimate the effect of the chromaticity on the IP vertical beam size for the CLIC BDS with $\mathrm{L}^* = 6$ m. The CLIC energy spread is expected to be 1%, full width of a uniform distribution $\Delta_{p\ (\mathrm{uniform})}$. This amounts to $\Delta_{p\ (\mathrm{rms})} = \frac{\Delta_{p\ (\mathrm{uniform})}}{\sqrt{12}} \approx 0.3\%$, and the vertical β-function at the IP is 0.12 mm, the relative vertical IP beam size amounts to 150. In the CLIC BDS baseline design, the β^*_y is equal to 0.07 mm which increases $\Delta y^*_{\mathrm{rms}}/\sigma^*_y$ by a factor of 145. In order to avoid this detrimental effect due to the energy spread, the chromaticity needs to be corrected.

2.1.3.1 Chromaticity correction

To correct the chromaticity it is required to separate spatially particles with different energies. To this end a bending magnet is inserted prior to the FD in order to generate a dispersion function $\eta_x(s)$. Once the particles are separated by energy, different focusing corrections are applied depending on the energy of the particles by using sextupoles, whose field is non-linear in the transverse directions as shown in Appendix A.2. Figure 15 explains schematically how the correction takes place.

The normalised sextupole gradient (K_s) is given by

$$K_s = \frac{e}{p}\frac{\partial^2 B_y}{\partial x^2}, \tag{29}$$

see Appendix A.2. The kick that a focusing thin sextupole magnet provides to a particle can be written as:

$$\begin{aligned} \Delta x'_{\text{sext}} &= -\frac{1}{2}k_s(x^2 - y^2), && (30)\\ \Delta y'_{\text{sext}} &= k_s(x \cdot y), && (31) \end{aligned}$$

where $k_s = K_s \cdot l_s$ is the integrated normalised gradient of a sextupole in the thin lens approximation and l_s is the length of the sextupole magnet. Considering the horizontal dispersion created by the upstream dipole, the x coordinate can be decomposed in two contributions $x = x_\beta + \eta_x\delta_p$ while the y coordinate is expressed by $y = y_\beta$ assuming that $\eta_y = 0$ since there are no vertical dipoles in the FFS. Equations (30) and (31) can be rewritten as:

$$\begin{aligned} \Delta x'_{\text{sext}} &= -k_s[x_\beta\eta_x\delta_p + \frac{1}{2}\eta_x^2\delta_p^2 + \frac{1}{2}(x_\beta^2 - y_\beta^2)] && (32)\\ \Delta y'_{\text{sext}} &= k_s[y_\beta x_\beta + y_\beta\eta_x\delta_p], && (33) \end{aligned}$$

The horizontal and vertical kick received from a focusing quadrupole in a dispersion region is obtained by rewriting Eqs. (21) and (22) taking into account the horizontal dispersion as:

$$\begin{aligned} \Delta x'_{\text{quad}} &= -k_0[x_\beta + \eta_x\delta_p - x_\beta\delta_p - \eta_x\delta_p^2] && (34)\\ \Delta y'_{\text{quad}} &= k_0(1 - \delta_p)y_\beta = k_0(y_\beta - y_\beta\delta_p). && (35) \end{aligned}$$

The first two terms of Eq. (34) provide the focusing for the particle at a distance $x = x_\beta + \eta_x\delta$ from the centre of the quadrupole magnet. In the vertical plane, the first term of Eq. (35) provides the focusing. The terms proportional to $x_\beta\delta_p$ and $y_\beta\delta_p$ of Eqs. (34) and (35) vanish with the terms proportional to δ_p of Eqs. (32) and (33) respectively if the condition $k_s\eta_x = k_0$ is satisfied [‡]. However the sextupole magnet introduce a chromatic aberration of second order given by the term proportional to δ_p^2 of which just a half is compensated by the quadrupole magnet. In order to fully compensate this term, the sextupole magnets run twice stronger, which leads to an over compensation of the natural chromaticity of the lattice. For this reason the entire chromaticity of the FFS is generated once more upstream of the FD in a non-dispersive region.

The geometrical aberration (δ_p-independent) introduced by the sextupole magnets, namely the horizontal and vertical deflections proportional to $x^2 - y^2$ and xy of Eqs. (32) and (33) respectively increase the IP beam size. As an example the geometric aberration xy increase the relative vertical beam size approximate as (see Ref. [8]):

$$\frac{\Delta\sigma_y^*}{\sigma_y^*} = \frac{\sqrt{\epsilon_x\beta_x^{\text{FD}}}\text{L}^*}{\beta_x^*\eta_x^{\text{FD}}}. \tag{36}$$

Inserting the values of the CLIC L*=6 m lattice in Eq. (36) the result $\Delta\sigma_y^*/\sigma_y^* \approx 50$ is obtained. Hence while correcting the chromatic aberration, the sextupoles introduce a geometric aberration

---

[‡] Assuming that the variation of the β-functions between the FD quadrupoles and the nearby sextupoles is negligible

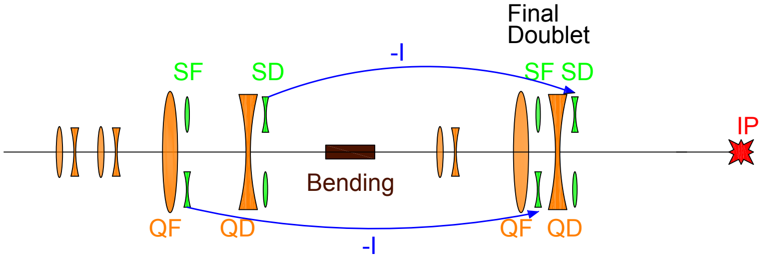

Figure 16: Optical layout of the FFS based on the local chromaticity correction. QF and QD stand for a focusing and a defocusing quadrupole magnets respectively. SF and SD stand for a focusing and a defocusing sextupole magnet. The unlabelled elements refer to quadrupole magnets meant to transport the beam.

which increases the beam size by a factor 50. The FFS with local chromaticity correction requires an additional pair of upstream sextupoles at the same phase as the ones in the FD, with a -I transformation between the pairs of sextupoles is needed in order to fully compensate these undesired contributions. The complete layout of the local chromaticity correction scheme is shown in Fig. 16. This local correction scheme is the adopted solution for the next generation of linear colliders as ILC and CLIC described in Section 2.1.3. Its experimental verification is presently ongoing at the Accelerator Test Facility (ATF2) introduced in Section 3.2.1. In terms of performance, the local chromaticity correction scheme provides a wider bandwidth of δ_p and similar alignment tolerances compared to the non-local scheme. In addition it is shorter and therefore a cheaper solution.

2.1.4 Synchrotron radiation emission

The power emitted by the Synchrotron radiation (SR) when a particle travels through a bend trajectory is proportional to the 4^{th} power of the particle energy and inversely proportional to the square of its trajectory radius, as Eq. (2) shows. The emission of photons into SR occurs statistically, leading to a quantum fluctuation of beam parameters as discussed in Ref. [40]. SR plays an important role in the performance of a high energy linear collider, specially in the FFS. As discussed in Section 2.1.3 the dispersion at the chromatic-correction sextupoles is generated by introducing the bending magnets, therefore the presence of bending magnets at the highest energy of the linear collider is an undesirable situation in terms of SR. If the energy loss occurs at a dispersive location, it causes a change in the particle orbit, which leads to a statistical increase of the emittance as explained in Ref. [36]. In order to detect a beam emittance growth, an emittance measurement station for CLIC is reported in [41]. As an example, Table 5 shows the IP beam size increase and luminosity loss due to the SR emitted in the CLIC BDS with $L^*= 3.5$ m and $L^*= 6$ m designs according to the different magnets of the FFS. An error-free lattice is assumed in these calculations. The FFS bending magnets are the most important source of both total and peak luminosity losses. As an example, the total luminosity losses are 27% and 45% for the CLIC BDS designs with $L^*= 3.5$ m and $L^*= 6$ m, respectively. The FD is the second source of luminosity loss, but the observed peak luminosity loss is lower for the CLIC BDS $L^*= 6$ m than for the CLIC BDS $L^*= 3.5$ m. The total luminosity loss taking into account the contributions from all the magnets is more than 30% and almost 50% for the baseline and alternative designs, respectively. It is worth mentioning that in both of the designs the total and the peak luminosities are above the required threshold of 10^{34} cm^{-2}s^{-1} when the effect of synchrotron radiation is taking into account.

The larger focusing provided by the FD induces a larger synchrotron radiation emission [44], specially

	σ_x^*		σ_y^*		$\Delta\mathcal{L}/\mathcal{L}$		$\Delta\mathcal{L}_{1\%}/\mathcal{L}_{1\%}$	
	[nm]		[nm]		[%]		[%]	
	L*=3.5	L*=6	L*=3.5	L*=6	L*=3.5	L*=6	L*=3.5	L*=6
SR OFF	41.1	57.0	1.0	1.1	0	0	0	0
SR ONLY MULTS	41.1	57.1	1.0	1.1	0	-1	0	0
SR ONLY FD	42.8	57.2	1.6	1.8	-10	-7	-9	-6
SR ONLY QUADS	42.9	57.2	1.6	1.8	-10	-9	-9	-6
SR ONLY BENDS	48.1	82.5	1.9	2.3	-27	-45	-13	-25
SR ON	49.8	84.1	2.0	2.4	-31	-49	-20	-30

Table 5: The effect of synchrotron radiation on σ^* and $\mathcal{L}$ is evaluated depending on the considered magnets. In this sense the magnets are grouped as: bending (BENDS), quadrupole (QUADS) except the FD, final doublet (FD) and higher order multipole (MULTS). The multipole magnets include the sextupole, octupole and decapole magnets. The study is done for the CLIC BDS L*= 3.5 m and the alternative CLIC BDS L*= 6 m designs. IP beam sizes are calculated as the standard deviation of 10^6 tracked particles by PLACET [42], and the luminosity is evaluated by GUINEA-PIG [43].

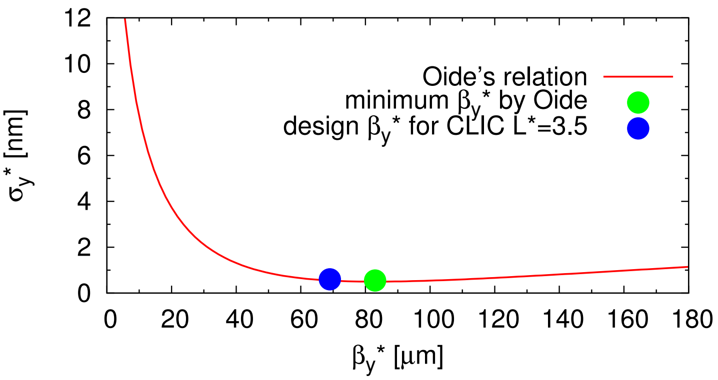

Figure 17: The vertical beam size as a function of the β-function at the collision point. The red line is obtained from Eq. (37) considering the CLIC BDS baseline design parameters, and the green and blue markers represent the minimum $\beta^*_{y,\mathrm{Oide}}$ by the Oide relation and design β^*_y values.

by the last defocusing quadrupole QD0, which leads to a luminosity degradation as shown in Table 5. The emitted synchrotron radiation by QD0 drives the focusing of the electron beams at the IP, hence the minimum σ^*_y. This is known as the Oide effect [45]. Neglecting chromatic aberrations the IP vertical beam size at the IP is given by (see Ref [45]):

$$\sigma_y^* = \sqrt{\epsilon_y\beta_y^* + A(\gamma, k_{\mathrm{QD0}}, l_{\mathrm{QD0}}, \mathrm{L}^*)\Big(\frac{\epsilon_y}{\beta_y^*}\Big)^{5/2}}, \tag{37}$$

where the function $\mathrm{A}(\gamma, k_{\mathrm{FD}}, l_{\mathrm{FD}}, \mathrm{L}^*)$ depends on the considered QD0 and its distance to the IP. Figure 17 shows the Oide beam size regarding the CLIC BDS baseline design, the minimum $\beta^*_{y,\mathrm{Oide}}$ given by the Oide relation and the design value of β^*_y of the CLIC design. This effect becomes more important in the baseline design due to the stronger FD required to reduce the β^*_y.

The impact of the SR between the two CLIC FFS designs differs on the contribution from the bending magnets due to the higher η_x-functions along the FFS for the CLIC BDS with L*=6 m. Figures 9 and 18, shows the η_x-function along the FFS of CLIC for both designs.

During collisions the bunches are strongly deflected towards each other due to their opposite charges, resulting into a reduction of the effective beam sizes and an increase of the luminosity. This effect is known as the so-called *pinch* effect. The $\mathcal{H}_D$ factor in Eq. (6) takes into account this effect. More

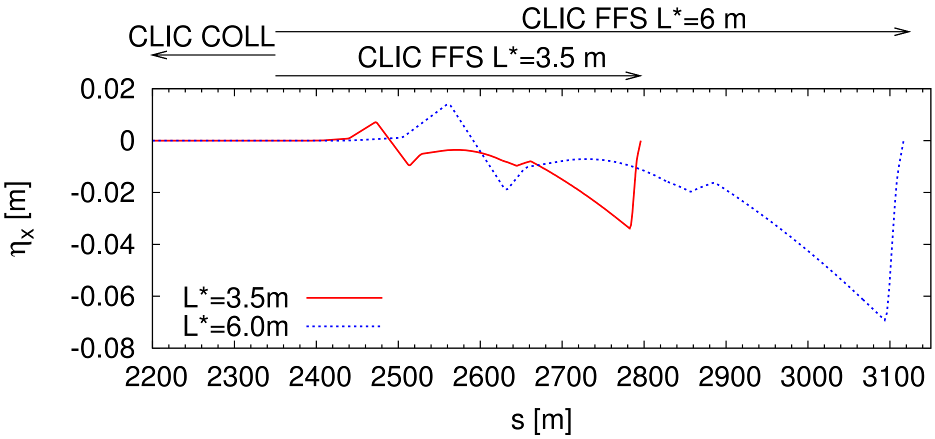

Figure 18: Comparison between the η_x-functions along the FFS of CLIC which starts after the CLIC collimation section (CLIC COLL) at position s=2356 m. The read and blue curves show the horizontal dispersion for the CLIC BDS with L*= 3.5 m and L*= 6 m designs.

discussion of the collision process is given in Ref [46]. Due to the high fields experienced by the opposite beam, as a result of the extremely high charge densities of the beams at the IP, the particles describe a bent trajectory which leads to a radiation emission referred to as beamstrahlung. The energy loss by emission can be a significant fraction of the total beam energy, enlarging the luminosity spectrum [47]. The rms relative energy loss at the collision due to the beamstrahlung $\delta_{p\,(\mathrm{B})}$ is given by the following relation (taken from [48]):

$$\delta_{p\,(\mathrm{B})} \approx 0.86 \frac{e\, r_e^3}{2m_0c^2} \Big(\frac{E_{\mathrm{cm}}}{\sigma_z}\Big) \frac{N_b^2}{(\sigma_x^* + \sigma_y^*)^2}, \tag{38}$$

where $r_e = \frac{e^2}{4\pi\epsilon_0 m_0 c^2}$ is the classical electron radius. If $\delta_{p\,(\mathrm{B})}$ increases considerably this would lead to an energy reduction which would cause a luminosity loss in the 1% energy peak, see Ref. [49]. According to Eq. (6) the product $(\sigma_x\, \sigma_y)$ must be small in order to enhance the luminosity. However according to Eq. (38) the sum $(\sigma_x + \sigma_y)$ must be maximised to reduce the relative energy loss. Taking advantage of the natural flat beams coming out from the damping rings the next generation of linear colliders are designed to collide flat beams with $\sigma_y \ll \sigma_x$ as a trade off of the pinch effect and the maximisation of the luminosity. For example, in the case of CLIC baseline design the aspect ration is $\frac{\sigma_x^*}{\sigma_y^*} \approx 40$.

2.2 MAPS formalism

Excluding the sextupoles and even higher order multipole magnets the beam transport along the machine is described by a product of the transport matrices R. The free field region or drift space, bending and quadrupole magnets are represented by the matrices R_d, R_b and R_q respectively. In Appendix A.3 the matrix representation of these elements is given. The global transport of a particle through several magnets and drift spaces is $u_{\mathrm{f}} = R\, u_0$ where R is the matrix product of the individual matrices and u_0 and u_{f} are the initial and final state vectors. The R matrix maps the initial coordinates of the beam $u_0 = (x_0,\, x_0',\, y_0,\, y_0',\, \delta_p)$ to the coordinates at the final position u_f as:

$$u_\mathrm{f} = R\, u_0 = \begin{pmatrix} R_{11} & R_{12} & R_{13} & R_{14} & R_{15} \\ R_{21} & R_{22} & R_{23} & R_{24} & R_{25} \\ R_{31} & R_{32} & R_{33} & R_{34} & R_{35} \\ R_{41} & R_{42} & R_{43} & R_{44} & R_{45} \\ R_{51} & R_{52} & R_{53} & R_{54} & R_{55} \end{pmatrix} \begin{pmatrix} x \\ x' \\ y \\ y' \\ \delta_p \end{pmatrix}_0 . \tag{39}$$

This matrix formalism is effectively used to describe the linear system. The two dimensional transfer matrix from two longitudinal locations s_0 to s_f in a transport beam line can be written as [50]:

$$\begin{pmatrix} \sqrt{\frac{\beta_{\mathrm{f},i}}{\beta_{0,i}}}(\cos\Delta\varphi_i + \alpha_{0,i}\sin\Delta\varphi_i) & \sqrt{\beta_{0,i}\beta_{\mathrm{f},i}}\,\sin\Delta\varphi_i \\ -\frac{1+\alpha_{0,i}\alpha_{\mathrm{f},i}}{\sqrt{\beta_{0,i}\beta_{\mathrm{f},i}}}\sin\Delta\varphi_i + \frac{\alpha_{0,i}-\alpha_{\mathrm{f},i}}{\sqrt{\beta_{0,i}\beta_{\mathrm{f},i}}}\cos\Delta\varphi_i & \sqrt{\frac{\beta_{0,i}}{\beta_{\mathrm{f},i}}}(\cos\Delta\varphi_i - \alpha_{\mathrm{f},i}\sin\Delta\varphi_i) \end{pmatrix}, \tag{40}$$

where i stands for the horizontal or vertical planes, $\beta(s)$ and $\alpha(s)$ are the Twiss functions and $\Delta\varphi_i = \varphi_i(s_\mathrm{f}) - \varphi_i(s_0)$ is the phase advance between the final and initial locations, s_f and s_0 respectively. The R_{12} and R_{34} coefficients are of special interest since they relate the initial angular kicks at the start x_0' and y_0' with the change in final coordinates x_f and y_f, respectively.

However this matrix formalism cannot be applied to describe the higher order elements of the system such as the sextupole magnets. In order to include the non-linear elements a new framework is required. The map is extended by additional transfer matrices (T, U) [51] as suggested in [52]. The coordinates at the final position $u_{\mathrm{f},i}$ are related to the initial ones $u_{0,i}$ by:

$$u_{\mathrm{f},i} = \sum_{j=1}^{5} R_{i,j}\;\, u_{0,j} + \sum_{j,k=1}^{5} T_{i,jk}\;\, u_{0,j}u_{0,k} + \sum_{j,k.l=1}^{5} U_{i,jkl}\;\, u_{0,j}u_{0,k}u_{0,l} + O(\geq 4). \tag{41}$$

This map can also be expressed in a more compact way as

$$u_{\mathrm{f},i} = \sum_{jklmn} X_{i,jklmn}\;\, x_0^j\, p_{x_0}^k\, y_0^l\, p_{y_0}^m\, \delta_p^n, \tag{42}$$

where the coordinates x' and y' are replaced by p_x and p_y respectively, being $u_1 = x$, $u_2 = p_x$, $u_3 = y$, $u_4 = p_y$ and $u_5 = \delta_p$. The Polymorphic Tracking Code (PTC) [53], [54] provides the $X_{i,jklmn}$ coefficients for a given beam line defined in the MAD-X [55] environment. The PTC models the accelerator elements by the evaluation of their Hamiltonian [56]. The accuracy of the model is determined by the user who defines the maximum order, N_order, used for the evaluation of the Hamiltonians. The sum of the indices j, k, l, m and n in Eq. (42) is equal to N_order. For instance for N_order=2 the map coefficients $X_{i,jklmn}$ are evaluated including up to the sextupole components and neglecting the higher multipole components of the beam line.

The MAPCLASS code profits from the calculation of the $X_{i,jklmn}$ coefficients by the PTC module of MAD-X to transport a distribution of particles ρ.

The distribution of particles is characterised by its moments $\langle u_i^n \rangle$ which are calculated by:

$$\langle u_i^n \rangle = \int_{-\infty}^{\infty} u_i^n\, \rho\, d\nu. \tag{43}$$

The first moment defined by Eq. (43) can be rewritten as:

$$\langle u_{\mathrm{f},i}\rangle = \int_{-\infty}^{\infty} u_{\mathrm{f},i}\,\rho_{\mathrm{f}}\,d\nu_{\mathrm{f}} = \int_{-\infty}^{\infty} \sum_{jklmn}^{N_{\mathrm{order}}} X_{i,jklmn}\, x_0^j\, p_{x_0}^k\, y_0^l\, p_{y_0}^m\, \delta_{p,0}^n\, \rho_0 d\nu_0 =$$

$$= \sum_{jklmn}^{N_{\mathrm{order}}} X_{i,jklmn} \int_{-\infty}^{\infty} x_0^j\, p_{x_0}^k\, y_0^l\, p_{y_0}^m\, \delta_{p,0}^n\, \rho_0 d\nu_0 \quad (44)$$

where it has been assumed that the beam line transport is symplectic, this implies $\rho_{\mathrm{f}} d\nu_{\mathrm{f}} = \rho_0 d\nu_0$ along the BDS. The rms beam size is obtained from the quadratic standard deviation of the final density distribution given by:

$$\begin{aligned}\sigma_{\mathrm{f},i}^2 &= \langle u_{\mathrm{f},i}^2\rangle - \langle u_{\mathrm{f},i}\rangle^2 = \sum_{\substack{jklmn\\ j'k'l'm'n'}}^{N_{\mathrm{order}}} X_{i,jklmn}X_{i,j'k'l'm'n'} \int_{-\infty}^{\infty} x_0^{j+j'} p_{x_0}^{k+k'} y_0^{l+l'} p_{y_0}^{m+m'} \delta_p^{n+n'}\ \rho_0 d\nu_0 \\ &\quad - \left(\sum_{jklmn}^{N_{\mathrm{order}}} X_{i,jklmn} \int_{-\infty}^{\infty} x_0^j\, p_{x_0}^k\, y_0^l\, p_{y_0}^m \delta_p^n\ \rho_0\, d\nu_0\right)^2. \qquad (45)\end{aligned}$$

The result in Eq. (45) is equivalent to the σ_{rms} definition given in Section 2.1.2. An example of beam size calculation for CLIC is discussed in detail in Ref. [19].
According to Eq. (28) and considering only the purely chromatic contributions to ξ_y the natural chromaticity can be re-written as

$$\xi_y^2 = \frac{1}{12\,(\sigma_y^*)^2}\left(X_{y,00101}X_{y,00101}\ \sigma_{y0}^2 + X_{y,00011}X_{y,00011}\ \sigma_{p_y0}^2\right) =$$

$$= \frac{1}{12}\left(X_{y,00101}X_{y,00101}\ \frac{\beta_{y0}}{\beta_y^*} + X_{y,00011}X_{y,00011}\ \frac{1}{\beta_y^*\beta_{y0}}\right), \quad (46)$$

a centred Gaussian beam in the coordinates x, p_x, y, p_y and a rectangular distribution in δ_p is assumed. Eq (46) is used to evaluate the value of ξ_y for the CLIC FFS lattices. In the case of the ATF2 lattices, a centred Gaussian beam in the coordinates x, p_x, y, p_y, δ_p is assumed. Again considering only the purely chromatic contributions to ξ_y, the natural chromaticity is expressed as

$$\xi_y^2 = \frac{1}{(\sigma_y^*)^2}\left(X_{y,00101}X_{y,00101}\ \sigma_{y0}^2 + X_{y,00011}X_{y,00011}\ \sigma_{p_y0}^2\right) =$$

$$= X_{y,00101}X_{y,00101}\ \frac{\beta_{y0}}{\beta_y^*} + X_{y,00011}X_{y,00011}\ \frac{1}{\beta_y^*\beta_{y0}}, \quad (47)$$

where β_{y0} and β_y^* are the values of vertical β-function at the beginning and at the IP of the beam line respectively.

2.3 Beam based alignment

For the CLIC FFS it is required to achieve a pre-alignment of its components down to 10 μm over 500 m sliding window, see Ref. [57]. Such a resolution can be reached by means of an active pre-

alignment, as discussed in [57]. In this context the beam based alignment (BBA) method refers to the approach that uses measurements of beam parameters to infer the offset between the beam and the machine element. The problem of determining the alignment limiting factors that preclude to improve the BBA resolution is in the scope of this thesis.
The residual misalignment of quadrupole and sextupole magnets has a non negligible impact on the beam size as it is shown in the following. Section 6 presents the simulations and experimental results.

2.3.1 Off-axis magnetic fields

The magnetic fields (B_x, B_y) of a perfectly aligned quadrupole and sextupole magnets described in Appendix A.2 are given by:

$$\text{Quadrupole} \left\{ \begin{array}{ll} B_x & = B'y \quad \text{where} \quad B' = \frac{\partial B_x}{\partial y} = \frac{\partial B_y}{\partial x} \\ B_y & = B'x \end{array} \right. , \tag{48}$$

$$\text{Sextupole} \left\{ \begin{array}{ll} B_x & = B''xy \quad \text{where} \quad B'' = \frac{\partial^2 B_x}{\partial y \partial x} = \frac{\partial^2 B_y}{\partial x^2} \\ B_y & = \frac{1}{2}B''(x^2 - y^2) \end{array} \right. , \tag{49}$$

B' and B'' represent the quadrupole and sextupole magnetic field gradients respectively. The magnetic field of an offset quadrupole or sextupole ($\hat{B}_x$, $\hat{B}_y$) is obtained by replacing x or y in Eqs. (48) and (49) by $x + \Delta x$ and $y + \Delta y$, where Δx and Δy are the horizontal and vertical offsets, respectively. One obtains the following magnetic fields:

$$\text{Offset Quadrupole} \left\{ \begin{array}{l} \hat{B}_x = B_x + B'\Delta y \\ \hat{B}_y = B_y + B'\Delta x \end{array} \right. \tag{50}$$

$$\text{Offset Sextupole} \left\{ \begin{array}{l} \hat{B}_x = B_x + (B''\Delta x)y + (B''\Delta y)x + B''\Delta x \Delta y \\ \hat{B}_y = B_y + (B''\Delta x)x - (B''\Delta y)y + \frac{1}{2}B''(\Delta x^2 - \Delta y^2). \end{array} \right. \tag{51}$$

Equation (50) describes the magnetic field of an offset quadrupole which differs from the magnetic field of a centred quadrupole by a constant term. This constant term is equivalent to a horizontal and vertical dipole field. The terms linear in Δx and Δy on the right hand side of Eq. (51), are equivalent to a normal and a skew quadrupole fields respectively. The $B''\Delta x \Delta y$ and $B''(\Delta x^2 - \Delta y^2)$ terms on the right hand side of Eq. (51) represent dipole fields. Thus an offset quadrupole introduces a dipole field and an offset sextupole introduces quadrupole and dipole fields. This is the so called feed-down effect due to the misaligned magnet. The additional quadrupole field introduced by the offset sextupole magnet generates a horizontal and vertical dispersion at the IP according to (see Ref. [58]):

$$\Delta \eta_x^* = K_s l_s \Delta x \; \eta_x^s \sqrt{\beta_x^s \beta_x^*} \sin(\Delta \varphi_x^s) \tag{52}$$

$$\Delta \eta_y^* = -K_s l_s \Delta y \; \eta_x^s \sqrt{\beta_y^s \beta_y^*} \sin(\Delta \varphi_y^s), \tag{53}$$

where K_s is the normalised gradient defined in Appendix A.2, l_s is the length of the sextupole, $\beta_{x,y}^s$ and $\beta_{x,y}^*$ are the horizontal and vertical β-functions at the sextupole and the IP, respectively, η_x^s is the dispersion function at the sextupole and $\Delta\varphi_{x,y}^s$ are the horizontal and vertical phase advanced between the sextupole and the IP. The additional normal quadrupole field introduced by the offset sextupole generates a shift of the waist position (see Ref. [58]) given by:

$$\Delta s_{w\ (x,y)} = \ K_s l_s \Delta x \beta^{s}_{x,y} \beta^{*}_{x,y} \cos(2\Delta\varphi_{x,y}), \tag{54}$$

leading to an increase of the β-functions at the IP according to Eq. (15). In accordance with Eq. (11) the increase of both the β-functions and the dispersion leads to an IP beam size increase that degrades the luminosity in the case of a collider.

The skew quadrupole fields created by a vertical offset sextupole generate a horizontal and vertical deflection given by:

$$\Delta x' = K_s l_s y \Delta y \tag{55}$$

$$\Delta y' = K_s l_s x \Delta y, \tag{56}$$

hence the change in the vertical position at the IP is obtained by transporting $\Delta x'$ and $\Delta y'$ from the sextupole magnet to the IP by means of the R_{32} and R_{34} matrix coefficients according to Eq. (39):

$$\Delta y^* = \Delta x' R_{32,s\rightarrow\mathrm{IP}} \tag{57}$$

$$\Delta y^* = \Delta y' R_{34,s\rightarrow\mathrm{IP}} = K_s l_s x \Delta y R_{34,s\rightarrow\mathrm{IP}}, \tag{58}$$

a FFS satisfies the condition $R_{32,s\rightarrow\mathrm{IP}}$=0 by design, the change in the vertical beam size at the IP due to skew quadrupole field is obtained by integrating Eq. (58) over the x coordinate, it is given by the following equations:

$$\Delta\sigma^*_y = K_s l_s \sigma_x \Delta y |R_{34,s\rightarrow\mathrm{IP}}|. \tag{59}$$

The coupling between the horizontal and vertical plane can also be introduced by tilted quadrupole magnets. The $\Delta\sigma^*_y$ due to coupling between the x with the y coordinate given by Eq. (59), can be compensated by vertically moving the sextupoles as suggested in [59].

In order to quantify the effect of a random misalignment of all the magnets in the CLIC BDS with L*= 6 m, 100 different machines with random misalignments of their magnets with respect to the ideal positions are seeded. Different width of Gaussian distributions σ_{offset} have been used for misaligning the magnets. Figure 19 shows the average IP vertical beam size $<\sigma^*_y>$ (red) and the average luminosity (green) for different values of σ_{offset}. For $\sigma_{\mathrm{offset}} = 1$ μm the average vertical spot size at the IP is more than 4 orders of magnitude larger than the value by design. The obtained luminosity is almost 3 orders of magnitude smaller than the designed one. In these calculations 10^6 particles are tracked by PLACET [42] throughout the entire CLIC BDS with L*= 6 m, the beam size is obtained as the rms of the final particle positions and the luminosity is calculated by the code GUINEA-PIG [43], frequently used for simulation of the beam-beam interaction in an electron-positron linear colliders [60]. In conclusion, the initial pre-alignment of the magnets is a critical parameter for CLIC. The goal of this study is to improve the alignment resolution obtained by BBA techniques and to determine its limiting factors.

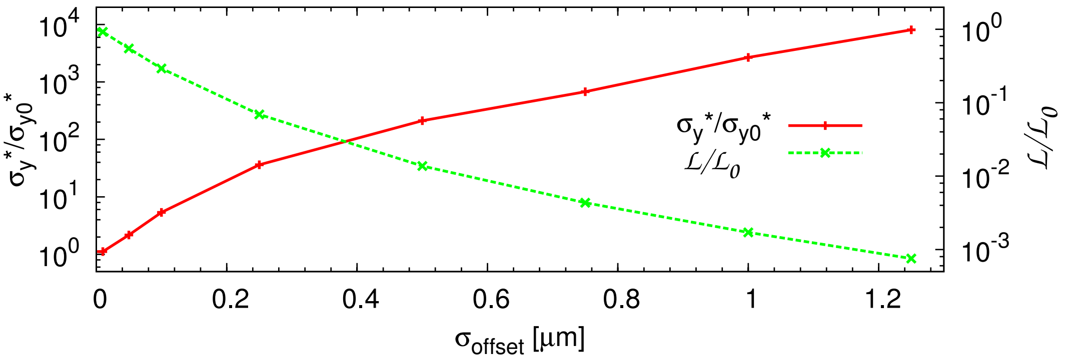

Figure 19: Average $\mathcal{L}/\mathcal{L}_0$ and σ_y^*/σ_{y0}^* for 100 different CLIC BDS L*= 6 m machines versus transverse misalignments. For each machine the magnets are randomly misaligned by following a Gaussian distribution with sigma σ_{offset}.

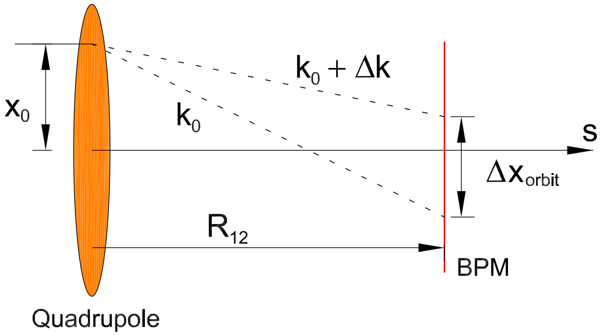

Figure 20: Principle of quadrupole shunting of BBA.

2.3.2 Theoretical model of the beam based alignment

A particle passing through a focusing quadrupole magnet with a horizontal offset x_0 from its magnetic centre experiences a kick given by:

$$\Delta x' = -k\ x_0 \quad , \tag{60}$$

where k is the normalised integrated strength of the quadrupole. If k is modified by Δk the change in the orbit reading of the i^{th} downstream BPM is given by:

$$\Delta x_{\text{orbit}}(i) = -x_0\ \Delta k\ R_{12}(i) \quad , \tag{61}$$

where $R_{12}(i)$ is the linear transport matrix element introduced in Section 2.2 that transport the x' coordinate from the quadrupole to the i^{th} downstream BPM. By varying the quadrupole current and measuring the downstream deflection, the value of x_0 can be inferred. This technique is known as quadrupole shunting [61]. Figure 20 illustrates this method schematically.

Assuming a resolution of the BPMs given by σ_{BPM}, the strength of the quadrupole magnet is scanned over j steps of current variation dk where Δk refers to the maximum current excursion $\Delta k = j_{\text{max}} dk$. The offset magnet x_0 may be fitted with a statistical resolution related to the registered number of pulses p as (derived in [61]):

$$\sigma_{x_0}^2 = \frac{\sigma_{\text{orbit}}^2}{p\sum_{j=1}^{j_{\max}}(jdk)^2\sum_i R_{12}^2(i)}. \tag{62}$$

Thus, BPMs placed at locations with higher values of R_{12} are able to resolve the offset magnet with a better resolution. Δk is usually 20% but it is determined by the maximum acceptable distortion of the orbit and size of the beam of the accelerator and the BPMs resolution. Since errors of the lattice tend to accumulate the BPMs located further away from the offset magnet may not be considered as fully reliable. The offset resolution improves when increasing the number of recorded pulses.

σ_{orbit} essentially depends on two contributions, the BPM resolution σ_{BPM} and the beam jitter σ_{jitter}. The jitter refers to the incoming position and angle variation from pulse to pulse at the upstream face of the quadrupole whose current is varied. Here it is assumed that $\sigma_{\text{orbit}}^2 = \sigma_{\text{BPM}}^2 + \sigma_{\text{jitter}}^2$. By applying techniques such as the singular value decomposition (SVD) [62] the jitter signal at the BPMs can be reconstructed in such a way that the contributions from energy or position variations from pulse to pulse to the orbit jitter are removed. It is worth noticing that the current excursion provided by Δk should be chosen so that the orbit remains in the high resolution dynamic range of the BPM.

The use of quadrupole shunting technique as a part of the BBA approach has several advantages namely, it provides a local correction of the offset of the magnet and it is relatively insensitive to small errors of the quadrupole current, BPM scale factors and transport matrices. However there are several disadvantages as well, it is a quite invasive technique, therefore it requires dedicated beam time to perform the measurements and the quadrupole centre position must be quite robust. The magnetic centre motion of the quadrupole when its strength is varied represents an alignment resolution limiting factor. Asymmetries due to mechanical construction, different thermal expansion or excitation of the poles are sources of errors which may lead to a motion of the magnetic centre while changing its current. This systematic error depends on each magnet construction and its nominal current. In what follows, a procedure for detecting and quantifying this effect is developed. Assuming that the magnetic centre moves a distance x_{mc} when the normalised integrated strength is varied by Δk, the orbit reading at the downstream i^{th} BPM is obtained by re-writing Eq. (61), as:

$$x_{\text{orbit}}(i) = -(x_0 + x_{\text{mc}})(k + \Delta k)R_{12}(i). \tag{63}$$

Thus the difference in the orbit readings at the i$^{\text{th}}$ BPM between the orbit with Δk and the one at nominal strength is given by:

$$\Delta x_{\text{orbit}}(i) = -[(x_0 + x_{\text{mc}})\Delta k + x_{\text{mc}}k]R_{12}(i). \tag{64}$$

For small variations of the quadrupole strength, the motion of the magnetic centre is likely to be linear. With this assumption x_{mc} can be replaced by $\dot{x}_{\text{mc}}\Delta k$, where $\dot{x}_{\text{mc}}$ characterises the magnetic centre variation when changing the quadrupole strength. Then Δx_{orbit} is re-written as:

$$\Delta x_{\text{orbit}}(i) = -R_{12}(i)[(x_0 + \dot{x}_{\text{mc}}k)\Delta k + \dot{x}_{\text{mc}}\Delta k^2]\ , \tag{65}$$

and Δx_{orbit} depends linearly and quadratically on Δk. The quadratic term permits to fit $\dot{x}_{\text{mc}}$ and, in addition, obtain x_0. This method was used in the BBA measurement campaign performed in May 2010 at ATF2. The results are discussed in Section 6.3.1.

An alternative method to estimate $\dot{x}_{\text{mc}}$ which does not rely on the knowledge of the linear optics of the lattice is to determine the magnetic centre position for the same quadrupole magnet for two different currents k_1 and k_2. From the eventual different magnetic centre positions $(x_{0,k_1} \neq x_{0,k_2})$, $\dot{x}_{\text{mc}}$ is determined by:

$$\dot{x}_{\text{mc}} = \frac{x_{0,k_2} - x_{0,k_1}}{k_2 - k_1}. \tag{66}$$

This method was used in the BBA measurement campaign conducted in July 2011 at CTF3. The results are presented in Section 6.3.2.

2.4 Tuning of a final focus system

The values of σ_x^* and σ_y^* discussed in Section 1.2 for both CLIC BDS baseline and alternative designs are obtained without taking into account realistic errors present in the machine components. For example, if the magnets of the CLIC BDS with $L^*= 6$ m design are randomly scattered in the transverse position according to a Gaussian distribution of width $\sigma_{\text{offset}}= 1$ μm, the obtained average σ_y^* is more than 3 orders of magnitude larger than in the ideal case, as it is shown in Fig. 19.
Tuning is the procedure which brings the system to its design performance in the presence of realistic imperfections by optimising the machine components. The tuning simulations of a FFS are used to demonstrate its feasibility within realistic error conditions. Due to the presence of sextupole and even higher order multipole magnets and a large number of variables, the CLIC FFS turns out to be a non-linear and complex system.
Since the initial error conditions are known within a certain range, the tuning requires a statistical study. Usually 100 machines are considered in computer simulations. The initial errors of each machine are randomly assigned within the expected range.
The dynamic error conditions such as the ground motion are not considered in the tuning study presented in Sections 5.1 and 5.2, since the long term performance of the system is beyond the scope of this thesis.

2.4.1 Tuning algorithms

The tuning algorithm defines the machine components or variables to be optimised in order to achieve the expected performance in terms of IP beam size or luminosity. The variables used for tuning, are usually the displacements, tilts and the strength of the magnets. Three different tuning algorithms are considered in this thesis, the *Simplex-Nelder* [63], *beam based alignment* and *orthogonal knobs*. A short description of them follows below.

2.4.1.1 Simplex-Nelder Algorithm

The *Simplex-Nelder* algorithm is a numerical method commonly used for optimisation of non-linear problems. This technique minimises an objective function in a many-dimensional space. In our study, the objective function is usually the IP beam size or the luminosity while the dimensional space is formed by the machine parameters. Due to the large number of variables to be tuned the tuning convergence to the design beam size or luminosity is not guaranteed.

2.4.1.2 Beam based alignment

The *beam based alignment* (BBA) [61] refers to the classical method used to correct the beam trajectory along the beam line. To implement BBA methods a set of BPMs and correctors are needed. Small dipole magnets are usually used as correctors, but displacement of the quadrupole magnets are valid as well. Assuming that there are N BPMs available in the beam line, the orbit measured by the monitors are represented by a vector $\vec{b}_N$, while a vector $\vec{C}_M$ represents the strength of M correctors present in the beam line.

The orbit correction and the dispersion free steering (DFS) are two examples of BBA techniques explained in the following:

2.4.1.2.1 Orbit correction

The orbit correction technique [64] minimises the BPM readings seeking for a flat orbit through the beam line. Activating each corrector one at a time and recording the orbit excitation at all BPMs, the response $(N \times M)$ matrix R_c of the correctors is determined. The orbit correction algorithm gives optimum strength of the correctors, by solving:

$$\vec{b}_{N,0} + R_c \cdot \vec{C}_M = 0, \tag{67}$$

where $\vec{b}_{N,0}$ are the initial BPM readings before correction.

2.4.1.2.2 Dispersion free steering

The dispersion free steering (DFS) algorithm [65] intends to correct the orbit and to match the measured dispersion η along the beam line to the nominal dispersion η_0. The dispersion is measured by sending two beams with energies that deviate from the nominal energy by $\pm\Delta E$ through the beam line, obtaining two different orbit readings $\vec{b}_{\Delta E_+}$ and $\vec{b}_{\Delta E_-}$. The measured dispersion is given by:

$$\vec{\eta} = \frac{\vec{b}_{\Delta E_+} - \vec{b}_{\Delta E_-}}{2\Delta E}. \tag{68}$$

The $(N \times M)$ matrix D describes the dispersion response of the system to the correctors, it is obtained by activating each corrector one at a time and recording the dispersion deviation from the design dispersion η_0 at the N BPMs.

In the DFS algorithm the optimum strength of the correctors is obtained by solving the equation:

$$\begin{pmatrix} \vec{b}_N \\ \vec{\eta} - \vec{\eta}_0 \end{pmatrix} + \begin{pmatrix} R_c \\ D \end{pmatrix} \cdot \vec{C}_M = 0. \tag{69}$$

2.4.1.3 Orthogonal Knobs

The *orthogonal knobs* are pre-computed combinations of sextupole displacements meant to control a chosen set of beam aberrations. The knobs are constructed to be orthogonal in order to preserve the correction provided by each knob when scanning the whole set of knobs. The expected beam aberrations at the IP induced by quadrupole and sextupole displacements are variations in the β-functions, waist shifts, dispersion and coupling.

The 5 sextupole magnets present in the FFS, namely SF6, SF5, SD4, SF1 and SD0, are used for construction of the orthogonal knobs. Therefore up to 10 knobs can be obtained by horizontal and vertical displacements. By moving a sextupole magnet in the horizontal plane, horizontal dispersion and shift of the waist positions are introduced as given by Eqs. (52) and (54). Therefore α_x^*, α_y^* and β_x^* depend on the horizontal position of the sextupole magnets denoted by x_{SF6}, x_{SF5}, x_{SD4},

x_{SF1}, and x_{SD0}. The knobs denoted by α_x^*, α_y^* and η_x^* are constructed from horizontal displacements of the sextupole magnets. For completeness two additional horizontal knobs denoted by β_x^* and β_y^* are included in the calculations, but a good performance of these knobs is not expected since the β-function at the IP varies quadratically versus the sextupole displacement as Eq. (15) shows.

By moving a sextupole magnet in the vertical plane, coupling and vertical dispersion are generated according to Eq. (53) and (59). The knobs constructed from the vertical displacements are denoted by: $< x, y >$, $< p_x, y >$, $< p_x, p_y >$, η_y^* and $\eta_y^{*'}$, here the brackets refer to the correlation between the coordinates in between, which is defined as:

$$< u_i, u_j >= \int_{-\infty}^{+\infty} u_i u_j \; \rho \; d\nu, \tag{70}$$

where u stands for x, p_x, y, p_y and δ. The horizontal and vertical response matrices, M_x and M_y, are constructed as:

$$M_x = \begin{pmatrix} \frac{\partial\beta_x^*}{\partial x_{\mathrm{SF6}}} & \frac{\partial\beta_x^*}{\partial x_{\mathrm{SF5}}} & \frac{\partial\beta_x^*}{\partial x_{\mathrm{SD4}}} & \frac{\partial\beta_x^*}{\partial x_{\mathrm{SF1}}} & \frac{\partial\beta_x^*}{\partial x_{\mathrm{SD0}}} \\ \frac{\partial\alpha_x^*}{\partial x_{\mathrm{SF6}}} & \frac{\partial\alpha_x^*}{\partial x_{\mathrm{SF5}}} & \frac{\partial\alpha_x^*}{\partial x_{\mathrm{SD4}}} & \frac{\partial\alpha_x^*}{\partial x_{\mathrm{SF1}}} & \frac{\partial\alpha_x^*}{\partial x_{\mathrm{SD0}}} \\ \frac{\partial\beta_y^*}{\partial x_{\mathrm{SF6}}} & \frac{\partial\beta_y^*}{\partial x_{\mathrm{SF5}}} & \frac{\partial\beta_y^*}{\partial x_{\mathrm{SD4}}} & \frac{\partial\beta_y^*}{\partial x_{\mathrm{SF1}}} & \frac{\partial\beta_y^*}{\partial x_{\mathrm{SD0}}} \\ \frac{\partial\alpha_y^*}{\partial x_{\mathrm{SF6}}} & \frac{\partial\alpha_y^*}{\partial x_{\mathrm{SF5}}} & \frac{\partial\alpha_y^*}{\partial x_{\mathrm{SD4}}} & \frac{\partial\alpha_y^*}{\partial x_{\mathrm{SF1}}} & \frac{\partial\alpha_y^*}{\partial x_{\mathrm{SD0}}} \\ \frac{\partial\eta_x^*}{\partial x_{\mathrm{SF6}}} & \frac{\partial\eta_x^*}{\partial x_{\mathrm{SD0}}} & \frac{\partial\eta_x^*}{\partial x_{\mathrm{SD4}}} & \frac{\partial\eta_x^*}{\partial x_{\mathrm{SF1}}} & \frac{\partial\eta_x^*}{\partial x_{\mathrm{SD0}}} \end{pmatrix}$$

$$M_y = \begin{pmatrix} \frac{\partial<x,y>}{\partial y_{\mathrm{SF6}}} & \frac{\partial<x,y>}{\partial y_{\mathrm{SF5}}} & \frac{\partial<x,y>}{\partial y_{\mathrm{SD4}}} & \frac{\partial<x,y>}{\partial y_{\mathrm{SF1}}} & \frac{\partial<x,y>}{\partial y_{\mathrm{SD0}}} \\ \frac{\partial<p_x,y>}{\partial y_{\mathrm{SF6}}} & \frac{\partial<p_x,y>}{\partial y_{\mathrm{SF5}}} & \frac{\partial<p_x,y>}{\partial y_{\mathrm{SD4}}} & \frac{\partial<p_x,y>}{\partial y_{\mathrm{SF1}}} & \frac{\partial<p_x,y>}{\partial y_{\mathrm{SD0}}} \\ \frac{\partial<p_x,p_y>}{\partial y_{\mathrm{SF6}}} & \frac{\partial<p_x,p_y>}{\partial y_{\mathrm{SF5}}} & \frac{\partial<p_x,p_y>}{\partial y_{\mathrm{SD4}}} & \frac{\partial<p_x,p_y>}{\partial y_{\mathrm{SF1}}} & \frac{\partial<p_x,p_y>}{\partial y_{\mathrm{SD0}}} \\ \frac{\partial\eta_y^*}{\partial y_{\mathrm{SF6}}} & \frac{\partial\eta_y^*}{\partial y_{\mathrm{SF5}}} & \frac{\partial\eta_y^*}{\partial y_{\mathrm{SD4}}} & \frac{\partial\eta_y^*}{\partial y_{\mathrm{SF1}}} & \frac{\partial\eta_y^*}{\partial y_{\mathrm{SD0}}} \\ \frac{\partial\eta_y^{*'}}{\partial y_{\mathrm{SF6}}} & \frac{\partial\eta_y^{*'}}{\partial y_{\mathrm{SF5}}} & \frac{\partial\eta_y^{*'}}{\partial y_{\mathrm{SD4}}} & \frac{\partial\eta_y^{*'}}{\partial y_{\mathrm{SF1}}} & \frac{\partial\eta_y^{*'}}{\partial y_{\mathrm{SD0}}} \end{pmatrix}.$$

Each column of $M_{x,y}$ is obtained by individually moving the corresponding sextupole by 0.1 μm, assuming an ideal lattice. The values of $\beta_{x,y}^*$, $\alpha_{x,y}^*$ and η_x^* are obtained by the Twiss module of MAD-X, whereas the values of $< x, y >$, $< p_x, y >$, $< p_x, p_y >$, η_y^* and $\eta_y^{*'}$ are calculated by MAPCLASS according to Eq. (70). By inverting M_x and M_y by means of the singular value decomposition method (SVD), the orthogonal knobs are directly obtained as the columns of M_x^{-1} and M_y^{-1}. As an example, the η_x^*-knob moves horizontally the five sextupole magnets in such a way that the following conditions are satisfied:

$$\alpha_x^*(x_{\mathrm{SF6}}, x_{\mathrm{SF5}}, x_{\mathrm{SD4}}, x_{\mathrm{SF1}}, x_{\mathrm{SD0}}) = \text{constant} \tag{71}$$

$$\alpha_y^*(x_{\mathrm{SF6}}, x_{\mathrm{SF5}}, x_{\mathrm{SD4}}, x_{\mathrm{SF1}}, x_{\mathrm{SD0}}) = \text{constant} \tag{72}$$

$$\eta_x^*(x_{\mathrm{SF6}}, x_{\mathrm{SF5}}, x_{\mathrm{SD4}}, x_{\mathrm{SF1}}, x_{\mathrm{SD0}}) \neq \text{constant} \tag{73}$$

As a result of the non-linear response of the lattice, the knobs might not be fully orthogonal. However the IP beam size aberrations can be tuned out by applying the knobs iteratively.

Parameter	Symbol	Value	Unit
Length	L	186.0	m
Energy	E	46.6	GeV
Relative energy spread	Δ_p	0.3	%
Bunch population	N_p	$1{\cdot}10^{10}$	
Normalised horizontal emittance	$\gamma\epsilon_x^*$	$30{\cdot}10^{-6}$	m
Normalised vertical emittance	$\gamma\epsilon_y^*$	$2{\cdot}10^{-6}$	m
Horizontal beta function at the FP	β_x^*	2.5	mm
Vertical beta function at the FP	β_y^*	0.1	mm
Horizontal beam size at the FP	σ_x^*	1.0	μm
Vertical beam size at the FP	σ_y^*	52	nm
Free distance before the FP	L*	0.4	m
Vertical chromaticity	ξ_y	10000	

Table 6: Main design parameters of the Final Focus Test Beam.

3 State of the art and existing test facilities

The most prominent example of design, optimisation and tuning of a FFS is the Final Focus Test Beam (FFTB) [22] at the Stanford Linear Accelerator (SLAC). The FFTB was a prototype of final focus system of a linear collider based on the non-local chromaticity correction scheme discussed in Section 1.2.1.1. A vertical spot size of about 70 nm was achieved [66] at the focal point (FP) which still remains the world record.

Feasibility demonstration of conceptual designs and technical solutions are currently being implemented at test facilities. In this chapter the Accelerator Test Facility (ATF) [67], and its extension ATF2, at KEK (Japan) and the CLIC Test Facility (CTF3) at CERN (Switzerland) are described.

3.1 Final Focus Test Beam

The FFTB was located at the end of the SLAC linac (SLC) (see Fig. 21), which was delivering an electron beam with an energy of about 46.6 GeV. At that time the SLC damping ring provided a normalised vertical emittance of $7{\cdot}10^{-7}$ m which however increases up to $2{\cdot}10^{-6}$ m after the beam reaches the end of the SLC linac. Table 6 summarises the most relevant parameters of the FFTB. FFTB extended over 200 m and was formed by five optical sections. The first one was a beta matching section (BM) for matching the optical functions at the end of the SLC to those of the FFTB. It contained quadrupoles magnets able to fully adjust the transverse phase space of the beam. The BM section was followed by two separated chromaticity correction sections, one for the horizontal (CCX) and one for the vertical (CCY) plane. Each one comprises sextupole magnets located at high dispersion regions in order to cancel the chromaticity introduced by the quadrupole magnets. The geometric aberrations were controlled by pairs of sextupoles placed at points of equal dispersion but spaced by a phase advance $n\pi$, where n is an integer. The lattice included a β-exchanger (BX) for matching the optics from one chromatic correction section to the other. The final doublet was embedded in the final transformer section (FT), it demagnified the beam size at the focal point. Figure 22 shows the structure of the FFTB beam line as an example of FFS based on the non-local chromaticity correction described in Section 1.2.1.1. The optical functions of the FFTB are corrected up to the third order [69] for the geometric and chromatic aberrations in which a relative energy

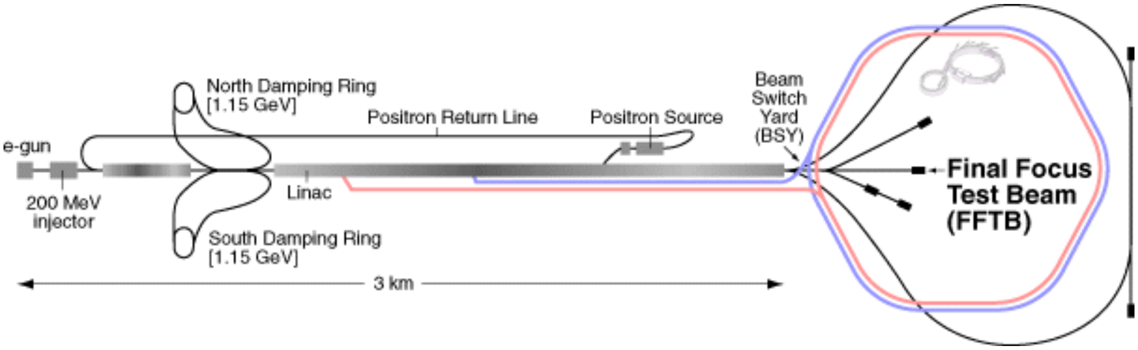

Figure 21: General scheme of the SLC facility, (Figure taken from [68]).

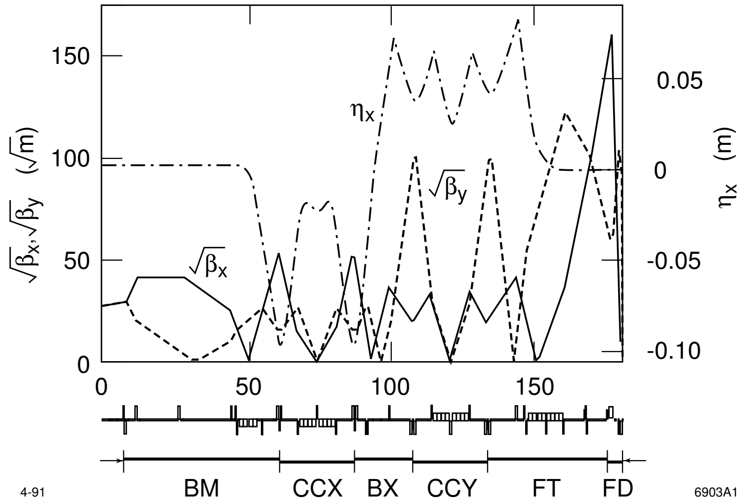

Figure 22: A scheme and optical functions of the final focus system of the FFTB (Figure taken from [22]).

spread of 0.3% was considered.

3.1.1 Performance of the FFTB

A stretched-wire [70] alignment system was used to align the magnet elements to the expected alignment of 100 and 60 μm in the horizontal and vertical planes respectively. Each quadrupole and sextupole magnet in the beam line was placed on a remotely-controllable support [71]. The precision of these movers allowed to implement beam based alignment procedures to improve the alignment of the magnets down to 10 μm on average in the vertical plane [72]. Each quadrupole and sextupole magnet was equipped with a strip-line Beam Position Monitor (BPM) capable to resolve the signal generated by a pulse of 10^{10} electrons displaced by 1 μm from the BPM center [73]. The vertical beam size measurement at the focal point of the FFTB was done by a Shintake monitor [34] with a resolution of about 10%.
The tuning procedure implemented to reach the measured 70 nm at the focal point of the FFTB consisted of the following 4 steps:

1. Beam based alignment: Each quadrupole and sextupole magnets were aligned by applying beam based techniques.

2. Lattice diagnostics: The optics of the beam line were checked in order to detect any strength error which would preclude to reach the design spot size.

3. Incoming beta match: In the matching section the $\beta_{x,y}$, $\alpha_{x,y}$ and the $\sigma_{x,y}$ were measured.

4. Tuning by orthogonal knobs [74]: The tuning of the spot size was done by scanning several orthogonal knobs and controlling the spot size measured by a spot-size monitor.

The orthogonal knobs which were found to be the most effective in tuning the FFTB were the horizontal and vertical dispersion, the horizontal and vertical waist motion and the coupling term $<p_x,y>$. These knobs were built by a combination of sextupole movers. Applying iteratively these knob scans a vertical beam size at the focal point below 100 nm was rapidly achieved. Further beam size reductions were obtained by scanning a set of non-linear knobs constructed as a combination of two normal and two trim skew sextupoles [66]. In May 1994 by relaxing the horizontal focusing in order to reduce the background signal, the smallest vertical spot size of 70 ± 7 nm was observed. The beam position jitter during the measurement was around 40 nm, which represents a significant contribution to the measured σ_y^* and it also represent a limiting factor for measuring smaller beam sizes, as explained in Ref. [75]. The measured vertical spot size at the focal point of the FFTB still remains as a world record.

3.2 Accelerator Test Facility

The Accelerator Test Facility consists of a linear accelerator (Linac) and a damping ring (DR). The linac delivers an electron beam with an energy equal to 1.3 GeV to the damping ring that reduces the ϵ_y to a value of 12 pm [76]. The ATF2 beam line was constructed in 2008 as an extension of the ATF damping ring.
Figure 23 shows a general scheme of the whole facility.

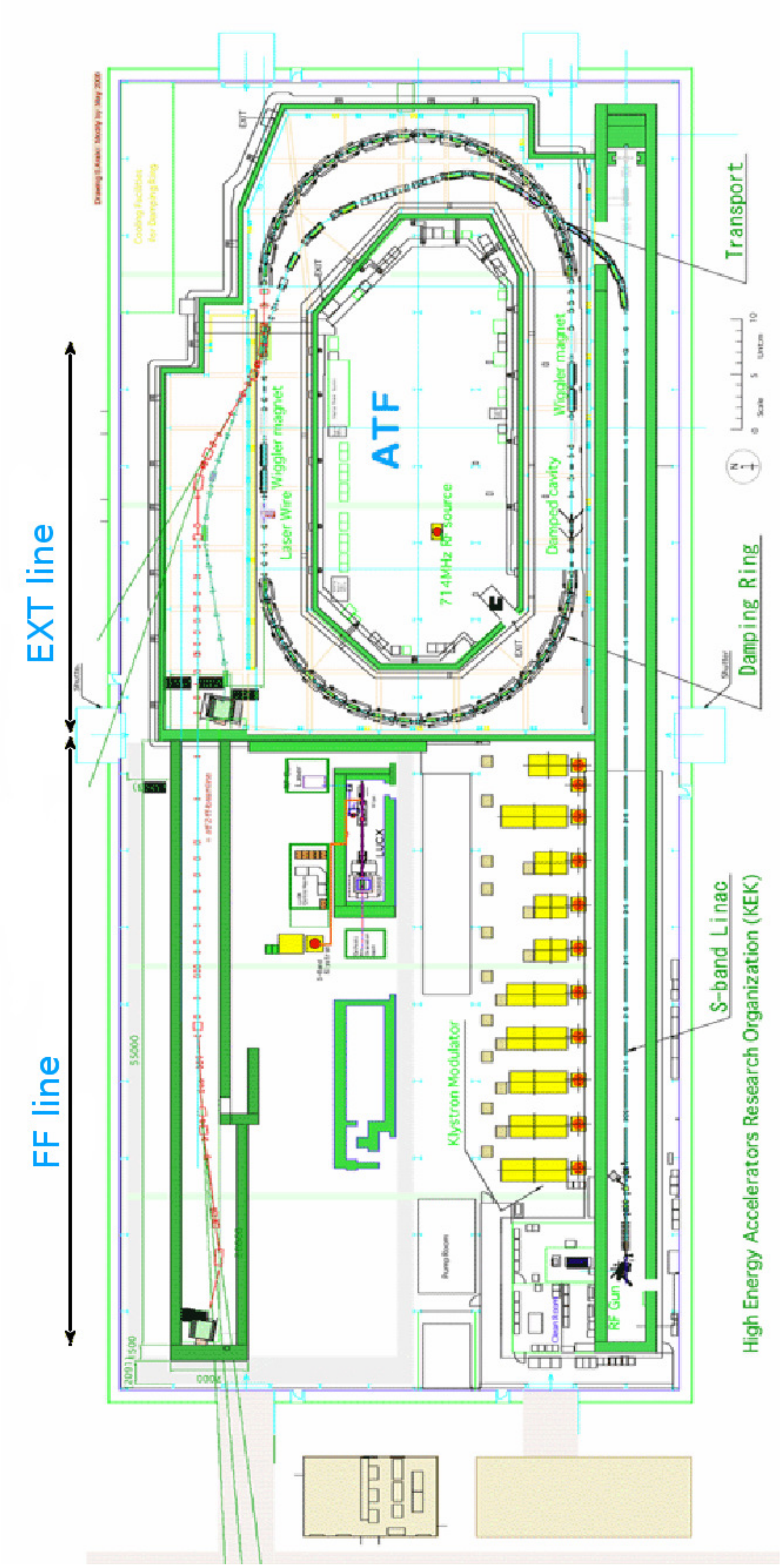

Figure 23: General scheme of the ATF and ATF2 facilities (Figure taken from [77]).

Parameter	Symbol	Value	Unit
Length	L	90.5	m
Energy	E	1.3	GeV
Relative energy spread	Δ_p	0.08	%
Normalised horizontal emittance	$\gamma\epsilon_x^*$	$5{\cdot}10^{-6}$	m
Normalised vertical emittance	$\gamma\epsilon_y^*$	$3{\cdot}10^{-8}$	m
Horizontal beta function at the IP	β_x^*	4	mm
Vertical beta function at the IP	β_y^*	0.1	mm
Horizontal beam size at the IP	σ_x^*	2.8	μm
Vertical beam size at the IP	σ_y^*	38.0	nm
Free distance before the IP	L*	1.0	m
Vertical chromaticity	ξ_y	10000	

Table 7: Main design parameters of the ATF2 Nominal lattice.

3.2.1 ATF2

The ATF2 beam line extends over about 90 meters from the beam extraction point in the ATF DR to the IP[§]. Figure 24 shows a scheme of the ATF2 beam line. The goals of the ATF2 experiments are taking advantage of the small emittances produced at the ATF DR: focusing the beams to tens of nanometres scale vertical beam size and providing a nanometre level stability. The first goal of ATF2 is to obtain a vertical spot size at the IP of about 38 nm by means of the ATF2 Nominal lattice which is the scaled-down version of the ILC FFS [9]. A detailed description of the ATF2 beam line is given in Refs. [77], [78]. Table 7summarises the most relevant parameters of the ATF2 Nominal lattice.

In addition to the ATF2 Nominal lattice, the ATF2 Ultra-low β^* lattice is a proposal [79] to test the feasibility for an even larger chromaticity lattice as the CLIC BDS. The ATF2 Ultra-low β^* proposal is an even more advanced optics with a value of β_y^* equal to 25 μm (see Ref. [80]), which represents a quarter of that one of the ATF2 Nominal lattice. The expected vertical σ_y^* is about 23 nm.

Table 8 shows the relevant parameters of the FFTB, ATF2, CLIC and ILC designs, with special attention to the vertical chromaticity defined by Eq. (28). The calculated values of the vertical chromaticity of ATF2 Ultra-low β^* lattice is almost 4 times that one of the ATF2 Nominal lattice. A comparable value of ξ_y is obtained between the CLIC designs and the ATF2 Ultra-low β^* one.

The ATF2 beam line can be divided into two sections, the extraction beam line (EXT) and the final focus system (FFS). The EXT beam line extends over 52 m, it comprises an extraction and a diagnostics section. The diagnostics section is used for measuring the emittance, Twiss functions, dispersion and transverse coupling. The emittance and the Twiss functions are measured at one location by a quadrupole scan or at several locations as described in [81] by means of five wire scanners [82] namely MW0X, MW1X, MW2X, MW3X and MW4X or alternatively by four Optical Transition Radiation (OTR) monitors [83] namely OTR0X, OTR1X, OTR2X, OTR3X. Knowing the Twiss functions at the exit of the EXT beam line is crucial for matching them with the FFS beam line by optimising the matching quadrupole magnets of the downstream beam line.

The dispersion is measured by the orbit displacement at the BPMs when changing the energy of the beam by means of the radio-frequency cavity of the DR. The dispersion is corrected by the correctors labelled as ZH and ZV or by changing the strength of the quadrupoles located at high dispersion

---

[§] Despite the fact that ATF2 is not a collider the focal point of the beam line is referred as the interaction point (IP).

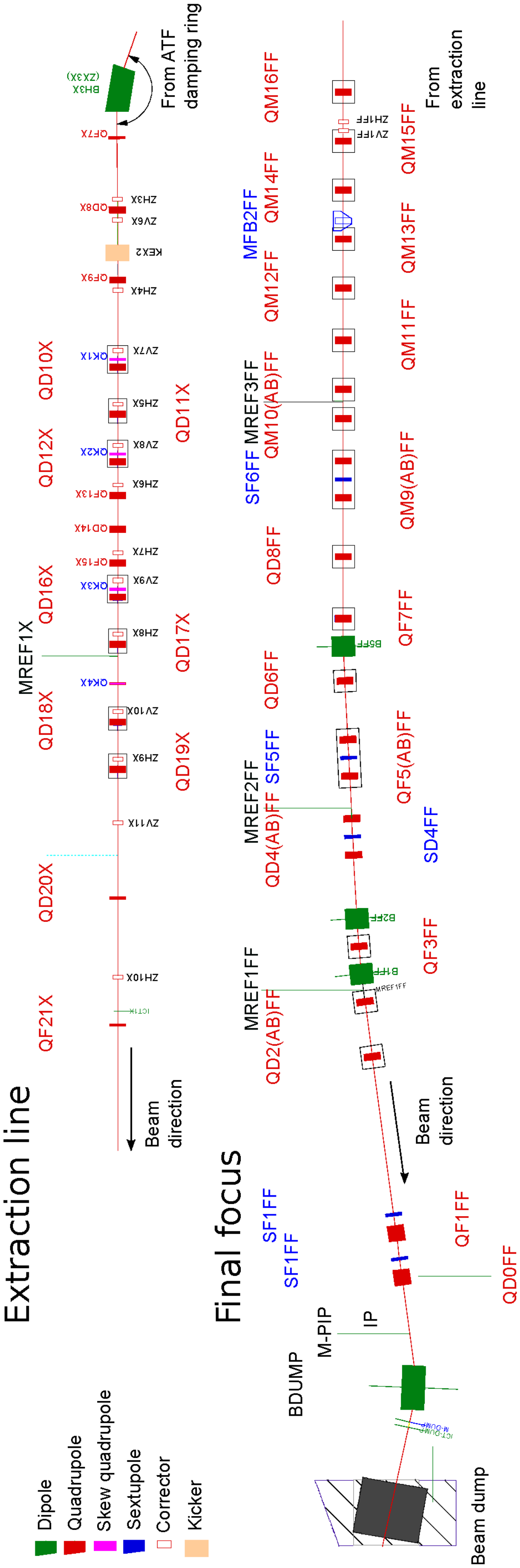

Figure 24: Scheme of the ATF2. The beam line on the left represents the extraction beam line (EXT). The beam line on the right represents the FFS as the continuation of the EXT line (Figure courtesy of S. Boogert).

	Status	Energy [GeV]	$\gamma\epsilon_y^*$ [nm]	σ_y^* [nm]	β_y^* [mm]	L* [m]	ξ_y
FFTB	Designed	46.6	2000	52	0.1	0.4	17000
FFTB	Measured	46.6	2000	60	0.167	0.4	10000
ATF2 Nominal	Designed	1.3	30	38	0.1	1.0	6700
ATF2 Ultra-low β^*	Proposed	1.3	30	23	0.025	1.0	25000
CLIC L*= 3.5 m	Designed	1500	20	1	0.069	3.5	31000
CLIC L*= 6 m	Designed	1500	20	1.1	0.12	6.0	30000
ILC	Designed	250	40	5.7	0.4	3.5	15000

Table 8: Relevant parameters of different projects. The last column gives the vertical natural chromaticity ξ_y which has been evaluated according to Eqs. (46) and (47) for the CLIC and ATF2 cases. The ξ_y for the FFTB and ILC lattices have been obtained from Refs. [9] and [22], respectively.

regions, more details can be found in [84]. The transverse coupling is corrected by means of four skew quadrupoles namely QK1X, QK2X, QK3X, QK4X. All the presented components can be identified in Fig. 24. Figure 25 shows the β-functions and the dispersion along the EXT beam line.

3.2.1.1 ATF2 FFS

The ATF2 FFS beam line is the first constructed final focus system based on the novel local chromaticity correction scheme described in [16]. The ATF2 final focus system extends over 40 m, it goes from the end of the EXT line up to the IP. It consists of a matching section composed of 6 quadrupole magnets denoted by QM16FF, QM15FF, QM14FF, QM13FF, QM12FF and QM11FF whose function is to match the β-functions measured at the exit of the EXT beam line, as described in Section 3.2.1. In addition there are 14 quadrupole magnets which transport the beam to the final doublet that include one focusing quadrupole (QF1FF) and one defocusing (QD0FF) meant to focus the beam at the IP. 3 bending magnets, namely B1FF, B2FF and B5FF, generate the required dispersion to correct the chromaticity, as described in Section 2.1.3 by means of the 5 sextupoles, namely SF6FF, SF5FF, SD4FF, SF1FF and SD0FF. An important feature of the FFS is that the phase advance between the sextupoles and the IP satisfies the condition $\Delta\varphi_{x,y} = \pi/2 + n\pi$, where n is an integer. Figure 26 shows the $\beta_{x,y}$ and η_x-functions along the FFS beam line.
A Shintake monitor is installed at the IP for measuring the beam size, its design is described in [85]. It detects the Compton scattered photons coming from the interaction between the electron beam and the interference fringe pattern created by two laser beams. This enables to obtain σ_y^*. In Section 2.1.2.1 a description of the Shintake monitor operation and its characteristics are given.
To reach small beam sizes at the IP of the ATF2 beam line, small emittances and strong focusing are required, that imply tight constraints on the design and machining of the FFS magnets. Because of this, the multipole components of the ATF2 FFS magnets have been measured independently by two groups. The effect of the measured multipole components on the IP beam sizes is addressed in this thesis. The FD quadrupole magnets require a dedicated treatment in terms of its integration, alignment, stability and field quality (see Refs. [86] and [87]). The tolerances of the FD quadrupole magnets of the ATF2 Nominal and Ultra-low β^* lattices are also obtained and discussed in Section 4.2.3.

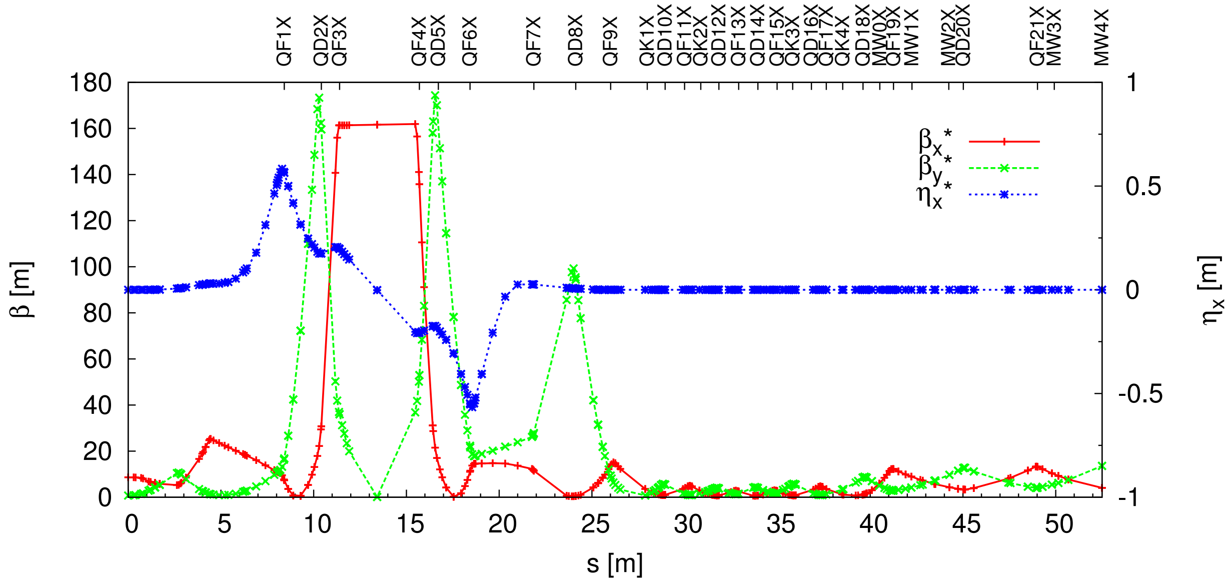

Figure 25: The $\beta_{x,y}$-functions and the η_x-function throughout the ATF2 extraction line.

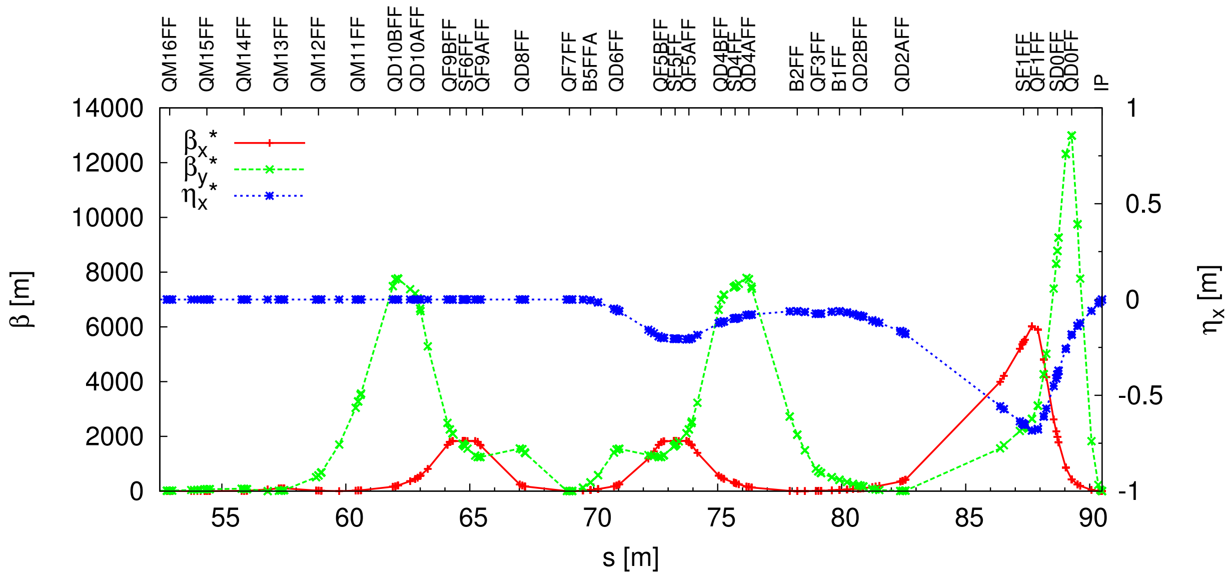

Figure 26: The $\beta_{x,y}$-functions and the η_x-function for the ATF2 Nominal lattice throughout the ATF2 final focus line.

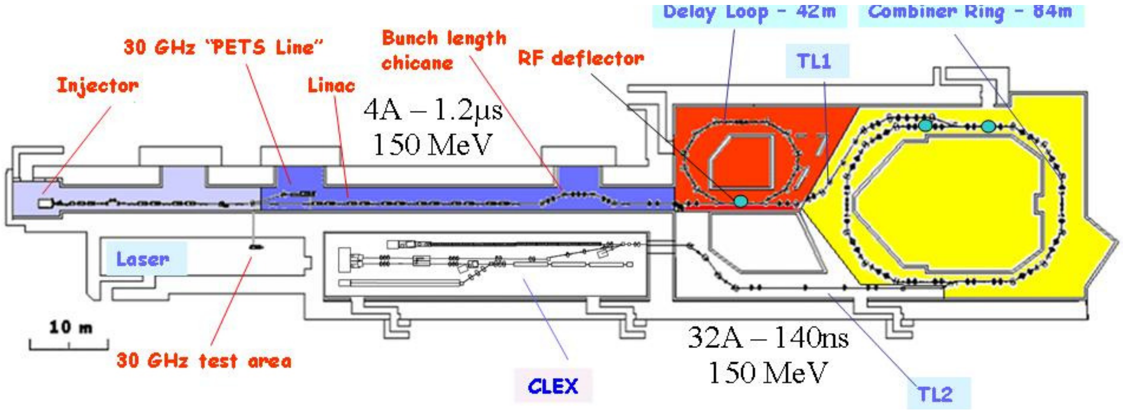

Figure 27: Layout of the CLIC Test Facility 3. The Test Beam Line is in the CLEX area at the bottom. (Picture taken from [90]).

3.3 CLIC Test Facility 3

The CLIC acceleration scheme is based on the two-beam acceleration concept as described in Section 1.2. The CLIC Test Facility (CTF3) [88] was built to demonstrate (i) the generation of a high intensity beam and (ii) the feasibility of this novel two-beam acceleration concept. In the CLIC experimental area (CLEX) of CTF3 two main experiments are taking place, namely the two-beam acceleration and the stable deceleration of the drive beam.

The source of the drive beam generator is a thermionic gun, which emits electrons in a continuous stream. The bunch train is divided into 140 ns sub-trains, and after an acceleration in a linac half of the sub-trains are sent into a delay loop (see Fig. 27). After one turn they are interleaved with the rest of the sub-trains, thereby increasing the frequency and beam current by a factor of 2. This beam is then sent into a combiner ring through the transfer line TL1, which performs a second multiplication by interleaving four sub-trains. The final pulses have a high-frequency of 12 GHz, and a high-current of 28 A. After the recombination, the beam enters the CLEX area through TL2 (see Fig. 28). This area houses the two main experiments. One of them is performed at the Two-Beam Test Stand (TBTS), and its aim is to demonstrate the two-beam acceleration by using the drive beam to accelerate a probe beam. The second experiment takes place at the TBL, it is designed to show a stable and efficient transport of a heavily decelerated beam (see Ref. [89]).

3.3.1 Test Beam Line

The TBL is located at the CLEX area of CTF3. A detail scheme of the CLEX area is shown in Fig. 28. TBL is a periodic structure of 8 FODO cells. Each cell contains two Power Extraction and Transfer Structures (PETS), two BPMs, one focusing quadrupole and one defocusing quadrupole magnet. The magnets are mounted on mechanical movers. There are also 3 conventional orbit corrector magnets in the lattice at the beginning of the TBL beam line. Figure 29 shows the scheme of the TBL components and the β-functions along the TBL beam line.

The beam line was commissioned in 2010, its detailed description is given in [91]. The nominal parameters of the TBL beam are summarised in Table 9.

The TBL is a prototype of the CLIC decelerator, though some of its parameters are different. For instance, the CLIC drive beam current is 4 times higher than the TBL beam. However the CLIC PETS length is roughly a quarter of the TBL PETS length, thus the power produced in each PETS

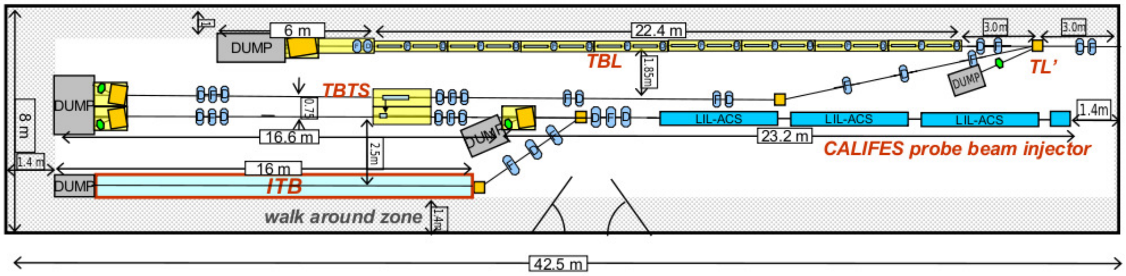

Figure 28: Scheme of the CLEX area. TBL is located in the upper part of the figure while the TBTS is located in the lower part of the figure. (Picture taken from [90])

Beam Parameter	Value	Unit
Initial Energy	150	MeV
Final Energy	67	MeV
Energy extraction efficiency	55	%
Bunch charge	2.3	nC
Bunch length	1.0	mm
Bunch spacing	83	ps
Pulse duration	140	ns
Pulse current	28	A
Normalised vertical emittance	150	μm

Table 9: Nominal parameters of the TBL.

is of the same order.

The TBL is designed to study and validate the drive beam stability during its deceleration. The transport efficiency of the beam with a very high energy spread along the beam line without significant beam losses is a concern. Simulations show that if the quadrupoles of the TBL are randomly misaligned by more than 25 μm, significant beam losses occur when the beam is heavily decelerated by the PETS as it can be seen in Fig. 30, see Ref. [92] for more details. This effect is due to the dispersion generated by the offset quadrupoles according to Eq. (50) which in combination with the energy spread growth due to the beam deceleration leads to beam size increase along the TBL beam line as it can be seen in Fig. 31. The beam based alignment resolution of the TBL quadrupole magnets is studied in this thesis with special attention to the resolution limitations.

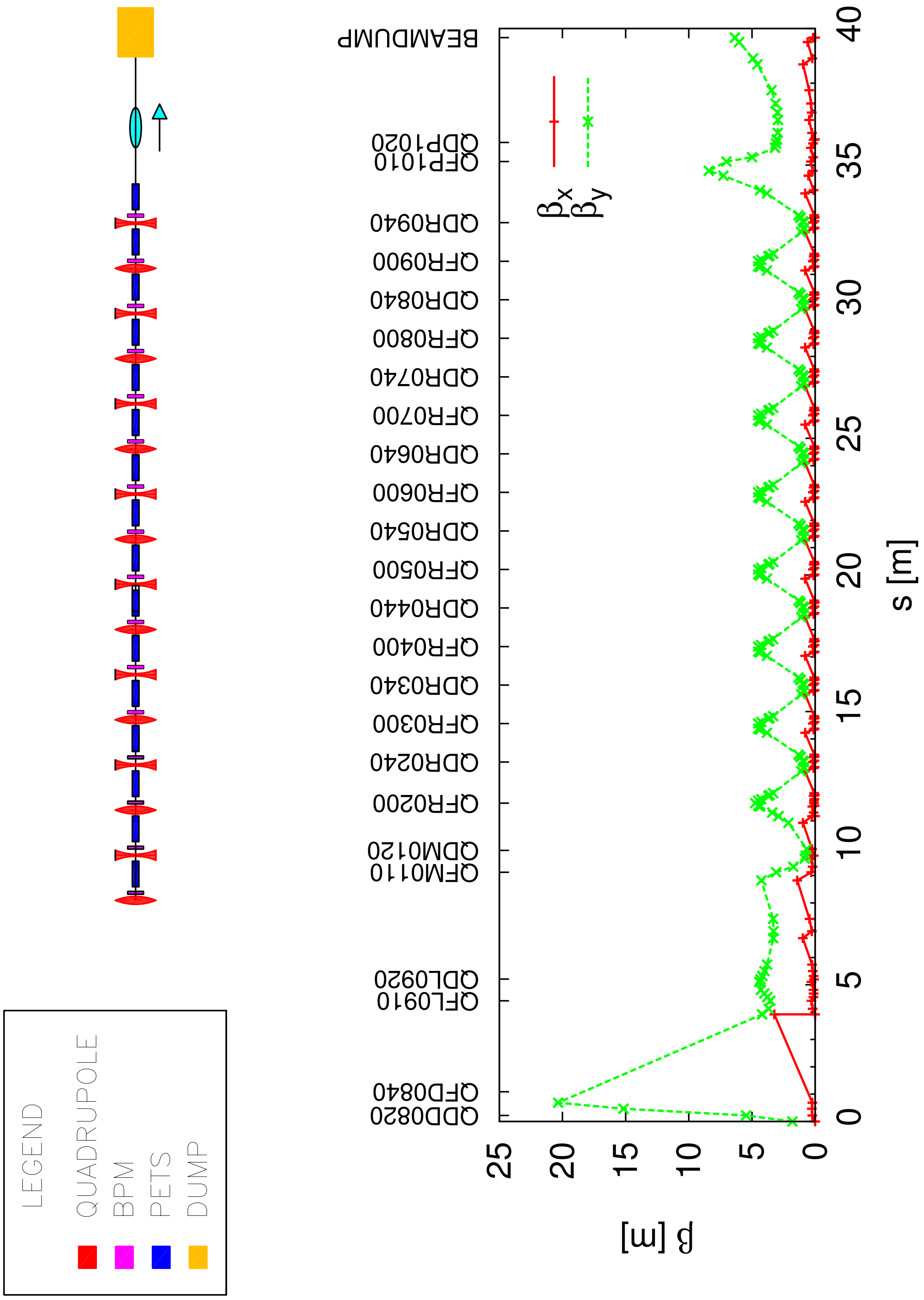

Figure 29: β-functions along the TBL. The legend on the left indicates the TBL components.

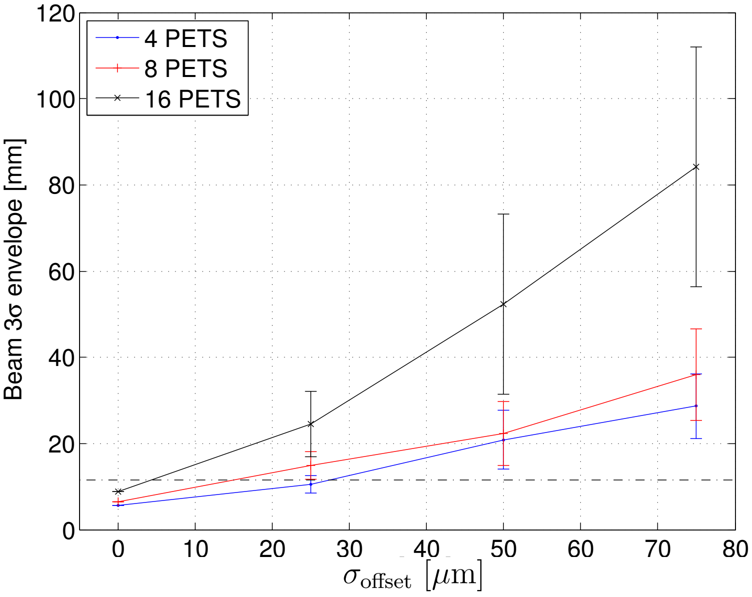

Figure 30: 3 σ_x beam envelope at the TBL quadrupoles with the magnets displaced by different values of σ_{offset}. Three different scenarios (blue, red and black) depending on the numbers of PETS installed at the TBL, are considered in simulations. The dash line represents the beam pipe aperture of TBL (Figure courtesy of G. Sterbini).

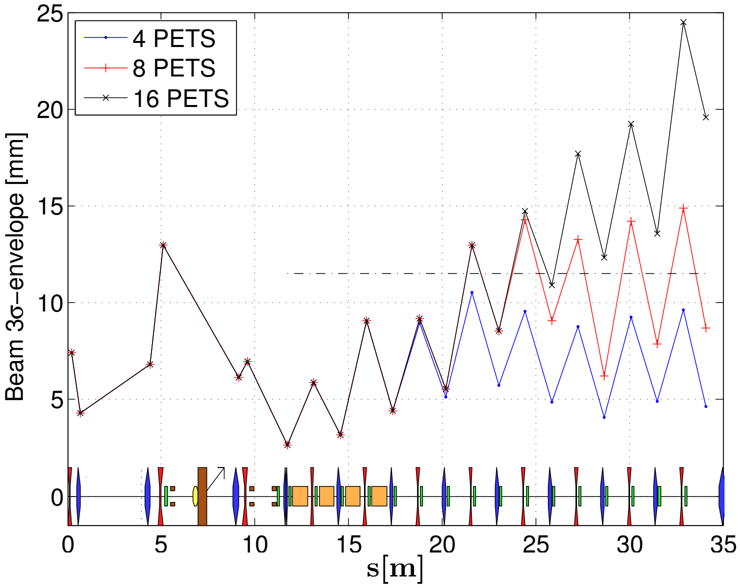

Figure 31: 3 σ_x beam envelope along the TBL with the quadrupole magnets randomly misaligned by 25 μm. Three different scenarios (blue, red and black) depending on the numbers of PETS installed at the TBL, are considered in simulations. The dash line represents the beam pipe aperture of TBL (Figure courtesy of G. Sterbini).

4 FFS lattice design and optimisation

In this section the optimisation of the CLIC BDS baseline design and ATF2 lattices are described. According to the CLIC BDS baseline design the crossing angle between the electron and positron beams at the IP is 20 mrad. To prevent a luminosity loss due to the non-zero crossing angle a single crab cavity per beam line is foreseen to provide the head-on collisions at the IP. However, it has been recently found that the crab cavity only recovers up to 95% of the design luminosity [93] and in addition the vertical beam size increases by about 1%. In this section different solutions to recover the design luminosity are described.

The ATF2 IP beam sizes simulated with the measured multipole components of the ATF2 magnets are well above the design beam sizes. From the analysis of the high order aberrations on the IP beam sizes possible solutions that minimise the detrimental effect of the measured multipole components are inferred. By combining different solutions new ATF2 Bx2.5By1.0 and ATF2 Ultra-low β_y^* lattices are designed, which preserve the design vertical IP spot size for each of them.

4.1 CLIC BDS lattice optimisation

The CLIC BDS baseline design is described in Section 1.2. The luminosity given in Table 2 corresponds to the CLIC BDS baseline design assuming head-on collisions $\mathcal{L}_{(\text{head}-\text{on})}$. In reality the electron and positron beams cross at an angle of 20 mrad to allow the extraction of the spent beams. For such crossing scheme the luminosity is reduced with respect to the head-on luminosity. For small crossing angles and if the condition $\sigma_x^* \ll \sigma_z^*$ is satisfied, the reduction of the geometric luminosity is expressed by the following relation [93]:

$$\mathcal{L} = \mathcal{L}_{(\text{head}-\text{on})} \frac{1}{\sqrt{1+\Theta^2}}, \tag{74}$$

where Θ is the Piwinski angle defined as:

$$\Theta = \frac{\tan\left(\frac{\theta_c}{2}\right) \sigma_z^*}{\sigma_x^*}, \tag{75}$$

where θ_c is the crossing angle of the beams and σ_x^* and σ_z^* are the horizontal and longitudinal beam sizes at the IP. According to the CLIC BDS baseline design parameters shown in Table 2 a luminosity loss about 90% is obtained. In order to preserve the required luminosity R. Palmer introduced the concept of crab cavity [94]. This cavity deflects the head and the tail of the bunch horizontally in opposite directions so that after flying the distance between the crab cavity and the collision point, the bunches are perfectly aligned with respect to each other, as shown in Fig. 35.

For the CLIC BDS baseline design the insertion of one 2.6 MV crab cavity per beam line before the FD is planned as Fig. 32 shows, more details can be found in Refs. [95] and [96]. In previous studies with a single crab cavity located prior to the FD a luminosity loss of 5% with respect to $\mathcal{L}_{(\text{head}-\text{on})}$ of the CLIC baseline design was obtained [93]. The goal of the study in the present thesis is to understand this 5% luminosity loss and to look for solutions that allow to fully recover the design luminosity.

4.1.1 MAPCLASS 6 coordinates

Part of the optimisation process is carried out by the MAPCLASS code [38]. As described in Section 2.2 the PTC [54] module of MADX [55] can provide the map coefficients up to 6 coordinates,

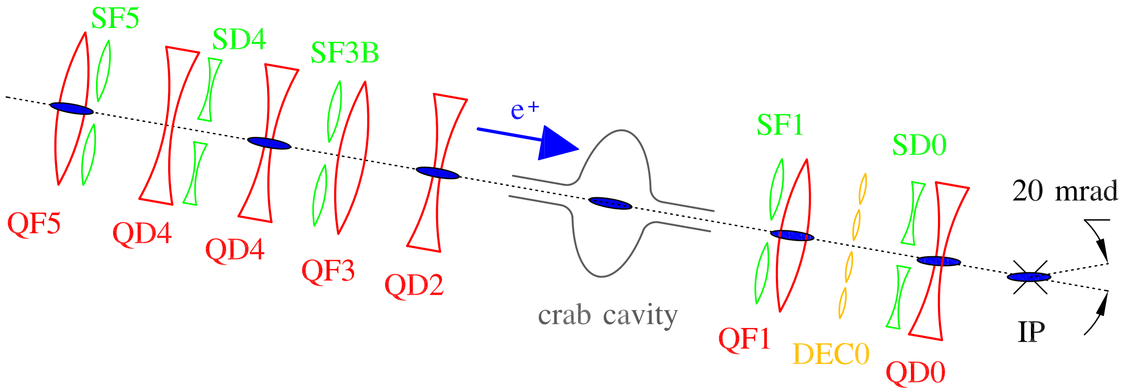

Figure 32: Scheme of the bunch rotation by the crab cavity prior to the collision at the IP according to the CLIC BDS baseline design. Quadrupole, sextupole and the decapole magnets are in red, green and yellow colours, respectively. (Figure not to scale).

namely x, p_x, y, p_y, z and δ_p. However the MAPCLASS code operates with 5 coordinates. In order to optimise the higher order aberrations in the presence of the crab cavity it is required to extend MAPCLASS to 6 coordinates (MAPCLASS-6C).

By analogy with the transfer map defined by Eq. (42) in Section 2.2, a map of 6 coordinates can be written in the form:

$$u_{\mathrm{f},i} = \sum_{jklmnp} X_{i,jklmnp} \; x_0^j \, p_{x0}^k \, y_0^l \, p_{y0}^m \, \delta_p^n \, z_0^p \tag{76}$$

where $u_{\mathrm{f},i}$ represents any of the final coordinates $(x,\, p_x,\, y,\, p_y,\, z)$ and $\delta_p = \frac{p-p_0}{p_0}$. The initial coordinates are labelled with the zero sub-index. The $X_{i,jklmnp}$ are the map coefficients provided by the PTC module of MAD-X and the maximum order of the map is $N_\mathrm{order} = j+k+l+m+n+p$. The standard deviation of the final density distribution $\widehat{\sigma_\mathrm{f}}$[¶] for 6 coordinates is obtained by adding the longitudinal coordinate to Eq. (45) as the following relation shows:

$$\begin{aligned} \widehat{\sigma_\mathrm{f}}^2 &= \langle u_{\mathrm{f},i}^2 \rangle - \langle u_{\mathrm{f},i} \rangle^2 = \sum_{\substack{jklmnp \\ j'k'l'm'n'p'}} X_{i,jklmnp} X_{i,j'k'l'm'n'p'} \int \; x_0^{j+j'} \, p_{x0}^{k+k'} \, y_0^{l+l'} \, p_{y0}^{m+m'} \, \delta_p^{n+n'} \, z_0^{p+p'} \; \rho_0 d\nu_0 \; - \\ &\qquad \left(\sum_{jklmnp} X_{i,jklmnp} \int \; x_0^j \, p_{x0}^k \, y_0^l \, p_{y0}^m \delta_p^n \, z_0^p \, \rho_0 \, d\nu_0 \right)^2 \end{aligned} \tag{77}$$

In order to validate the MAPCLASS-6C, it has been cross-checked with tracking simulations. Figure 33 shows the IP beam size calculated with the MAPCLASS-6C and the rms beam size obtained by tracking 10^5 particles for different values of voltage of the crab cavity. The observed agreement between the two methods is evident.

The crab cavity kicks the particles in the horizontal plane according to their longitudinal position, for simplicity it is assumed that the crab cavity rotates the beam in the x-z plane by a certain angle θ_c. Thus the following step consists in rotating the plane defined by the x, z coordinates in order to evaluate the intrinsic beams size instead of the projected one. The coordinates in the rotated reference

---

[¶] It should be noticed that $\widehat{\sigma_x^*}$ is the projected beam size of a rotated bunch.

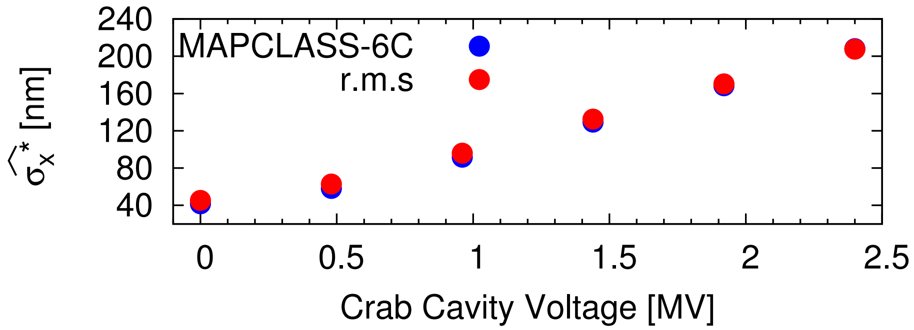

Figure 33: Comparison of $\widehat{\sigma_x^*}$ evaluated by MAPCLASS-6C (blue colour) and by tracking 10^5 particles (red colour) for different voltages of the crab cavity.

system, denoted as $x_\mathrm{f}^{\theta_c}$ and $z_\mathrm{f}^{\theta_c}$ are related to x_f and z_f by the following formula:

$$\begin{pmatrix} x_\mathrm{f}^{\theta_c} \\ z_\mathrm{f}^{\theta_c} \end{pmatrix} = \begin{pmatrix} \cos\theta_c & -\sin\theta_c \\ \sin\theta_c & \cos\theta_c \end{pmatrix} \begin{pmatrix} x_\mathrm{f} \\ z_\mathrm{f} \end{pmatrix} \tag{78}$$

Since $\sigma_{x_\mathrm{f}} \ll \sigma_{z_\mathrm{f}}$ and θ_c is small enough, it is justified to assume $z_\mathrm{f}^{\theta_c} \approx z_\mathrm{f}$, hence $x_\mathrm{f}^{\theta_c}$ can be expressed as:

$$x_\mathrm{f}^{\theta_c} = \cos\theta_c \sum_{jklmnp} X_{x,jklmnp}\, x_0^j\, p_{x0}^k\, y_0^l\, p_{y0}^m\, \delta_p^n\, z_0^p - z_0 \sin\theta_c \tag{79}$$

4.1.2 Beam size analysis with MAPCLASS-6C

In the present study a Gaussian distribution of the spatial coordinates x, y, p_x, p_y, z and a uniform distribution in relative momentum deviation δ_p are assumed. In fact, the particle bunch coming from the main linac is likely to have a correlation between z and δ_p, however this is neglected in the following analysis.

The obtained vertical IP spot size according to Eq. (76) is 1% larger than the one obtained by Eq. (42). An analysis of the map coefficients by MAPCLASS-6C when switching on/off the crab cavity of the CLIC BDS baseline design reveals which terms give the main contributions to the observed σ_y^* growth.

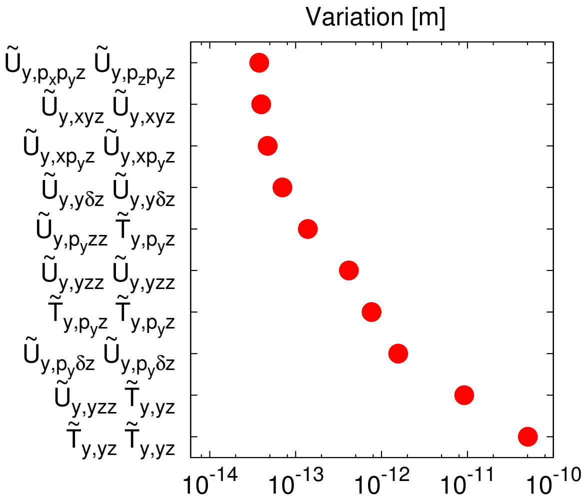

Figure 34: The 10 most important variations of the MAPCLASS coeficients when switching on/off the crab cavity.

Let us define the following quantities:

$$\tilde{T}_{y,yz}\tilde{T}_{y,yz} = \sqrt{\int X_{y,001001}X_{y,001001}\ y_0^2\ z_0^2\ \rho_0\ dy_0\ dz_0}, \tag{80a}$$

$$\tilde{U}_{y,yzz}\tilde{T}_{y,yz} = \sqrt{\int X_{y,001002}X_{y,001001}\ y_0^2\ z_0^3\ \rho_0\ dy_0\ dz_0}, \tag{80b}$$

$$\tilde{U}_{y,p_y\delta z}\tilde{U}_{y,p_y\delta z} = \sqrt{\int X_{y,000111}X_{y,000111}\ p_{y0}^2\ \delta_p^2\ z_0^2\ \rho_0\ dp_{y0}\ d\delta_p\ dz_0}, \tag{80c}$$

$$\tilde{T}_{y,p_yz}\tilde{T}_{y,p_yz} = \sqrt{\int X_{y,000101}X_{y,000101}\ p_{y0}^2\ z_0^2\ \rho_0\ dp_{y0}\ dz_0}, \tag{80d}$$

$$\text{where} \quad \rho_0 = \frac{e^{-x^2/2\sigma_x^2}\ e^{-p_x^2/2\sigma_{px}^2}\ e^{-y^2/2\sigma_y^2}\ e^{-p_y^2/2\sigma_{py}^2}\ e^{-z^2/2\sigma_z^2}\ \Pi(\frac{\delta_p}{\Delta_p})}{(2\pi)^{2.5}\sigma_x\sigma_{p_x}\sigma_y\sigma_{p_y}\sigma_z\Delta_p}, \tag{80e}$$

$$\text{where} \quad \Pi\left(\frac{\delta_p}{\Delta_p}\right) = \begin{cases} \frac{1}{2}\Delta_p & \text{if} \quad |\delta_p| \le \Delta_p \\ 0 & \text{if} \quad |\delta_p| > \Delta_p \end{cases} \tag{80f}$$

When switching on the crab cavity the variation of the coefficient $\tilde{T}_{y,yz}$ is larger than the others as $\tilde{U}_{y,yzz}$, $\tilde{U}_{y,p_y\delta z}$ and $\tilde{T}_{y,p_yz}$ as it is shown in Fig. 34. When the crab cavity is off all these coefficients are equal to zero. These terms are related to the map coefficients $X_{y,jklmnp}$ by Eqs. (80) and correlate either the y or p_y with the z coordinate due to the quadrupole introduced by the feed-down of the FD sextupoles located downstream the crab cavity when an off x-axis particle goes through.
The observed correlation between the y and p_y coordinates with z indicates the presence of a travelling waist [97] at the IP.

4.1.3 Possible Solutions

The travelling waist phenomenon refers to the change of the position of the betatron waist versus the z coordinate. For the CLIC BDS baseline design the crab cavity is designed to kick the head of the bunch in one direction, while the tail of the bunch is kicked in the opposite direction. Thus, from the feed-down of a horizontal offset at the sextupoles, particles experience different focusing, as Eq. (54) shows, that leads to a travelling waist at the IP. The overall picture is that the waist moves from the tail to the head of the bunch, contrary to what it is desired during the beam collision. According to the CLIC BDS baseline design the waist should move from the head to the tail of the bunch [98].
In the following discussion all the presented luminosity values are calculated by J. Barranco using GUINEA-PIG, while I compute the beam sizes by the MAPCLASS-6C code.
Possible solutions to recover the observed 5% luminosity loss are the following:

- a scheme with 2 crab cavities per beam line [99],
- new crab cavity location,
- opposite crossing angle.

These solutions are described below:

4.1.3.1 2 crab cavities scheme

As suggested in [99], a second crab cavity might compensate the beam aberrations generated by the downstream sextupole magnets of the first crab cavity. Keeping the original cavity at the same location and inserting a second crab cavity 5 m upstream the first one with voltages of -2.4 MV and 5 MV respectively, enables to recover the luminosity up to 98.5% of $\mathcal{L}_{(\text{head-on})}$.

4.1.3.2 New crab cavity location

Placing the crab cavity at a different location might help to compensate the aberrations introduced by the magnets between the crab cavity and the IP. In total 4 different locations have been analysed, denoted here as P_1, P_2, P_3, P_4, whereas P_0 represents the design location.
Locations P_4 and P_1 for which the crab cavity is placed before the SD4 and SD0 sextupole magnets, respectively, fully recover the $\mathcal{L}_{(\text{head-on})}$, in terms of IP beam sizes there is a negligible increase in both cases. This indicates an overall compensation of the tail-to-head travelling waist. Placing the crab cavity at P_2 which is in front of the decapole magnet 97.6% of the $\mathcal{L}_{(\text{head-on})}$ is achieved. The obtained $\mathcal{L}$ when the crab cavity is placed at P_3 which is in front of QF1 magnet is slightly better than the one obtained placing the crab cavity at P_0. Table 10 summarises the relative $\Delta\sigma_x^*$, $\Delta\sigma_y^*$ and $\mathcal{L}/\mathcal{L}_{(\text{head-on})}$ for the crab cavity positions P_0, P_1, P_2, P_3, P_4 with respect the design luminosity and beam sizes.

4.1.3.3 Opposite crossing angle

Swapping the crossing angle of the CLIC BDS baseline design from 20 mrad to -20 mrad as shown in Fig. 35 requires a change in the sign of the crab cavity kick, bringing the movement of the waist from the head to the tail of the bunch, thus following the collision process as reported in [100]. In this opposite crossing scheme scenario the obtained luminosity is 99.2% of $\mathcal{L}_{(\text{head-on})}$. Initially it was thought that the sign of the crossing angle was a free parameter due to reasons of symmetry,

Position	Next magnet after the CC	Distance to IP [m]	R_{12} [m]	V [MV]	$\Delta\sigma_x^*/\sigma_x^*$ [%]	$\Delta\sigma_y^*/\sigma_y^*$ [%]	$\mathcal{L}/\mathcal{L}_{(\mathrm{head-on})}$ [%]
P_1	SD0	6.7	10.32	5.8	0.005	0.05	99.5
P_2	DEC0	7.2	11.01	5.4	6.8	0.15	97.6
P_3	QF1	11.8	24.12	-2.5	4.5	1.2	95.3
P_0 (design)	SF1	14.0	23.41	2.6	4.7	1.0	95.0
P_4	SD4	268.6	-12.98	-4.6	0.3	0.04	100.0

Table 10: Luminosity and beam sizes at the IP for different positions of the crab cavity. P_0 corresponds to the position by design.

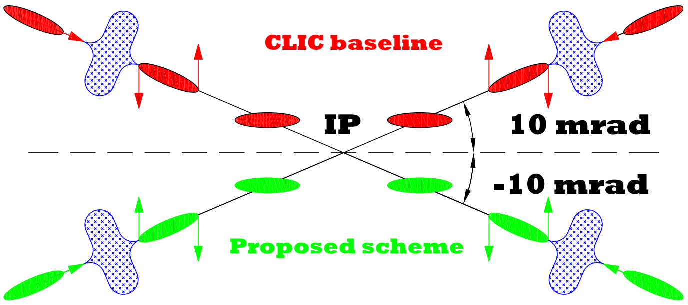

Figure 35: Crab crossing scheme for the CLIC baseline design (red colour) and the new proposed crossing scheme with opposite angle (green colour). The red and green arrows indicate the propagation of the particles in the horizontal plane. Blue elements represent the crab cavities.

nevertheless there is a preferred crossing angle imposed by the combination of the crab cavity voltage with the downstream sextupole magnets.

4.1.4 Summary of the solutions

The 5% luminosity loss observed when crossing the beams at the IP by 20 mrad with a single crab cavity is due to a motion of the waist from the tail to the head of the bunch during collision. This phenomenon is produced by the offset sextupole magnets located downstream the crab cavity. Locating the crab cavity in front of the SD4 or SD0 magnets fully recovers the design luminosity, but these locations are not considered due to the large distance between SD4 and the IP and space limitations respectively. Inserting a second crab cavity partially recovers the luminosity with a residual luminosity loss of 2.5%. Otherwise, keeping the single crab cavity scheme at the design position and crossing the beams at an angle of -20 mrad recovers the luminosity up to 99.2%. In absence of civil engineering constraints, the latter solution would be the preferred one because it does not require an additional cost.

4.2 ATF2 lattice design

This section presents the results of the design and optimisation of the ATF2 lattices in the presence of field quality measurements of the magnets. The analysis capabilities of the MAPCLASS[‖] code have been extensively used to mitigate the detrimental effect of the measured multipole components of the ATF2 magnets on the vertical beam size at the IP. In accordance with previous field quality

---

[‖] In this study the MAPCLASS 5-coordinates described in Section 2.2 is the one used for the design and optimisation.

measurements of the magnets performed at IHEP it was decided to insert a skew sextupole magnet to compensate the skew sextupole component present in the ATF2 quadrupole magnets. However new data on the multipole components of the magnets was obtained after a careful cross-check between the results of the IHEP and the later KEK measurement campaign [101]. This analysis allows to determine the ultimate multipole components of the ATF2 magnets. To mitigate the impact of these multipole components on the performance of the ATF2 lattices the following solutions have been studied:

- replacing the final doublet by better field quality quadrupoles,
- sorting the quadrupoles according to their field quality,
- modifying the lattice optics.

According to the possible cures mentioned above, for the ATF2 Nominal lattice two solutions are proposed. It is sufficient to replace the FD and to sort the remaining quadrupole magnets according to their skew sextupole component, or alternatively to increase by a factor 2.5 the nominal β_x^*. Both solutions recover the design σ_y^*. The later solution is described in Section 4.2.5, this new design is called ATF2 Bx2.5By1.0 lattice and it was used for the ATF2 experimental session in December 2010. The MAD-X model of this new lattice is available at the ATF2 web repository [102].

Regarding the ATF2 Ultra-low β^* lattice it is required to replace the FD, to sort the remaining quadrupole magnets according to their skew sextupole component and to increase by a factor 3/2 the design β_x^*. The new design is called the ATF2 Ultra-low β_y^* lattice, that reaches a vertical spot size at the IP equal to 27 nm, 25.6±0.2 nm and 21.2±0.3 nm according to the rms, Shintake and core beam size definitions, respectively. These definitions are given in Section 2.1.2 [**]. The MAD-X model of this new lattice design is available at the ATF2 web repository [103].

4.2.1 Initial estimates of multipole components of the ATF2 magnets

The ATF2 beam line is composed of 7 bending, 43 quadrupole and 5 sextupole magnets, Fig. 24 shows the beam line. Thirty-four of the 43 quadrupole magnets are newly manufactured at IHEP and named as QEA magnets [104]. All the quadrupole magnets that belong to the ATF2 FFS except the FD are denoted as QEA magnets. A first measurement campaign of the ATF2 FFS magnets was conducted at IHEP in 2006 during the manufacturing stage using the harmonic coil measurement technique [105]. The rotating coil measurement provides the integrated strength and the tilt of each multipole component present in the magnet. The strength of each multipole component is introduced into the model by fixing its ratio relative to the strength of the magnet, so that a variation of the magnet strength modifies the strength of its multipole components proportionally. It is assumed here that the strength of the multipole component varies linearly with the magnet strength. Each multipole component is modelled by thin elements at the edges and at the centre of the magnets. The sum of the thin element strengths being equal to the measured integrated strength.

The evaluated beam sizes at the IP with all the IHEP measured multipole components included in the simulations are 80 nm and 100 nm for the ATF2 Nominal and Ultra-low β^* lattices, respectively. The ATF2 lattices are described in Section 3.2.1. Taking advantage of the order-by-order analysis capabilities of MAPCLASS, discussed in Section 2.2, σ_y^* from $N_{\text{order}}= 1$ to $N_{\text{order}}= 10$ is evaluated. The maximum order is fixed by the maximum multipole component measurement included into the model.

[**] In the following analysis, σ_y^* always refers to the rms definition calculated by MAPCLASS according to Eq. (45). The spot sizes according to Shintake and Core definitions are denoted as σ_{shi}^* and σ_{core}^*, respectively.

Figure 36 shows the IP vertical beam size for those orders that increase σ_y^* significantly. From the order-by-order analysis one can see that the second, third and fifth orders are the main contributors to the observed vertical beam size growth. They correspond to the sextupole, octupole and dodecapole components, respectively. This unexpected increase of σ_y^* led to a revision of the multipole component measurements that were introduced into the model. In 2007 a second measurement campaign of the QEA magnets was conducted at KEK, the results are reported in [106]. Significant discrepancies between the IHEP and KEK measurements for some magnets were found, as it can be seen from Fig. 37. Several magnets do not meet the specifications defined in [77], according to which the amount of relative sextupole component tolerance is $4{\cdot}10^{-4}$ at 1 cm radius from the magnetic center of the magnet. Due to the uncertainty of the amount of relative sextupole component in the magnets it was decided to study the correction of σ_y^* provided by tilting the ATF2 sextupole magnets.

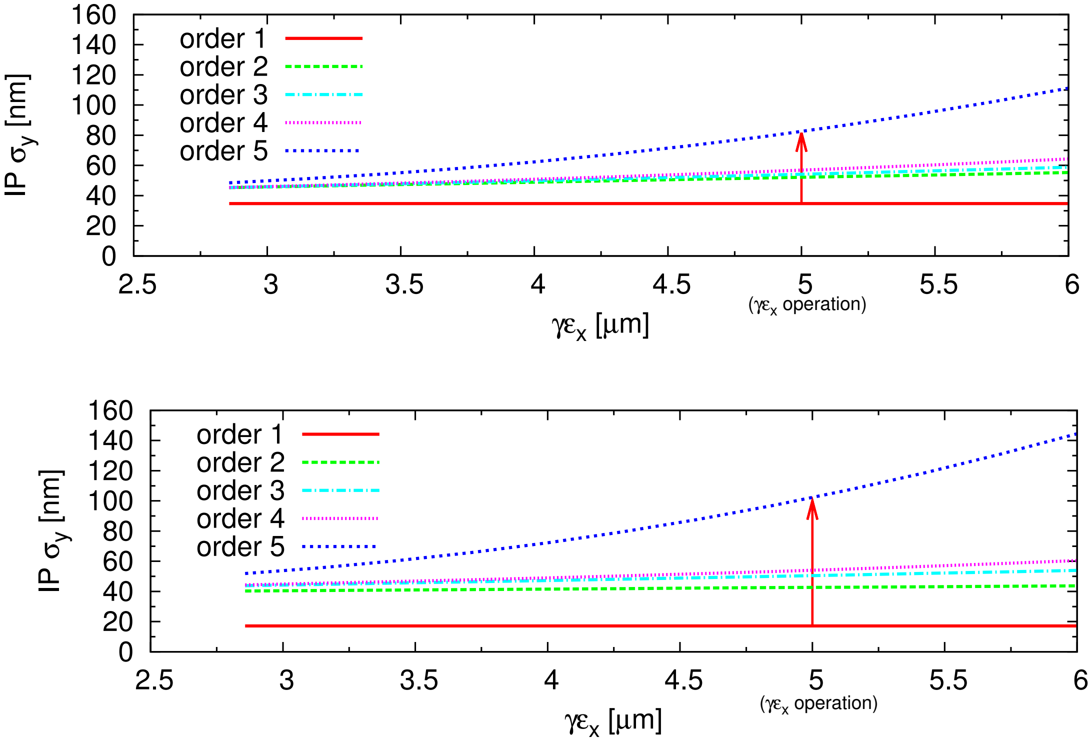

Figure 36: σ_y^* obtained in the simulations as a function of $\gamma\epsilon_x$ with the initial multipole components measurements included into the model. The red arrow points to the typical value of the normalised horizontal emittance during ATF operation. Each curve represents σ_y^* for a given order 1, 2, 3, 4 or 5 which corresponds to the transfer map with N_{order}=1, 2, 3, 4 and 5 respectively. The upper plot refers to the ATF2 Nominal lattice whereas the lower plot refers to the ATF2 Ultra-low β^* lattice.

4.2.1.1 Correction by tilting the sextupole magnets

Figure 37 shows the discrepancy between the IHEP and KEK field quality measurements of the magnets. Due to this uncertainty, it was decided to study the impact of different values of strength and tilt for the sextupole component of the QEA magnets within the range of the observed discrepancies between the IHEP and KEK measurements. In this sense, the strength and tilt of the sextupole

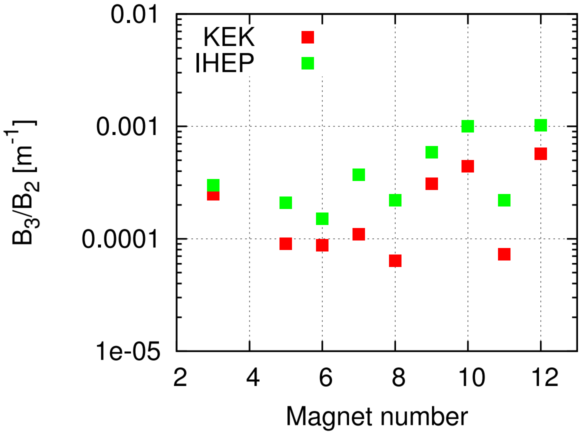

Figure 37: Comparison between KEK (red dots) and IHEP (green dots) measurements of the relative sextupole component at a radius of 1 cm of those QEA magnets which are close or above the tolerance of 10^{-4} (Data courtesy of G. White).

Magnet		SF6FF	SF5FF	SD4FF	SF1FF	SD0FF
k_s	[m^{-2}]	8.56	-0.79	14.91	-2.58	4.31
$\beta_{x,\mathrm{sext}}$	[m]	1864	1864	300	5553	2019
$\beta_{y,\mathrm{sext}}$	[m]	1906	1906	8469	2638	9942
Tilt	[mrad]	9.5	20.0	-7.6	-4.0	2.8
σ_y^*	[nm]	74	58	76	94	96

Table 11: Comparison between the strength, the value of the β-functions at the centre of the sextupole, the tilt and the obtained values of the IP beam size when tilting the ATF2 sextupoles individually.

components of the QEA magnets are randomly varied, for each scenario the sextupole magnets are tilted in order to minimise σ_y^*. The study refers to the ATF2 Nominal lattice including only the sextupole components. The approach consists of increasing by 50% the sextupole components of the QEA magnets, which increases the IP vertical spot size up to 140 nm. Figure 38 shows 5 curves that represent the correction provided by each sextupole magnet. The green curve of Fig. 38 corresponds to the SF5FF sextupole magnet which provides the wider and largest σ_y^* compensation, obtaining a final $\sigma_y^* < 60$ nm. It is also worth noticing that a small correction of σ_y^* is provided by the final doublet sextupole magnets (SF1FF and SD0FF). The SF5FF magnet operates at very low current as shown in Table 11, this allows a large tilt to compensate the skew sextupole components present in the quadrupole magnets.

The study was repeated for scale factors of 100% and 150%, for each factor 100 different machines are simulated each machine having the sextupole components of the QEA magnets randomly increased. Only the SF6FF, SF5FF and SD4FF sextupole magnets are considered. Figure 39 shows the results for the studied cases. Again, SF5FF provides the largest correction to σ_y^*. Red, green and blue curves show the results for the SF6FF, SF5FF and SD4FF sextupole magnets, respectively.

4.2.1.2 Correction by means of a dedicated skew sextupole magnet

The correction on the IP beam size provided by tilting the sextupole magnets is not a preferred solution

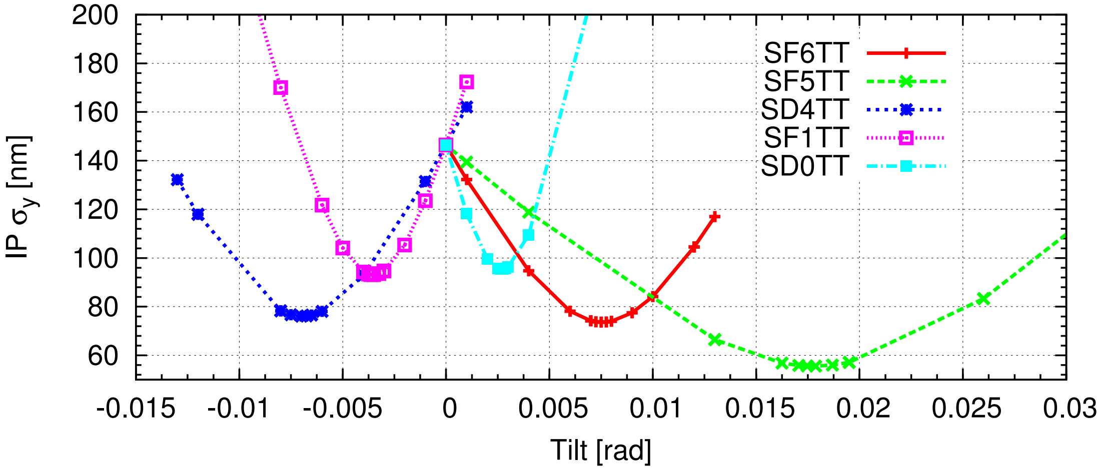

Figure 38: σ_y^* (2$^{\text{nd}}$ order) as a function of the sextupole tilt for the ATF2 Nominal lattice. Red, green, blue, magenta and cyan colours represent the tilt of the SF6FF, SF5FF, SD4FF, SF1FF and SD0FF sextupole magnets respectively.

since its correction range is rather small as shown in Fig. 38. In addition the coupling introduced by a tilted sextupole may impact the orthogonality of the tuning knobs as explained in Section 2.4.1.3. An alternative way to compensate the skew sextupole component of the magnets rather than tilting the normal sextupole magnets is by using a dedicated skew sextupole magnet [107]. Such a magnet provides the same correction in terms of σ_y^*. Taking into account the space constraints in the ATF2 FFS, the place chosen to insert the skew sextupole magnet (SK1) was in between the quadrupoles QD6FF and QF5BFF, close to the sextupole magnet SF5FF. In order to reduce the required current in the skew sextupole magnet, it is located close to magnet QF5BFF where the dispersion is 3 times larger than in the vicinity of QD6FF. The σ_y^* obtained in this approach is equivalent to the one obtained by tilting the sextupole magnet.

In January 2011 the dedicated skew sextupole magnet was installed at the ATF2 beam line. Figure 40 shows the installed skew sextupole magnet.

In the following calculations, the skew sextupole is included into the model and is considered in the sextupole optimisation.

4.2.1.3 Ultimate multipole components

Detailed analysis of the field quality measurements at IHEP and KEK [101] revealed a wrong interpretation of the tilt definition used for the IHEP measurements[††]. With the correct interpretation of the tilt, the observed differences disappear except for a few magnets, as can be observed in Fig. 42. The QD10BFF, QD6FF, QF7FF, QF5AFF, QF5BFF, QD4AFF, QF3FF, QD2AFF, QD4BFF and QD2BFF magnets still show discrepancies concerning the sextupole and the octupole components, a swap in the pick-up coil connection may be a possible explanation, as suggested in Ref. [101]. In the following calculations the data of the KEK multipole measurements available at [108] is considered in the ATF2 model.

[††] The cross-check between the IHEP and KEK field quality measurements was done by the ATF2 collaborators M. Masuzawa and M. Woodley

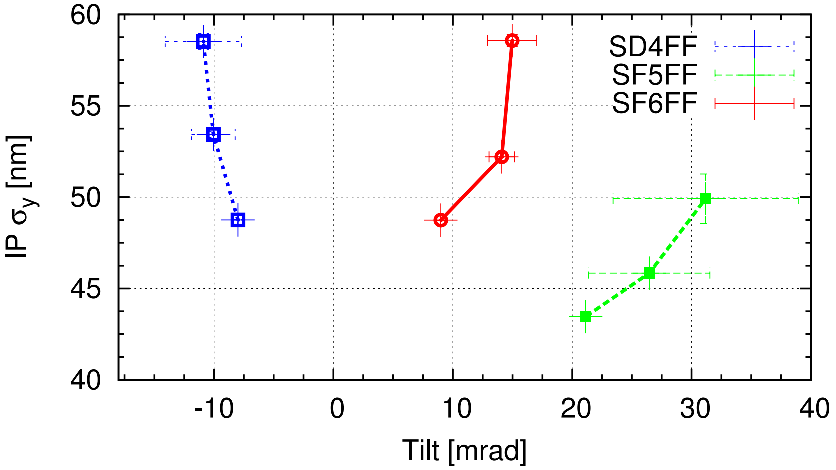

Figure 39: Average σ_y^* (2^{nd} order) as a function of the sextupole tilt for the ATF2 Nominal lattice. Each point is the average of 100 machines for which the multipole components have been randomly increased by 50%, 100% and 150%. The error bars are obtained as the quadratic standard deviation of the 100 simulated machines.

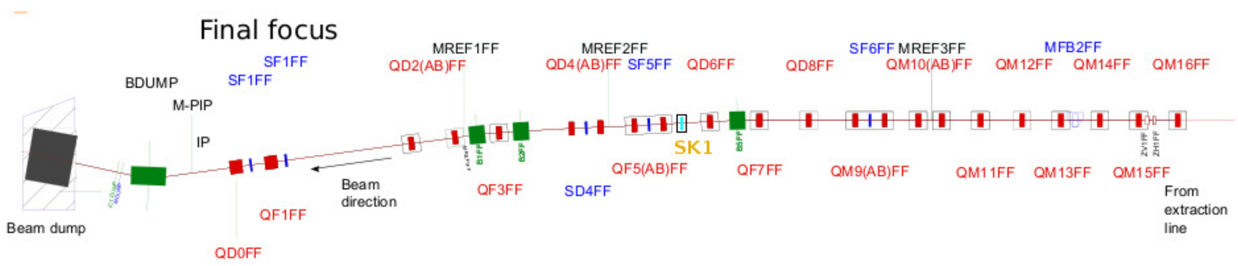

Figure 40: Scheme of the ATF2 FFS. The skew sextupole magnet SK1 (orange) is in between QF5BFF and QD6FF quadrupole magnets (Figure courtesy of S. Boogert).

4.2.2 Impact of the ultimate multipole components of the ATF2 magnets

With all the KEK multipole components included into the model the beam size at the IP is found to be larger than expected for both the ATF2 Nominal and Ultra-low β^* lattices. Depending on the beam size definition, this increase ranges from a few to hundreds of percent. As it is explained in Section 2.1.2 three different beam size definitions, namely core, Shintake and rms, have been considered in this study. Table 12 summarises the evaluated spot sizes at the IP when gradually including the measured multipole components. Four different scenarios have been studied according to the multipole component measurements included into the ATF2 model:

- without multipole components,
- only the QEA multipole components,
- only the FD multipole components,
- all the multipole components.

Figure 41: Picture of the installed skew sextupole magnet (SK1) between the QF5BFF (left) and QD6FF (right) quadrupole magnets (red) (Picture courtesy of N. Terunuma).

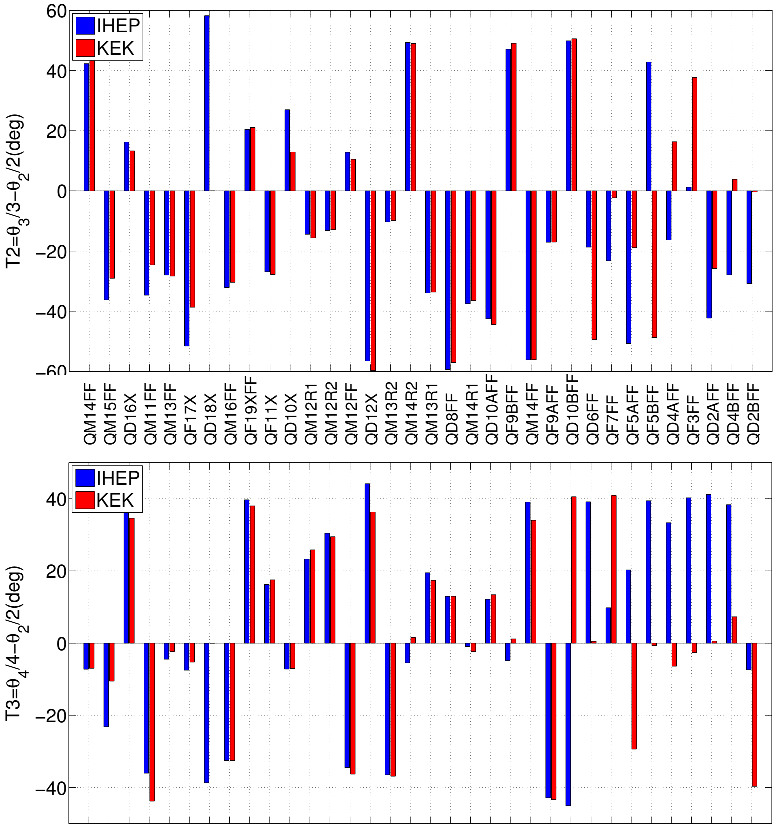

Figure 42: Comparison between the IHEP (blue) and KEK (red) measurements of the multipole components. T2 refers to the sextupole component angle and T3 refers to the octupole component angle (Figure by courtesy of S. Bai).

ATF2 Nominal Lattice				
	σ_x^* [μm]	σ_y^* [nm]		
	RMS	CORE	SHINTAKE	RMS
No mults	3.0	37.2	37.3	38.0
All QEA mults	3.5 (+17%)	37.3 (+0.3%)	38.8 (+4%)	43.2 (+14%)
Only FD mults	3.9 (+30%)	39.3 (+5.6%)	41.8 (+12%)	66.9 (+76%)
All mults	3.9 (+30%)	39.3 (+5.6%)	41.8 (+12%)	66.9 (+76%)
ATF2 Ultra-low β^* lattice				
No mults	3.0	20.4	22.8	23.1
All QEA mults	3.4 (+13%)	23.6 (+16%)	28.9 (+27%)	43.5 (+88%)
Only FD mults	3.7 (+23%)	30.0 (+47%)	42.3 (+86%)	80.1 (+247%)
All mults	3.7 (+23%)	30.0 (+47%)	42.3 (+86%)	80.1 (+247%)

Table 12: Comparison between the values of the IP beam size obtained according to 3 different definitions for the ATF2 Nominal and Ultra-low β^* lattices with and without multipole components. The value shown inside the parenthesis refers to the percentage of beam size growth with respect to the beam size for the case where no multipoles are included. The RMS value is obtained by MAPCLASS with a value of $N_{\mathrm{order}}=5$.

The effect of the multipole components turns out to be well above the expectations. For the ATF2 Ultra-low β^* lattice the situation is much worse than for the ATF2 Nominal lattice. The comparison between the $\Delta\sigma_y^*/\sigma_{y_0}^*$ of the different beam size definitions suggests that the tails of the bunch are enhanced by the multipole components. From Table 12 it is inferred that the most important sources of the evaluated beam size increase are the multipole errors of the Final Doublet quadrupoles. As it is mentioned in Section 3.2.1 the IP beam size is extremely sensitive to the field quality of the FD. Figure 43 shows the results of the MAPCLASS analysis for the ATF2 Ultra-low β^* lattice. It can be seen that the sextupole (2$^{\mathrm{nd}}$ order) and the dodecapole (5$^{\mathrm{th}}$ order) components are the main sources of the observed vertical beam size increase. The 2$^{\mathrm{nd}}$ order curve (green) in Fig. 43 shows no dependence of σ_y^* on $\gamma\epsilon_x$, thus the normal sextupole component is responsible for the observed vertical beam size increase. Therefore the skew sextupole components have almost no relevance any more. The dependence of σ_y^* on $\gamma\epsilon_x$ at the 5$^{\mathrm{th}}$ order implies that a skew dodecapole component is an important source of the observed σ_y^* increase.

4.2.3 Final Doublet Tolerances

The final doublet is the major source of vertical beam size increase at the IP, as it can be seen from Table 12. The tolerances for the ATF2 Ultra-low β^* lattice are evaluated by MAPCLASS in order to be compared with the tolerances for the ATF2 Nominal lattice given in [77]. Since more restrictive tolerances are expected for the Ultra-low β^* lattice than for the Nominal lattice, replacing the present FD by a better field quality FD that satisfies the ATF2 Ultra-low β^* tolerances may represent a step forward for the ATF2 facility.

The tolerances for the sextupole, octupole, decapole and dodecapole components of QF1FF and QD0FF are determined assuming an error-free ATF2 Ultra-low β^* lattice. The method for the evaluation was the following: the value of the normal and skew multipole component is increased until σ_y^* increases by 2%. Figure 44 shows the behaviour of the relative skew sextupole component of QF1FF as an example, according to two different beam size definitions, rms and Shintake. The columns

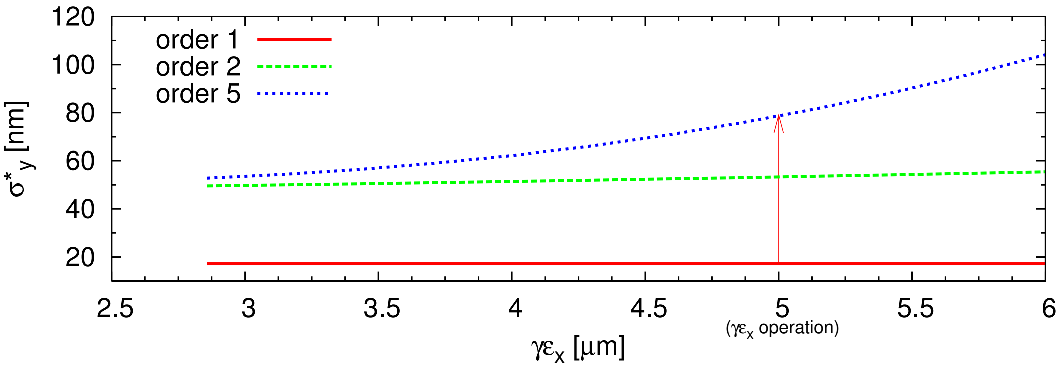

Figure 43: Plot of σ_y^* as a function of $\gamma\epsilon_x$ for the ATF2 Ultra-low β^* lattice including the ultimate multipole components. The red curve represents the vertical IP beam size considering up to the quadrupole components, green curve includes the sextupole components and the red curve takes into account all the measured multipole components.

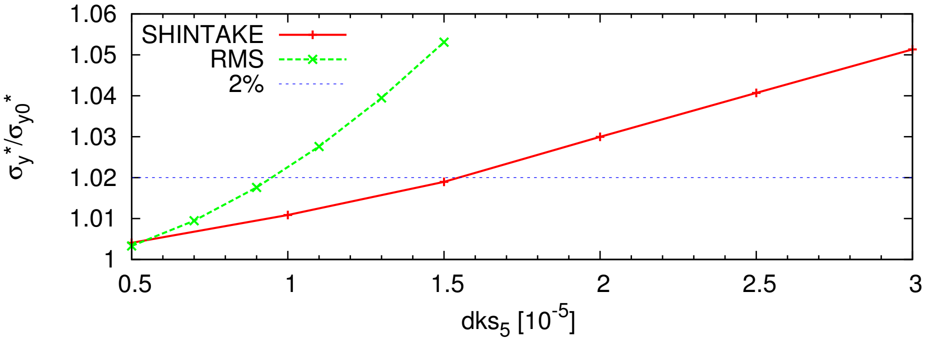

Figure 44: Plot of σ_y^* as a function of the relative skew dodecapole component (dks$_5$) of QF1FF at a radius equal to 1 cm for the ATF2 Ultra-low β^* lattice. Each curve represents σ_y^*/σ_{y0}^* according to the rms (red) and Shintake (green) beam size definition.

labelled as Tol.NL and Tol.UL of Table 13 summarise the obtained tolerances for QD0FF and QF1FF magnets for the ATF2 Nominal and Ultra-low β^* lattices, respectively. It is observed that tighter skew tolerances for all multipole components are obtained for QF1FF due to the higher β_x value at QF1FF. Table 13 compares the evaluated tolerances of QF1FF and QD0FF for the ATF2 Ultra-low β^* lattice with the measured multipole components. The cases for which the magnetic measurement exceeds the tolerance are marked in red. Table 13 shows that QF1FF exceeds the tolerances in almost all normal and skew multipole components, whereas for QD0FF only the sextupole component exceeds the tolerance. From the analysis of Fig. 43 and the comparison made in Table 13 it can be concluded that in order to achieve the design IP spot size for both ATF2 lattices a new design of the FD should be implemented, as considered in [109].

To this end, two projects to develop a new FD for ATF2 at BNL and CERN are on-going. At BNL, a superconducting quadrupole prototype has been constructed [110]. The superconducting magnet is a multilayer structure, hence after each coil winding, the multipole components are measured. If any measured component is above the expected tolerance the following winding is adjusted in order to compensate it. The final multipole component measurements are summarised in Table 14.

At CERN it has been proposed to design and construct a new quadrupole [111] based on permanent

Component	Sextupole $[10^{-4}]$					
	Normal			Skew		
	Tol.UL	Measured	Tol.NL	Tol.UL	Measured	Tol.NL
QF1FF	0.37	2.7	1.2	0.07	0.28	0.09
QD0FF	0.2	1.84	0.8	0.18	1.76	0.3

Component	Octupole $[10^{-4}]$					
	Normal			Skew		
	Tol.UL	Measured	Tol.NL	Tol.UL	Measured	Tol.NL
QF1FF	0.15	0.57	0.7	0.07	0.04	0.1
QD0FF	1.8	0.44	6.0	0.8	0.28	1.2

Component	Decapole $[10^{-4}]$					
	Normal			Skew		
	Tol.UL	Measured	Tol.NL	Tol.UL	Measured	Tol.NL
QF1FF	0.43	1.2	0.9	0.08	0.19	0.11
QD0FF	3.15	0.65	10.1	2.9	0.32	4.3

Component	Dodecapole $[10^{-4}]$					
	Normal			Skew		
	Tol.UL	Measured	Tol.NL	Tol.UL	Measured	Tol.NL
QF1FF	0.17	3.4	0.4	0.09	0.76	0.11
QD0FF	15.0	3.5	50.0	9.0	0.22	12.3

Table 13: Comparison between the relative tolerances evaluated at a radius equal to 0.01 m for the ATF2 Nominal and Ultra-low β^* lattices and the measured multipole components of QF1FF and QD0FF. The cases for which the measured multipole component does not meet the evaluated tolerances for both ATF2 lattices are marked in red, when the measurements only meet the tolerance for the ATF2 Nominal lattice orange is used and when the measurements satisfy both ATF2 Nominal and Ultra-low β^* tolerances green.

Final Doublet	Sextupole $[10^{-4}]$		Octupole $[10^{-4}]$		Decapole $[10^{-4}]$		Dodecapole $[10^{-4}]$	
	Normal	Skew	Normal	Skew	Normal	Skew	Normal	Skew
UL Tolerance	0.2	0.07	0.15	0.07	0.43	0.08	0.17	0.09
Normal conducting	1.84	0.28	0.44	0.04	0.65	0.19	3.4	0.22
Superconducting	0.49	-0.49	-0.2	-0.35	0.025	-0.016	0.000	0.001
Permanent	0.4	0.05	0.65	0.07	0.4	0.06	0.5	0.08

Table 14: Comparison between the tightest relative tolerance at a radius equal to 0.01 m of the FD for the ATF2 Ultra-low β^* lattice and the measured multipole components of the superconducting magnet (SC) [112] and the expected components of the permanent magnet (PM) [111]. (The SC and PM data are provided by B. Parker and A. Vorozhtsov respectively.). The smallest measured multipole components of the current QF1 and QD0 are shown as an example of normal conducting component.

magnet (PM) material. The expected multipole components from previous prototypes are summarised in Table 14. The new FD designs based on superconducting and permanent magnet technology almost satisfy the evaluated tolerances for the ATF2 Ultra-low β^* lattice, yet the sextupole component tolerance is not satisfied by none of them, reflecting the difficulty for minimising the IP beam aberrations for the pushed optics proposal.

When replacing the MAD-X model of the current normal conducting final doublet of ATF2 by the super-conducting or permanent magnet ones, a significant reduction of $\Delta\sigma_y^*$ is obtained with respect to the σ_y^* with normal conducting magnets. Yet the evaluated σ_y^* for the ATF2 Nominal lattice is about 50 nm when considering the SC or the PM final doublet. Whereas for the ATF2 Ultra-low β^* lattice it is obtained a σ_y^*= 48 nm, as Fig. 45 shows.

Despite this $\Delta\sigma_y^*$ reduction as a result of the new FD design, the impact of the remaining multipole components of the ATF2 magnets on the IP beam sizes is still noticeable for the ATF2 lattices. The designed σ_y^* in absence of multipole components given in Table 12 are 38 nm and 23 nm for the ATF2 Nominal and Ultra-low β^* lattices respectively. From the order-by-order analysis of the ATF2 Ultra-low β^* with a PM final doublet, it is inferred that the sextupole and octupole components are the most relevant sources of vertical beam size increase, see Fig. 45.

Therefore the multipole components present in the remaining quadrupoles (QEA) are partially responsible for the IP beam size increase. Sorting these quadrupoles according to their field quality is a possible solution to further reduce $\Delta\sigma_y^*$, as proposed in [113].

4.2.4 Swapping proposals for the QEA magnets

Sorting the quadrupoles according to their field quality and placing the best magnets in the more sensitive locations might help to minimise the impact of multipole components present in the ATF2 beam line. This is the idea of the approach to reduce $\Delta\sigma_y^*$ in this section.

A sensitivity study for all the quadrupole magnets that belong to ATF2 FFS has been performed in order to discern the most sensitive locations. Using an ideal (error-free) ATF2 Nominal lattice, the skew sextupole component at each location is increased until σ_y^* increases by 2% and a similar study is performed for the skew octupole component. The blue curve of Figs. 46 and 47 shows the amount of relative skew sextupole and octupole components respectively producing a 2% growth of σ_y^* at each location. Locations are sorted according to their sensitivity. Only the most important 11 locations are

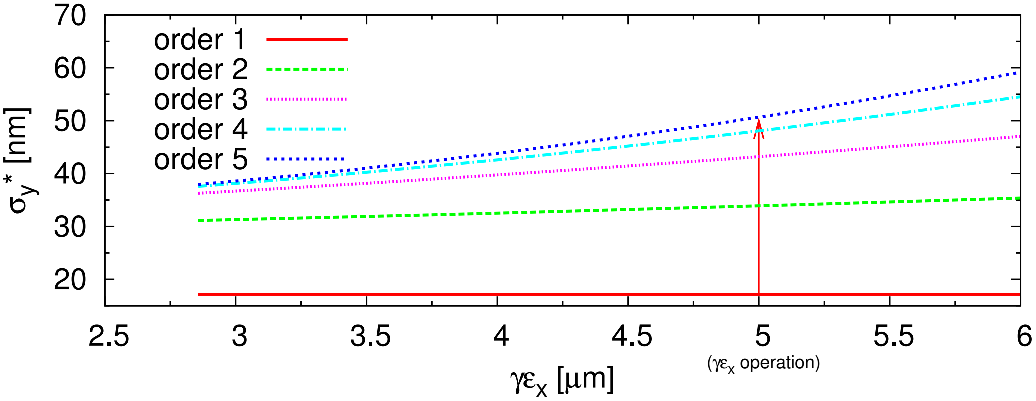

Figure 45: σ_y^* evaluated by MAPCLASS as a function of $\gamma\epsilon_x$ for the ATF2 Ultra-low β^* considering the expected PM tolerances for the FD and the measured multipole components of the remaining magnets.

shown, for the rest of them the calculated tolerances are satisfied by the present quadrupole magnets.

In order to sort the best quadrupoles in terms of their field quality, all the quadrupole magnets, except the FD, have been sorted out according to their relative skew sextupole component. The upper and lower plots of Fig. 48 show the best 9 QEA quadrupole magnets according to the skew sextupole and octupole components, respectively.

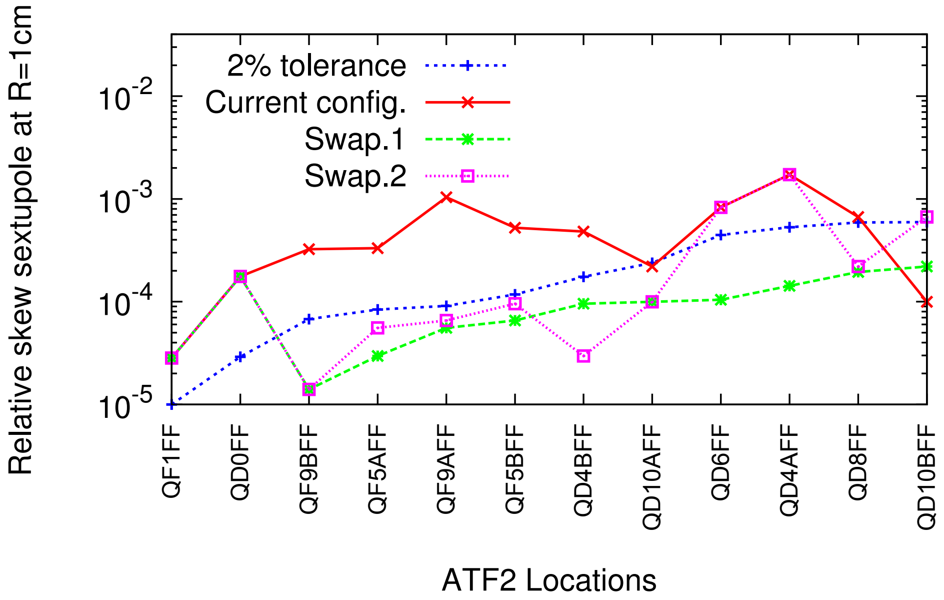

Figure 46: Relative amount of skew sextupole component that increases σ_y^* by 2%. The horizontal axis shows the beam line location denoted by the name of the corresponding quadrupole name.

Using the data shown in Figs. 46 and 47, two possible quadrupole orderings are proposed:

- *Swap.1*: quadrupole magnets are sorted according to their skew sextupole component. The proposed swapping of the magnets is the following:

QF9BFF replaced by QM12FF

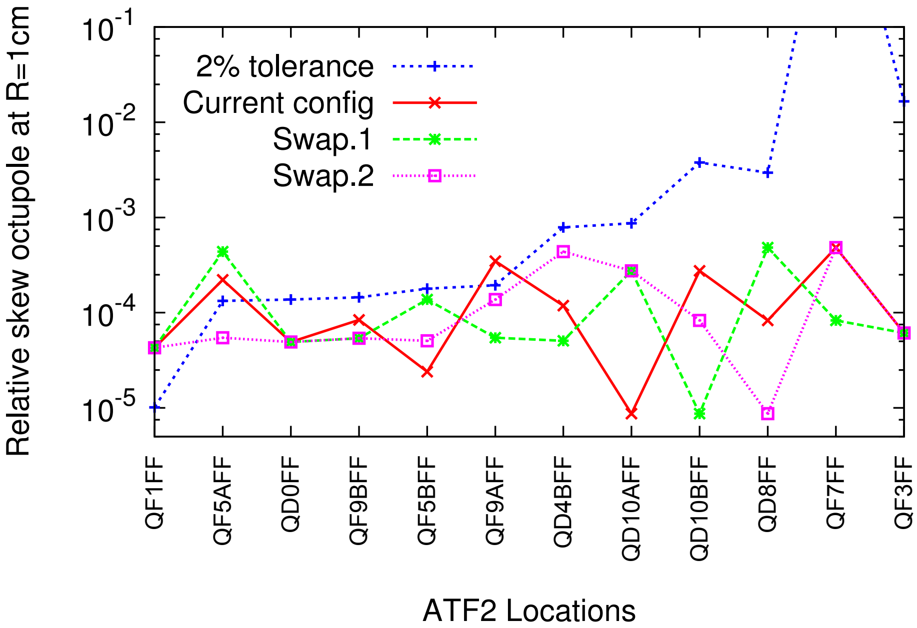

Figure 47: Relative amount of the skew octupole component that increases σ_y^* by 2%. The horizontal axis shows the beam line location denoted by the name of the corresponding quadrupole name.

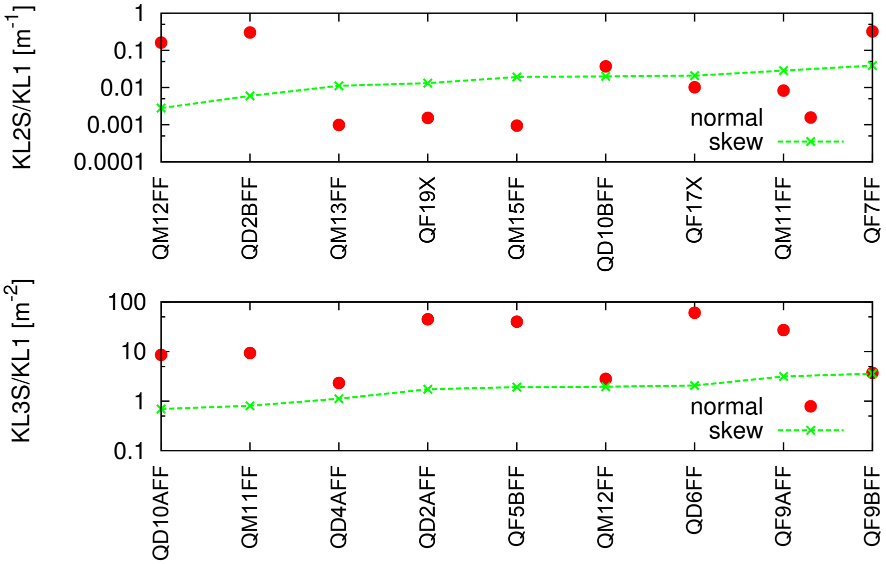

Figure 48: Lower plot: Best 9 QEA quadrupole magnets according to their skew octupole component. Upper plot: Best 9 QEA quadrupole magnets according to their skew sextupole component.

QF5AFF replaced by QD2BFF
QF9AFF replaced by QM13FF
QF5BFF replaced by QF19XFF
QD4BFF replaced by QM15FF
QD10AFF replaced by QD10BFF
QD6FF replaced by QF17X
QD4AFF replaced by QM11FF
QD8FF replaced by QF7FF

- *Swap.2*: quadrupole magnets are sorted according to their skew octupole component, in case two magnets satisfy the octupole tolerance they are sorted in order to satisfy the sextupole tolerance as well. The proposed swapping of the magnets is the following:

QF5AFF replaced by QF17X
QF9BFF replaced by QM12FF
QF5BFF replaced by QM15FF
QF9AFF replaced by QM13FF
QD4BFF replaced by QF11X
QD10AFF replaced by QM16FF
QD10BFF replaced by QM11FF
QD8FF replaced by QD16X
QD6FF replaced by QM14FF

The data shown in Fig. 48 is translated into the relative components at R=0.01 m in order to compare it with the calculated tolerances. The comparison is made in Figs. 46 and 47. The red curve represents the current skew sextupole component. The green and magenta curves show the expected skew sextupole component after swapping the magnets according to the swap.1, and swap.2 criteria respectively. It was assumed that the multipole components remain proportional to the quadrupole strength.

From the data shown in Fig. 46 it was concluded that the present skew sextupole component exceeds the 2% tolerance in almost all evaluated locations. According to the swap.1 sorting all the skew sextupole components are below tolerances and according to the swap.2 sorting only the first 6 high sensitivity locations satisfy the tolerances.

As far as the skew octupole components are concerned, in general the situation is much better. The current configuration and the swap.1 sorting satisfy the octupole tolerances at all locations except 2. When considering the swap.2 sorting, all octupole tolerances are satisfied. Figure 47 shows the octupole tolerance and the amount of skew octupole component for the current configuration, the swap.1 and swap.2 sorting.

The calculated σ_y^* for the ATF2 Nominal lattice with a PM final doublet according to the swap.1 and swap.2 options are 41 nm and 44 nm respectively. Regarding the ATF2 Ultra-low β^* lattice with a PM final doublet the calculated vertical beam size at the IP is 38 nm and 41 nm for swap.1 and swap.2 options respectively.

Therefore, the obtained σ_y^* according to the swap.1 sorting is better than the one according to the swap.2 sorting for the ATF2 lattices. It is also concluded that σ_y^* is very sensitive to the sextupole component of the quadrupole magnets. Therefore, the swap 1 distribution of the quadrupole magnets is recommended to avoid the demonstrated detrimental effects of the measured multipole components.

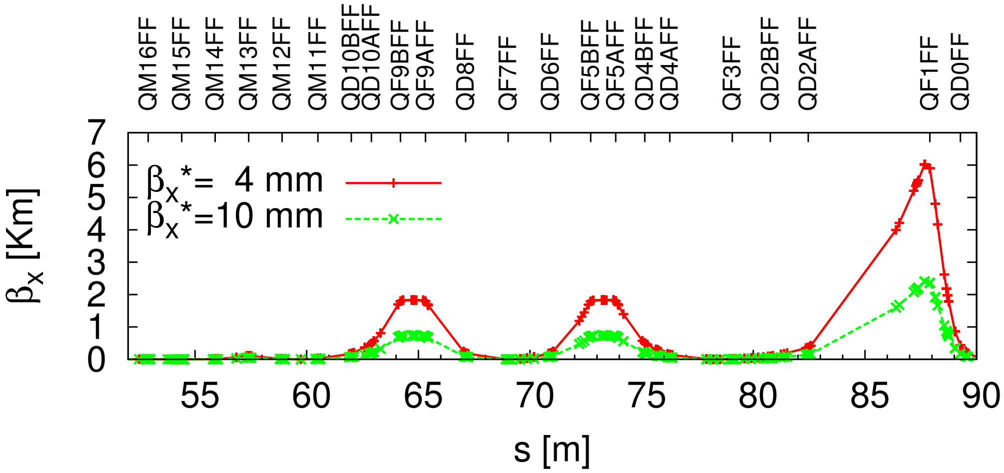

Figure 49: Red and green curves represent the β_x function for the ATF2 Nominal lattice with β_x^* equal to 4 and 10 mm respectively, along the ATF2 FFS.

4.2.5 Optics modification

One more approach to minimise the detrimental impact of the multipole components is to modify the optics by increasing β_x^*. Doing so, the horizontal beta function is lowered along the FFS according to Eq. (15). Thus the impact of all the multipole components present in the ATF2 magnets is reduced as well. Although, increasing β_x^* is not the preferred solution, since it is not foreseen in the final focus system design of the future linear colliders, considering ILC as an example, increasing 2.5 times β_x^* enlarges σ_x^* by a factor $\sqrt{2.5}$ according to Eq. (12) which reduces $\mathcal{L}$ by almost 40% according to Eq. (6). Nevertheless this solution is considered in this study, because it may help to reduce the detrimental effect of the multipole components enabling to test the local chromaticity correction scheme of FFS. By using the matching quadrupoles QM16FF, QM15FF, QM14FF, QM13FF and QM12FF located at the beginning of the final focus, β_x^* is increased from 4 mm to 10 mm. Afterwards the remaining quadrupoles and sextupoles are optimised in order to compensate for the beam aberrations and reach the design spot size at the IP. This optimisation process is done by the simplex algorithm [63] inserted in MAD-X in combination with MAPCLASS code which evaluates σ^*.

Figure 49 shows the horizontal beta function along the FFS of ATF2 for the ATF2 Nominal lattice with β_x^*=4 and β_x^*=10 mm. The horizontal beta function at QF1FF with β_x^*=10 mm is 2.5 times smaller according to Eq. (15). The obtained σ_y^* when increasing β_x^* to 10 mm is equal to 41 nm for the ATF2 Nominal lattice. The performance of this new lattice was cross-checked by the ATF2 collaborators G. White and M. Woodley, using the Lucretia code [114] and MAD-8 [115] respectively, obtaining similar values of σ_y^* [116]. Indeed the impact of the FD is effectively minimised and so are the multipole components present in the QEA quadrupole magnets. This new design is called ATF2 Bx2.5By1.0 lattice, since β_x^* is 2.5 times larger than the nominal β_x^*, and it was used in ATF2 for the experimental tuning attempt in December 2010. Details of the simulated and experimental tuning performance of this lattice can be found in Section 5.2.1. The MAD-X model of the new ATF2 Bx2.5By1.0 lattice can be found in [102].

For the ATF2 Ultra-low β^* with β_x^*= 10 mm, the obtained vertical spot size at the IP is 51 nm, well above the design value of 23 nm. Therefore in contrast to the ATF2 Nominal lattice the mitigation obtained by increasing β_x^* is not enough for the Ultra-low β^* lattice. The endpoints of the green curve of Fig. 50 show the results for the ATF2 Nominal and Ultra-low β^* lattices. The study of two intermediate lattices with β_y^* equal to 50 μm and 75 μm helps to understand the impact of the multipole components when going to ultra-low values of β_y^*. For smaller values the beam aberrations dominate the σ_y^* as shown by the red curve in the present ATF2. Regarding the swap.1 and swap.2 sorting, when increasing β_x^* to 10 mm the impact of the beam aberrations is not as severe as in the current quadrupole configuration. For the swap.1 and swap.2 sorting, the obtained σ_y^* are 31 nm and 35 nm respectively, as shown by the green and blue curves of Fig. 50. The measured multipole components preclude from reaching the expected vertical beam size for the ATF2 Ultra-low β^* lattice just by increasing β_x^*. Although going to a larger value of β_y^* is not a preferred cure because in doing so the vertical chromaticity decreases, and becomes no longer comparable to the vertical chromaticity of CLIC, as shown in Table 8.

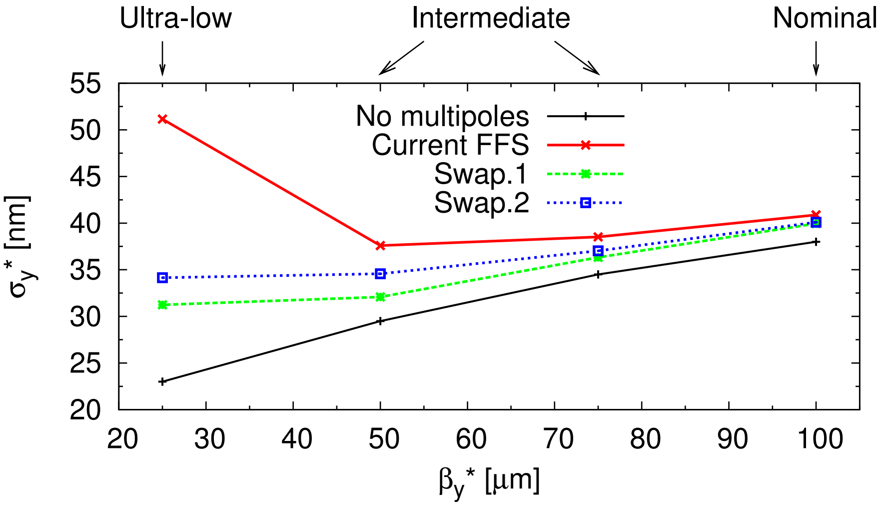

Figure 50: Calculated beam size σ_y^* for different values of β_y^* (25, 50, 75, 100 μm) with β_x^*=10 mm. Each curve refers to a different magnet sorting. The red curve corresponds to the current configuration. The blue and magenta curves correspond to the sorting options swap.1 and swap.2 respectively. The black curve represents σ_y^* without multipole components.

4.2.6 ATF2 Ultra-low β_y^* lattice

The effect of the multipole components on the IP beam size cannot be mitigated for the ATF2 Ultra-low β^* lattice when applying the studied solutions separately. However by combining all the studied solutions a further reduction of $\Delta\sigma_y^*$ is achieved. Two solutions are considered. In the **1$^{\text{st}}$ solution** the value of β_x^* is increased up to 10 mm, in addition the QEA magnets are sorted according to swap.1 proposal. This gives the results σ_y^*=31 nm and σ_{Shi}^*=29.1±0.3 nm. In the **2$^{\text{nd}}$ solution** it is required to replace the final doublet by the permanent quadrupole magnets developed at CERN, the remaining ATF2 quadrupole magnets need to be sorted according to the swap.1 proposal and the β_x^* has to be increased up to 6 mm for further mitigation of the effect of the measured components. The obtained values of vertical IP spot size are 27 nm and 25.6±0.2 nm according to the rms and Shintake beam size definitions. Since β_x^* is no longer the nominal value of 4 mm, this lattice is called ATF2 Ultra-low β_y^* lattice. The model of the new lattice design can be found at [103]. Table 15 summarizes the calculated beam sizes when gradually adding the solutions presented in Section 4.2.2.

The adopted solutions presented in Table 15 are partially satisfactory. On one hand the vertical chromaticity of the lattice is comparable to the CLIC 3 TeV but on the other hand the value of β_x^*

Table 15: Calculated σ_x^* and σ_y^* according to the core, Shintake and rms beam size definitions. The rms and $\sigma_{\rm Shi}^*$ values are obtained by MAPCLASS with $N_{\rm order}$=5 and by the Shintake algorithm respectively.

	σ_x^* [μm]	σ_y^* [nm]		
	RMS	CORE	SHINTAKE	RMS
ATF2 UL β^*	4.4	35±0.4	42.5±0.5	80
1st solution				
β_x^*= 10 mm	4.5	30.2±0.4	40.4±0.4	51
+ swap.1	4.5	24.7±0.5	29.1±0.3	31
2nd solution				
+ PM FD	3.5	26.8±0.5	35.4 ±0.4	48
+ swap.1	3.6	21.7±0.3	26.8±0.3	32
+ β_x^*= 6 mm	3.6	21.2±0.3	25.6±0.2	27

needs to be increased. A smaller σ_y^* is obtained for the 2nd solution due to better field quality of the FD magnets. Despite the increase of the cost due to the fabrication of the magnets, it would be the preferred solution because it would also allow to test the ATF2 Nominal lattice with the nominal value of β_x^*.

5 Final Focus Systems tuning results

The tuning of a final focus system consists of bringing the system to its design performance under realistic error conditions as defined in Section 2.4. It is of special importance since it determines the feasibility of a lattice.

Three tuning algorithms namely, (i) *Simplex*, (ii) *Beam Based Alignment* and (iii) *orthogonal knobs* for tuning the CLIC and ATF2 final focus systems are considered.

In this section simulation results of the tuning of the CLIC BDS with $L^*= 6$ m by means of a tuning procedure that combines a beam based alignment and orthogonal knobs algorithms are shown. The results are compared to those reported in Ref. [31] in which the Simplex tuning algorithm for the same lattice was used. In previous studies, the same tuning procedure was considered for tuning the CLIC BDS with $L^*= 3.5$ m [117]. Comparison of the tuning results obtained with the same tuning algorithm for both CLIC designs allows to analyse the tuning difficulties when increasing L^*.

Also results of tuning simulations of the ATF2Bx2.5By1.0 and ATF2 Ultra-low β_y^* lattices designed in this thesis are discussed. Experimental tuning results obtained during the tuning session carried out in December 2010 using the new ATF2Bx2.5By1.0 design are compared to the simulation results. No comparison with experimental results for the ATF2 Ultra-low β_y^* lattice is made due to the long interruption of the ATF2 operation caused by the big earthquake that shook Japan in March 2011. Therefore there are not experimental studies of the tuning versus the β_y^*.

5.1 CLIC BDS tuning

The baseline design of the CLIC BDS and the alternative option with $L^*= 6$ m are described in Section 1.2.1.2. The CLIC BDS consists of three main subsystems: (i) the diagnostics, (ii) the collimation and (iii) the final focus system. Previous studies on tuning simulations have demonstrated the tunability of the two first sections of the BDS against misalignments, when applying the standard beam based correction techniques presented in Section 2.4 [118]. However for the FFS the number of simulated machines that reach the tuning target using this tuning algorithm is not satisfactory.

The figure of merit of the tuning procedure of the CLIC FFS is the luminosity $\mathcal{L}$. Since the effect of ground motion is not included into the simulations the target luminosity is 110% of the design luminosity $\mathcal{L}_0$ given in Section 1.2.1.2, so that 10% budget for the luminosity loss due to dynamic imperfections is allowed. According to [17] the tuning goal for the CLIC BDS is that 90% of the machines reach a final luminosity equal or higher than $1.1\mathcal{L}_0$. The results of previous tuning studies reported in Ref. [117] when applying the Simplex and the Simplex combined with orthogonal knobs tuning algorithms to the CLIC BDS baseline design are summarised in Table 16. In previous studies an alternative tuning algorithm, which combines beam based corrections and orthogonal knobs tuning algorithm techniques, is considered for tuning the CLIC BDS baseline design, the obtained results [119] are summarised in Table 16. The results given are obtained assuming that (i) the magnets of the CLIC BDS $L^*= 3.5$ m are randomly misaligned with the Gaussian distribution of width $\sigma_{\text{offset}}= 10\ \mu$m, (ii) a BPM resolution of 10 nm is assumed for the BBA tuning algorithm and (iii) the effect of synchrotron radiation described in Section 2.1.4 is included in the simulation study. 90% of the machines reach a final luminosity $\geq$90% of $\mathcal{L}_0$ when applying the (Simplex + orthogonal knobs) algorithm, while only 60% of the machines reach a luminosity $\geq$80% of $\mathcal{L}_0$ when applying the (BBA + orthogonal knob) algorithm. Regarding the number of required iterations, clearly the (BBA + orthogonal knobs) algorithm is 10 times faster than the other tuning algorithms. Each iteration corresponds to a luminosity measurement that takes half a second as reported in Ref. [117].

Tuning strategy	Iterations	Success ratio (80%$\mathcal{L}_0$)
	[10^3]	[%]
Simplex	15	80
Simplex + orthogonal knobs	16	90
BBA + orthogonal knobs	1.6	60

Table 16: Tuning results for the CLIC BDS with L* = 3.5 m using the Simplex, the Simplex with orthogonal knobs and the BBA with orthogonal knobs as tuning algorithms (Table taken from [117]).

σ_{offset}	Iterations	Success ratio
[μm]	[10^3]	80% of $\mathcal{L}_0$ [%]
5	11	91
6	10	90
7	12	87
8	11	81

Table 17: Tuning results for the CLIC BDS with L*= 6 m using the Simplex tuning algorithm. Different scenarios according to the initial random misalignments σ_{offset} of the magnets are considered. (Data taken from Ref. [31]).

5.1.1 CLIC BDS with L*= 6 m Tuning

In the CLIC BDS L*= 6 m design L* is large enough to locate the last quadrupole QD0 outside the detector, which leads to a simple solution as discussed in Section 1.2.1.2. Previous tuning studies to the CLIC BDS L*= 6 m design show promising results when applying the simplex tuning algorithm (see Ref. [31]), the results are summarised in Table 17. As one can see for σ_{offset} below 7 μm 90% of the machines reach 80% of $\mathcal{L}_0$. It is worth noticing that in the order of 10000 iterations are required in all these cases.

The idea of the following tuning study is to apply an alternative tuning algorithm based on beam based alignment approach in combination with orthogonal knobs for the CLIC BDS L*= 6 m. The obtained results are compared with the ones presented in Table 17, that were obtained when applying the simplex algorithm. Also, the tuning performance of the CLIC BDS with L*= 3.5 m and L*= 6 m designs are compared in terms of number of tuning iterations and number of machines that reach the tuning target.

5.1.1.1 Tuning algorithm

In the following a description of the (BBA + orthogonal knobs) tuning algorithm which is going to be applied is given. Firstly it applies an orbit correction and dispersion free steering with the FFS sextupole and higher order magnets switched off. Both techniques are described in Section 2.4. Secondly the sextupole and high order multipoles are switched on and the whole BBA procedure is applied again. At this stage the pre-computed orthogonal knobs are scanned iteratively in order to maximise the luminosity. Further details about the algorithm are given in Ref. [119].

We have designed the following orthogonal knobs to be scanned at the final stage of the tuning procedure, which are denoted as: β_x^*, α_x^*, β_y^*, α_y^*, η_x^*, $<x,y>$, $<p_x,y>$, $<p_x,p_y>$, η_y^* and $\eta_y'^*$. A short

knob	Horizontal displacements				
	SF6	SF5	SD4	SF1	SD0
	[μm]	[μm]	[μm]	[μm]	[μm]
β_x^*	-5.0	-8.3	-2.0	0.5	0.9
α_x^*	3.5	-2.6	-0.8	-8.9	-5.9
β_y^*	5.3	-0.1	-0.7	2.7	4.4
α_y^*	0.0	-0.5	5.4	-0.9	8.4
η_x^*	-5.8	4.8	-4.8	-3.4	3.1

knob	Vertical displacements				
	SF6	SF5	SD4	SF1	SD0
	[μm]	[μm]	[μm]	[μm]	[μm]
$<x, y>$	-1.8	32.4	9.6	-0.5	-0.2
$<p_x, y>$	0.1	-2.5	-0.7	0.0	0.0
$<p_x, p_y>$	52.4	453.0	125.0	150.0	57.2
η_y^*	-0.2	3.3	0.8	0.0	0.0
$\eta_y'^*$	98.8	-401.4	1128.2	1345.3	512.9

Table 18: Coefficients of sextupole magnet displacements for each horizontal and vertical knob.

description of the function of each knob and their construction is given in Section 2.4. Table 18 summarises the obtained coefficients for each sextupole magnet and each knob. Figure 51 shows the performance of the knobs when they are scanned individually on an error-free CLIC BDS with L*= 6 m lattice. The scanning range of the knobs plotted there goes from -1 to 1 in arbitrary units, that amounts to the displacement of the corresponding sextupole given in Table 18.
Left and right plots in Fig. 51 show the aberration responses when scanning the horizontal and vertical knobs, respectively. In general the orthogonality between knobs is evident except for the β_x^*, β_y^* and $\eta_y'^*$ knobs which are entangled with the α_x^*, α_y^* and $<x, y>$ knobs respectively. Yet when scanning iteratively the $\eta_y'^*$ and $<x, y>$ knobs both aberrations are tuned-out since the $<x, y>$ is orthogonal to the $\eta_y'^*$ knob. However this is not the case for the $\beta_{x,y}^*$ knobs because none of the constructed knobs modify the beta function at the IP, as expected from a sextupole magnet displacement (see Section 2.4.1.3). Recall that these knobs were considered for completeness of the matrix used in their construction. To conclude, the chosen beam aberrations are tuned-out except for the changes in the beta functions at the IP when scanning iteratively this set of knobs.

5.1.1.2 Tuning results

We have performed tuning simulations for 5 different scenarios according to the initial magnet misalignments. The magnets are randomly misaligned according to a Gaussian distribution of width σ_{offset}. The studied values of σ_{offset} are 1, 3, 5, 7 and 10 μm. The errors considered in this study are the same as for the simulation tuning results presented in Table 16 and Table 17. Figure 52 shows the results in terms of the confidence level for all these scenarios. The confidence level represents the curve that accommodates the number of machines that reached a $\mathcal{L}$ larger than $\mathcal{L}_0$ where $\mathcal{L}_0$ is the design luminosity introduced in Table 3. The tuning target is only reached when the value of σ_{offset}= 1 μm, in which case 97% of the machines reach a $\mathcal{L}\geq 1.1\mathcal{L}_0$. The number of machines that reached 80% of $\mathcal{L}_0$ constantly decreases as the value of σ_{offset} increases as summarised in Table 19,

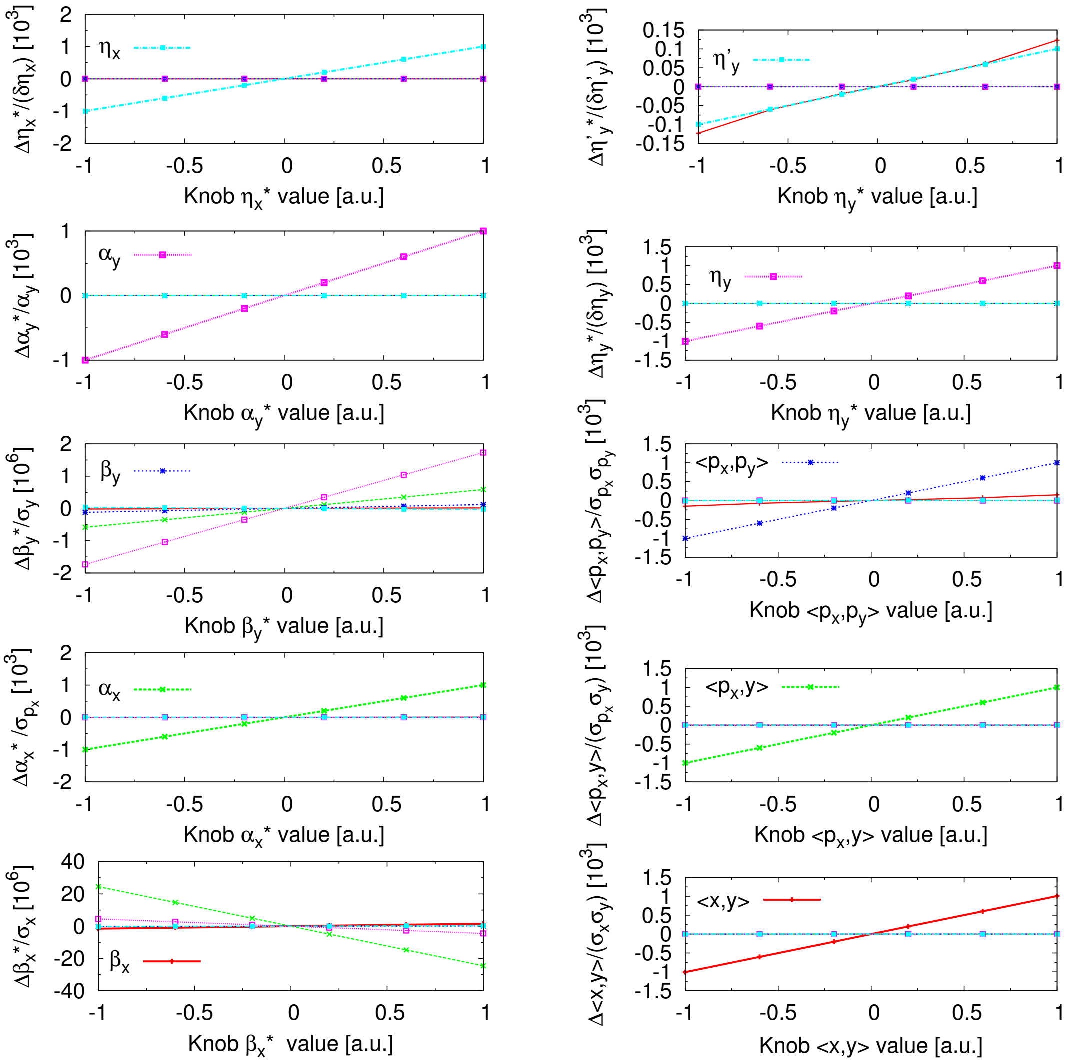

Figure 51: Left plots: Aberrations response when scanning the knobs β_x^* (red), α_x^* (green), β_y^* (blue), α_y^* (purple) and η_x^* (cyan) obtained by moving the sextupole magnets in the horizontal plane. Right plots: Aberrations response when scanning the knobs $<x,y>$ (red), $<p_x,y>$ (green), $<p_x,p_y>$ (blue), η_y^* (purple) and $\eta_y'^*$ (cyan) obtained by moving the sextupole magnets in the vertical plane.

σ_{offset}	Iterations	Success ratio
[μm]	[10^3]	80% of $\mathcal{L}_0$ [%]
1	1.1	100
3	1.2	97
5	1.1	80
7	1.3	58
10	1.4	21

Table 19: Tuning results for the CLIC BDS with L*= 6 m using the (BBA + orthogonal knobs) tuning algorithm. Different scenarios according to the initial random misalignments σ_{offset} of the magnets are considered.

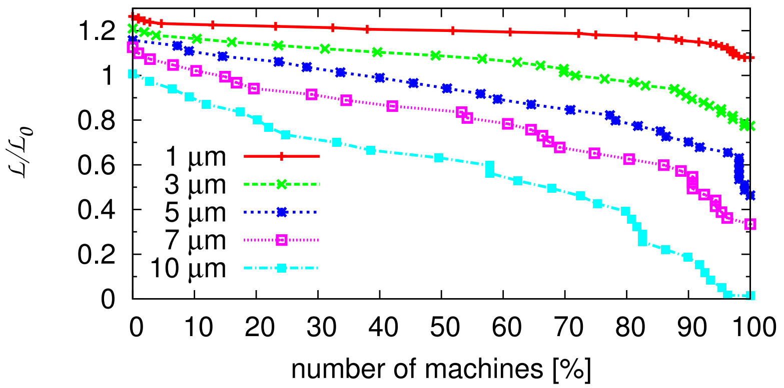

Figure 52: Accumulated curves that account for the results of 100 different machines that reach $\frac{\mathcal{L}}{\mathcal{L}_0}$. The simulation tuning results for the initial misalignment of 1 μm, 3 μm, 5 μm, 7 μm and 10 μm are represented by the red, green, blue, magenta and cyan curves, respectively.

being σ_{offset}= 10 μm the worst scenario in which case only 21% of the simulated machines reach 80% of $\mathcal{L}_0$. Therefore it is evident that the impact of the value σ_{offset} on the tuning performance. The number of required iterations when σ_{offset}= 10 μm is on average 1425 ± 278.

5.1.2 Discussion of the simulations results

Regarding the different tuning algorithms considered to study the CLIC BDS L*= 6 m, the Simplex algorithm reaches better results than the (BBA + orthogonal knobs) algorithm in terms of number of machines that reach 80% of the $\mathcal{L}_0$ for the cases when the value of $\sigma_{\text{offset}} \geq$5 μm. However in terms of number of iterations required for tuning a machine, the Simplex algorithm is almost 10 times slower than the (BBA + orthogonal knobs) one. Similar results were observed in tuning studies of the CLIC BDS L*= 3.5 m.

Comparing the tuning performance between the CLIC BDS lattices, the tuning difficulties clearly increase as L* increases, regardless of the considered tuning algorithm. For the CLIC baseline design, 90% of the machines reach a $\mathcal{L}\leq$90% of $\mathcal{L}_0$ for a value of σ_{offset}=10 μm using the (Simplex + orthogonal knobs) algorithm, while for the CLIC BDS L*= 6 m lattice, 81% of machines are successfully tuned to 80% of $\mathcal{L}_0$ if σ_{offset}=8 μm. For σ_{offset}= 10 μm the (BBA + orthogonal knobs) algorithm is capable to recover 60% of CLIC BDS L*=3.5 m machines with a $\mathcal{L} \geq$ 80% of $\mathcal{L}_0$, whereas only of 21% of the CLIC BDS L*=6 m machines.

As a final conclusion, further improvements of the tuning algorithms are required in order to meet the tuning target for both CLIC BDS designs for values of σ_{offset} >1 μm.

5.2 ATF2 Tuning

We have also performed tuning simulations of the ATF2 FFS which results are presented in this section. The ATF2 is described in detail in Section 3.2.1. The tuning study was done for the new designs ATF2 Bx2.5By1.0 and ATF2 Ultra-low β_y^* lattices described in Sections 4.2.5 and 4.2.6 respectively.

The chromaticity of the ATF2 Ultra-low β_y^* is larger than that of the ATF2 Nominal lattice as explained in Section 3.2.1. This is mainly due to the smaller value of β_y^* according to Eq. (27). In previous tuning studies [79] in which the Simplex was considered as the tuning algorithm, serious

β_y^*	Tuning time	Ratio of success
[μm]	[days]	[%]
100	5.5	100
50	8.0	90
25	10.0	80

Table 20: Tuning performance of the ATF2 lattice for different values of the IP vertical beta function. The Simplex algorithm described in Section 2.4 was implemented in the tuning study (Data taken from [79]).

tuning difficulties were observed as the chromaticity of the lattice increases, Table 20 summarises the obtained results for that study.

The ATF2 beam line comprises the extraction and final focus system beam lines, as presented in Section 3.2.1. The general tuning procedure of ATF2 reported in Ref. [120] consists of the following basic steps:

1. Beam based alignment: to generate a good beam quality and maintain a low background signal at the Shintake monitor.
2. Orbit response and jitter modelling: validation of the current online model by cross checking with the orbit response at the BPMs.
3. Orbit steering: using the orbit correction algorithm, described in Section 2.4.1, the beam is steered flat using the available EXT line correctors and the FFS magnet movers.
4. Dispersion and coupling correction: the dispersion and coupling generated in the EXT and FFS is measured and corrected as described in Ref. [121] and [122] respectively.
5. Twiss parameters and emittance measurement: before entering into the IP beam tuning, the measurement of the Twiss parameters is carried out as explained in Ref. [123] in order to avoid any miss-match between the EXT beam line and the FFS. In addition the emittance measurement [123] determines the minimum achievable IP spot size according to the given Twiss parameters, as Eq. (11) shows.

After completing the above tuning procedure, residual aberrations still remain at the IP that cause a vertical beam size significantly larger than the design value. The IP beam tuning procedure takes place. The following tuning study assumes that the beam coming out from the extraction line is properly tuned, so that the errors are only due to the FFS magnets. The tuning study includes 100 machines with different initial error distributions in order to determine the tuning feasibility.

The implemented tuning algorithm is based on pre-computed orthogonal knobs which are described in Section 2.4, the set of knobs to be applied are denoted as: β_x^*, β_y^*, α_x^*, α_y^*, η_x^*, $<x,y>$, $<p_x,y>$, $<p_x,p_y>$, η_y^* and $\eta_y'^*$, which are constructed as described in Section 2.4. These knobs are iteratively scanned until the vertical beam size at the IP measured by the Shintake monitor converges to its minimum value.

The errors considered in the tuning study of ATF2 are summarised in Table 21. They are assigned following a random Gaussian distribution of width σ_{error}. The measured multipole components discussed in Section 4.2.1.3 are included into the ATF2 tuning simulations.

Error	σ_{error}
Transverse misalignments	30 μm
Transverse rotations	300 μrad
Relative magnet miss-powering	10^{-4}
Beam size measurement	4%

Table 21: Considered errors in the ATF2 simulation tuning study obtained from [124]. σ_{error} refers to the width of the Gaussian distribution which is used to assign the errors.

knob	Horizontal displacements				
	SF6	SF5	SD4	SF1	SD0
	[μm]	[μm]	[μm]	[μm]	[μm]
β_x^*	-5.6	-8.1	0.1	-1.7	-0.3
α_x^*	0.3	-1.7	-2.7	5.5	7.6
β_y^*	-8.2	5.4	0.4	1.4	0.1
α_y^*	-0.5	0.4	-9.7	-0.2	-3.1
η_x^*	0.0	1.5	-1.6	-8.0	5.5

knob	Vertical displacements				
	SF6	SF5	SD4	SF1	SD0
	[μm]	[μm]	[μm]	[μm]	[μm]
$<x, y>$	0.4	6.7	1.1	-6.6	-3.0
$<p_x, y>$	-9.7	-0.5	2.1	-1.2	0.9
$<p_x, p_y>$	-0.6	7.2	1.4	6.2	2.9
η_y^*	-0.6	1.2	-7.1	-2.8	6.3
$\eta_y'^*$	2.4	-1.1	6.5	-2.8	6.5

Table 22: Coefficients for each sextupole magnet displacement according to the horizontal and vertical knob.

It should be pointed out that the impact of ground motion as a dynamic error is not considered in these tuning studies, because the long term performance of the system is not in the scope of this thesis.

5.2.1 ATF2 Bx2.5By1.0 Tuning results

The ATF2 Bx2.5By1.0 lattice was the design lattice to be used for the ATF2 experimental tuning session in December 2010. It is obtained by increasing the value of β_x^* from 4 mm of the ATF2 Nominal lattice to 10 mm, as described in Section 4.2.5.

Table 22 summarises the sextupole magnet coefficients corresponding to each knob for the ATF2 Bx2.5By1.0 lattice. Figure 53 shows the response of the knobs under consideration when they are scanned individually using an error-free lattice. The orthogonality between all the pre-computed knobs, except for the knob meant to vary the β_y^* function at the IP, is evident.

The tuning results are presented in terms of the confidence level which represents the curve that accommodates the number of machines that reached an IP vertical beam size below the corresponding

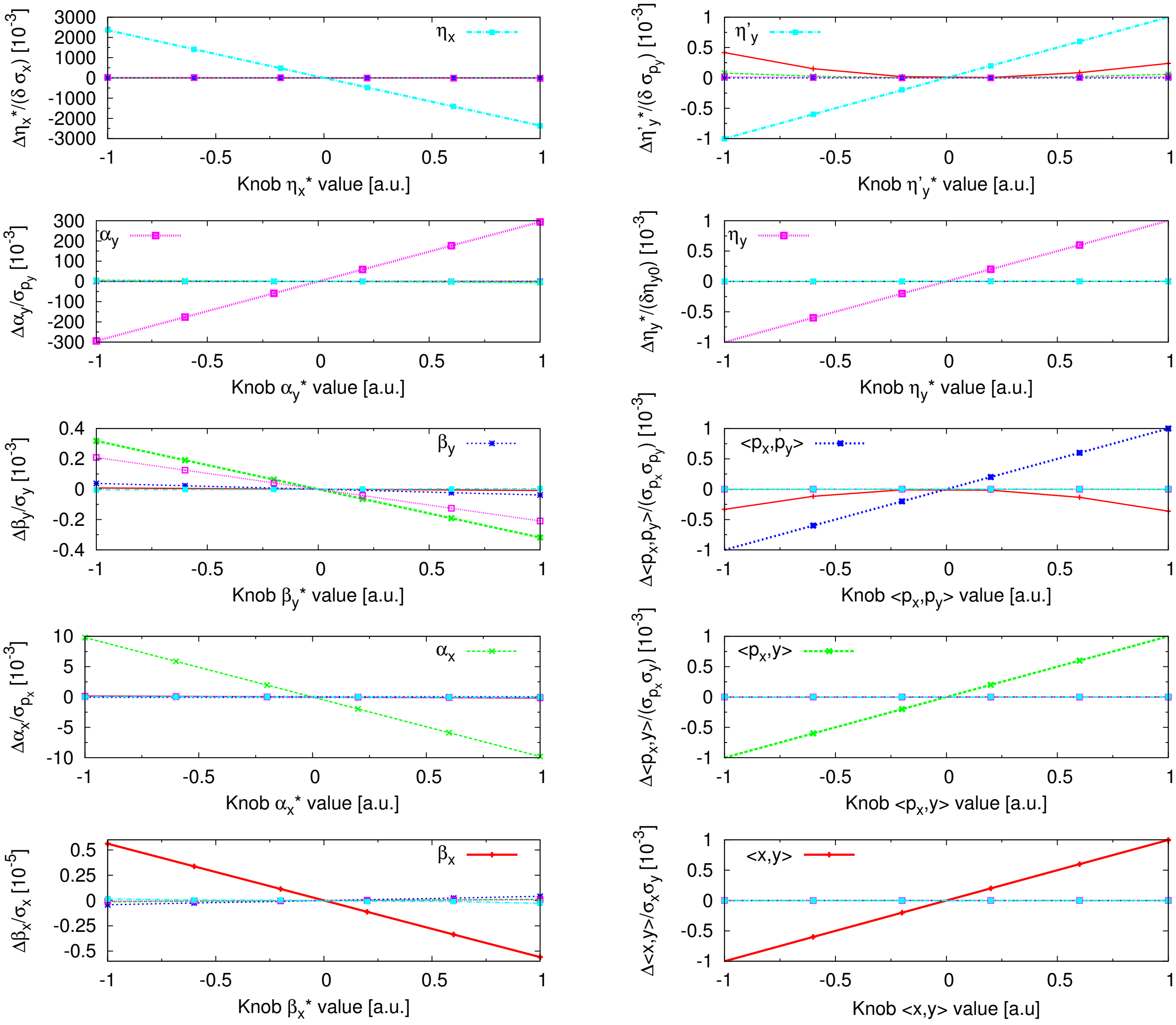

Figure 53: Left plots: Knobs obtained by horizontal sextupole displacements (β_x^*, β_y^*, α_x^*, α_y^*, η_x^*) are represented by red, green, blue, magenta and cyan curves respectively. Right plots: Knobs obtained by vertical sextupole displacements ($<p_x, y>$, η_y^*, $\eta_y'^*$, $<p_x, p_y>$, $<x, y>$) are represented by red, green, blue, magenta and cyan curves respectively.

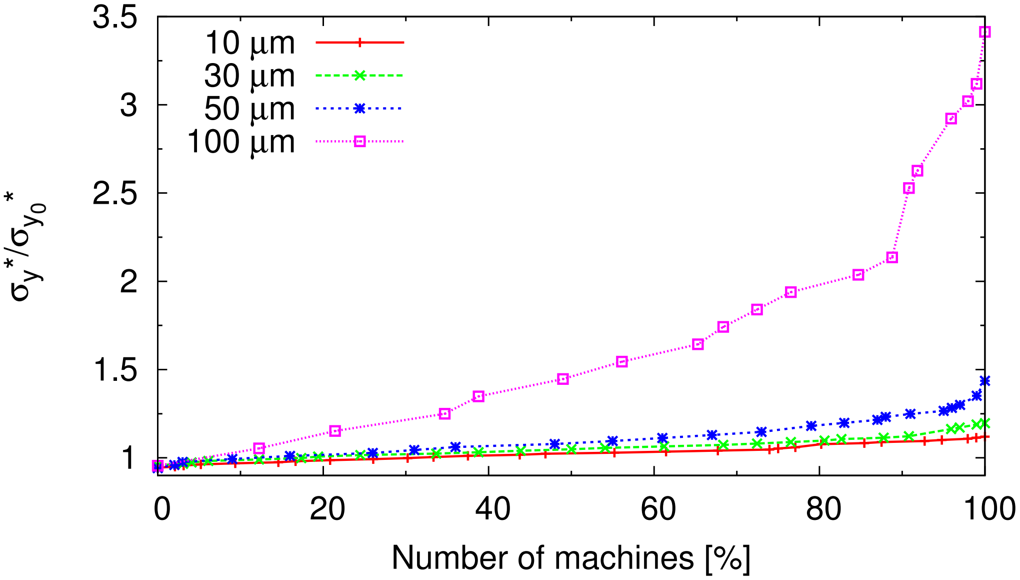

Figure 54: Confidence level after scanning the orthogonal knobs: $<p_x, y>$, α_y^*, $<x, y>$, $\eta_y'^*$, $<p_x, y>$, η_y^* and η_x^*. Red, green, blue and magenta colours correspond to σ_{offset}=10, 30, 50, 100 μm, respectively.

σ_y^*/σ_{y0}^* where σ_{y0}^* is the design vertical beam size at the IP introduced in Section 4.2.5. The confidence level is calculated from the final IP vertical beam size of each machine after scanning the following set of orthogonal knobs: $<p_x, y>$, α_y^*, $<x, y>$, $\eta_y'^*$, $<p_x, y>$, η_y^* and η_x^*. Four different scenarios according to the initial magnet misalignment σ_{offset} are studied. Figure 54 shows the confidence level for the cases when σ_{offset} is equal to 10, 30, 50 and 100 μm, respectively. The most likely value of σ_{offset} is 30 μm, as reported in Ref. [124].

The order in which the set of orthogonal knobs are applied is the following: $<p_x, y>$, α_y^*, $<x, y>$, $\eta_y'^*$, $<p_x, y>$, η_y^* and η_x^*. This is the same order that the knobs were applied during the experimental tuning session in December 2010.

Figure 55 compares the simulation results with the experimental data. Red dots represent the IP vertical beam size averaged over the 100 simulated machines and green curves enclose ±1 standard deviation after scanning each knob.

The initial σ_y^* measured by the Shintake monitor during the experimental session before applying the orthogonal knobs was about 1.2 μm, 50% larger than expected from simulations. The blue dots of Fig. 55 show the IP vertical spot sizes measured by the Shintake monitor [125] after scanning each knob. The double blue dots at knob iterations 1 and 3 correspond to an optimisation of the Shintake monitor. The minimum IP vertical beam size measured by the Shintake monitor is 304 ±40 nm, the error corresponds to the quadratic sum of the systematic error of the Shintake monitor error (which is 10%, see Ref. [125]) and the standard deviation of three different Shintake measurements that are taken after each knob scan. No further minimisation of the IP beam size was made due to stability problems in the laser of the Shintake monitor when switching from 8 to 30 degree mode, during the experimental session of December 2010 as described in Ref. [126].

The smallest IP vertical beam size measured at the ATF2 beam line up to the time of writing this thesis is 168±2 nm, the error corresponds to the rms value of 10 measurements using the 30 degree mode of the Shintake monitor, more details are given in Ref. [127].

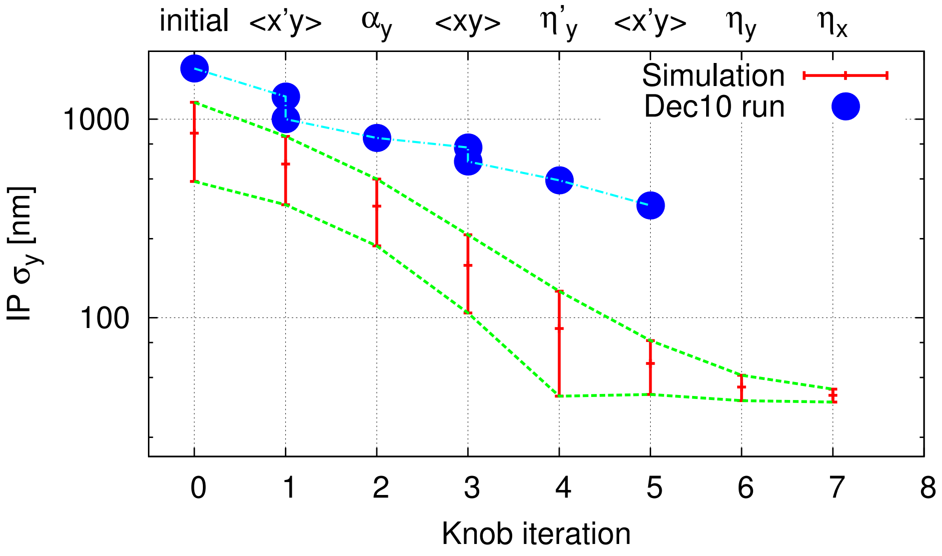

Figure 55: The blue data points represent the experimental tuning results for the ATF2 Bx2.5By1.0 lattice. The red dots represent the simulation tuning results for the same lattice.

5.2.2 ATF2 Ultra-low β_y^* Tuning results

We have also performed the tuning simulation study for the new ATF2 Ultra-low β_y^* lattice which is described in Section 4.2.6, the obtained results are presented in this section. 100 simulated ATF2 Ultra-low β_y^* machines with different initial error configurations are considered to study the tuning feasibility of this lattice. The assumed errors are the same as the ones used for the tuning study of the ATF2 Bx2.5By1.0 lattice, these are summarised in Table 21. The measured multipole components are included in the tuning study.

The tuning study is based on pre-computed orthogonal knobs, the calculated knob coefficients for this lattice are summarised in Table 23. The response of the aberrations when the knobs are scanned using an error-free lattice is shown in Fig. 56. Almost all the knobs show a good orthogonality except β_y^*, $<p_x, p_y>$ and $\eta_y'^*$.

The order of application of the orthogonal knobs has been optimised for tuning the ATF2 Ultra-low β_y^* lattice. In this sense the knobs are sorted according to their efficiency to minimise σ_y^*. To figure out the best knob ordering, the whole set of knobs are applied individually to 50 different machines. Figure 57 shows the $\Delta\sigma_y^*$ provided by each single knob at the first scan. The $<p_x, y>$ knob turns out to be the most efficient, as shown by the red curve in Fig. 57. The second iteration is formed by applying the $<p_x, y>$ knob to 50 different machines and afterwards all knobs are individually scanned except the $<p_x, y>$ knob. The green curve in Fig. 57 shows that the α_y^* knob is the most efficient at this step. The third iteration consists of applying firstly the $<p_x, y>$ and secondly the α_y^* knobs to 50 different machines, at this stage all knobs are scanned except the α_y knob. The blue curve of Fig. 57 shows that the $<\eta_y^*>$ knob is the most efficient at the third iteration. The last knob iteration is performed by applying the $<p_x, y>$, α_y^* and η_y^* knobs to 50 different machines, at this stage all the knobs are scanned except the η_y^* knob. Magenta curve of Fig. 57 shows that the $<p_x, y>$ knob is the most efficient at the fourth iteration. Therefore the order of the first 4 knobs in the tuning algorithm for the ATF2 Ultra-low β_y^* lattice is chosen to be: $<p_x, y>$, α_y^*, $<\eta_y^*>$ and $<p_x, y>$. No further iterations are considered, since as it will be shown below, the first 4 iterations are the most

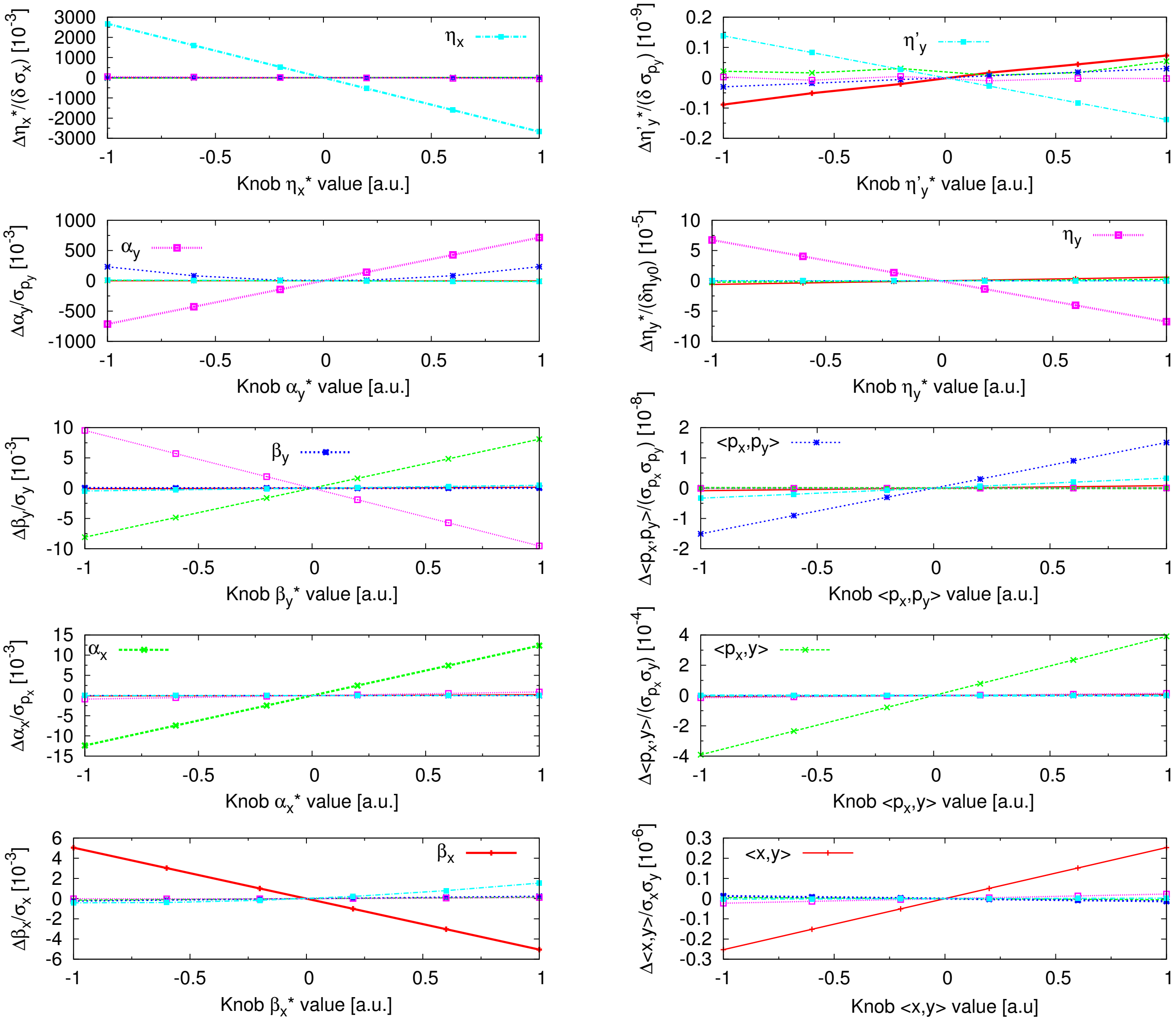

Figure 56: Left plots: Knobs obtained by horizontal sextupole displacements (β_x^*, β_y^*, α_x^*, α_y^*, η_x^*) represented by red, green, blue, magenta and cyan curves respectively. Right plots: Knobs obtained by vertical sextupole displacements ($<p_x, y>$, η_y^*, $\eta_y'^*$, $<p_x, p_y>$, $<x, y>$) represented by red, green, blue, magenta and clan curves respectively.

knob	Horizontal displacements				
	SF6	SF5	SD4	SF1	SD0
	[μm]	[μm]	[μm]	[μm]	[μm]
β_x^*	-0.35	9.99	0.01	-0.14	0.01
α_x^*	-7.18	-0.20	-0.83	3.92	5.70
β_y^*	6.85	0.29	-2.49	4.12	5.46
α_y^*	-1.17	-0.03	-9.49	0.07	-2.91
η_x^*	0.01	-0.12	-1.72	-8.22	5.42

knob	Vertical displacements				
	SF6	SF5	SD4	SF1	SD0
	[μm]	[μm]	[μm]	[μm]	[μm]
η_y^*	0.68	0.09	6.76	3.15	-6.62
$\eta_y^{\prime *}$	3.15	-0.03	-9.49	0.07	-2.91
$<x, y>$	7.69	0.01	-3.23	5.52	0.12
$<p_x, y>$	4.51	0.10	6.35	-2.69	5.66
$<p_x, p_y>$	4.48	0.47	-1.87	-7.23	-4.89

Table 23: Coefficients for each sextupole magnet displacement for the horizontal and vertical knobs.

effective.

The statistical tuning study for the ATF2 Ultra-low β_y^* with the σ_{offset} equal to 10, 30, 50 and 100 μm is carried out.

The upper plot in Fig. 58 shows the mean IP vertical beam size calculated by the Shintake monitor over 100 ATF2 Ultra-low β_y^* machines after scanning the pre-computed knobs for all cases of σ_{offset}. In all scenarios the convergence is mostly achieved after 4 knob iterations. For σ_{offset} equal to 10 μm and 30 μm the obtained $< \sigma_{\text{Shi}}^* >$ values are 27 and 30 nm respectively. However when the value of σ_{offset} is equal to 50 μm and 100 μm the tuning algorithm is not able to reduce the final average value of σ_{Shi}^* below 40 nm and 60 nm respectively. The lower plot in Fig. 58 shows the confidence level evaluated according to the Shintake definition for $\sigma_{\text{offset}}=$ 10, 30, 50 μm. The set of knobs is applied 2 times. For cases when σ_{offset} is equal to 50 and 100 μm the confidence level shows that the tuning knobs are not able to minimise σ_y^* to the design vertical beam size σ_{y0}^* discussed in Section 4.2.6.

5.2.3 Discussion of the results

From the results of the simulations for the ATF2 Bx2.5By1.0 lattice we conclude that tuning based on the knobs presented is capable to recover the design IP vertical beam size under realistic error conditions. The current σ_y^* is minimised to the level of 100 nm, for smaller vertical beam sizes the system slowly converges to the design IP vertical beam size σ_{y0}^*. When comparing to the experimental results over the range from 1 μm to 300 nm, both simulation and experimental results show a similar behaviour, however it is also observed that the simulations converge much faster than the experiment. In the case of the ATF2 Ultra-low β_y^* lattice the statistical tuning study based on knobs is capable to recover the expected vertical beam size at the IP under realistic error imperfections. However when σ_{offset} $\geq$50 μm, which is an unlikely scenario, the tuning procedure does not reach satisfactory results. When comparing the simulation tuning results for the ATF2 Bx2.5By1.0 and the ATF2 Ultra-low β_y^* lattices, it can be concluded that larger tuning difficulties are expected for the ATF2 Ultra-low β_y^*

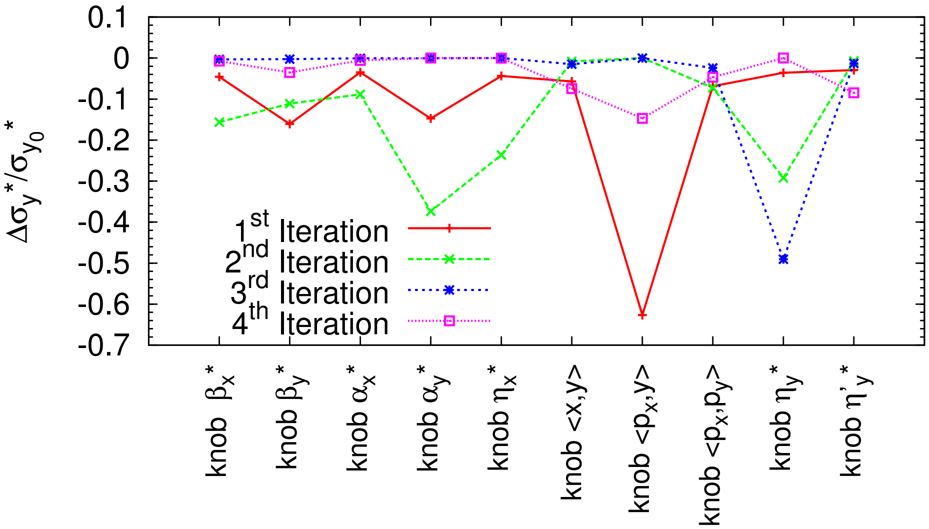

Figure 57: The evolution of the IP vertical beam size from the deviation σ^*_{y0} for tuning with the pre-computed knobs β^*_x, β^*_y, α^*_x, α^*_y, η^*_x, $<x, y>$, $<p_x, y>$, $<p_x, p_y>$, η^*_y and η'^*_y, applied individually at 4 different iterations represented by the red, green, blue and magenta curves respectively.

σ_{offset}	ATF2 Bx2.5By1.0	ATF2 Ultra-low β^*_y
[μm]	$\Delta\sigma^*_y/\sigma^*_{y0}$ [%]	$\Delta\sigma^*_y/\sigma^*_{y0}$ [%]
10	8	9
30	11	35
50	20	80
100	98	250

Table 24: Comparison between the simulation tuning results of the ATF2 Bx2.5By1.0 and the ATF2 Ultra-low β_y lattices for different values of σ_{offset}. $\Delta\sigma^*_y/\sigma^*_{y0}$ refers to the percentage beam size increase that accommodates 80% of the simulated machines for each lattice.

lattice. Table 24 summarises the obtained $\Delta\sigma^*_y/\sigma^*_{y0}$ at the level of 80% of machines for different values of σ_{offset} for both lattices. Figure 59 shows the tuning performance between the ATF2 Bx2.5By1.0 and ATF2 Ultra-low β^*_y lattices when the value of σ_{offset}=30 μm. The initial σ^*_y/σ^*_{y0} before applying the tuning algorithm is larger for the ATF2 Ultra-low β^*_y lattice than for the ATF2 Bx2.5By1.0 lattice. The same is true after applying the tuning algorithm based on orthogonal knobs. As it follows from the tuning difficulties observed in Table 24 and Fig. 59 it can be concluded that more experimental measurements would be necessary to tune the ATF2 Ultra-low β^*_y. It should be noticed that these lattices differ in the value of β^*_x, for the ATF2 Bx2.5By1.0 lattice β^*_x= 10 mm while β^*_x= 6 mm for the ATF2 Ultra-low β^*_y lattice. The impact of this parameter on the tuning difficulties needs to be analysed in further studies.

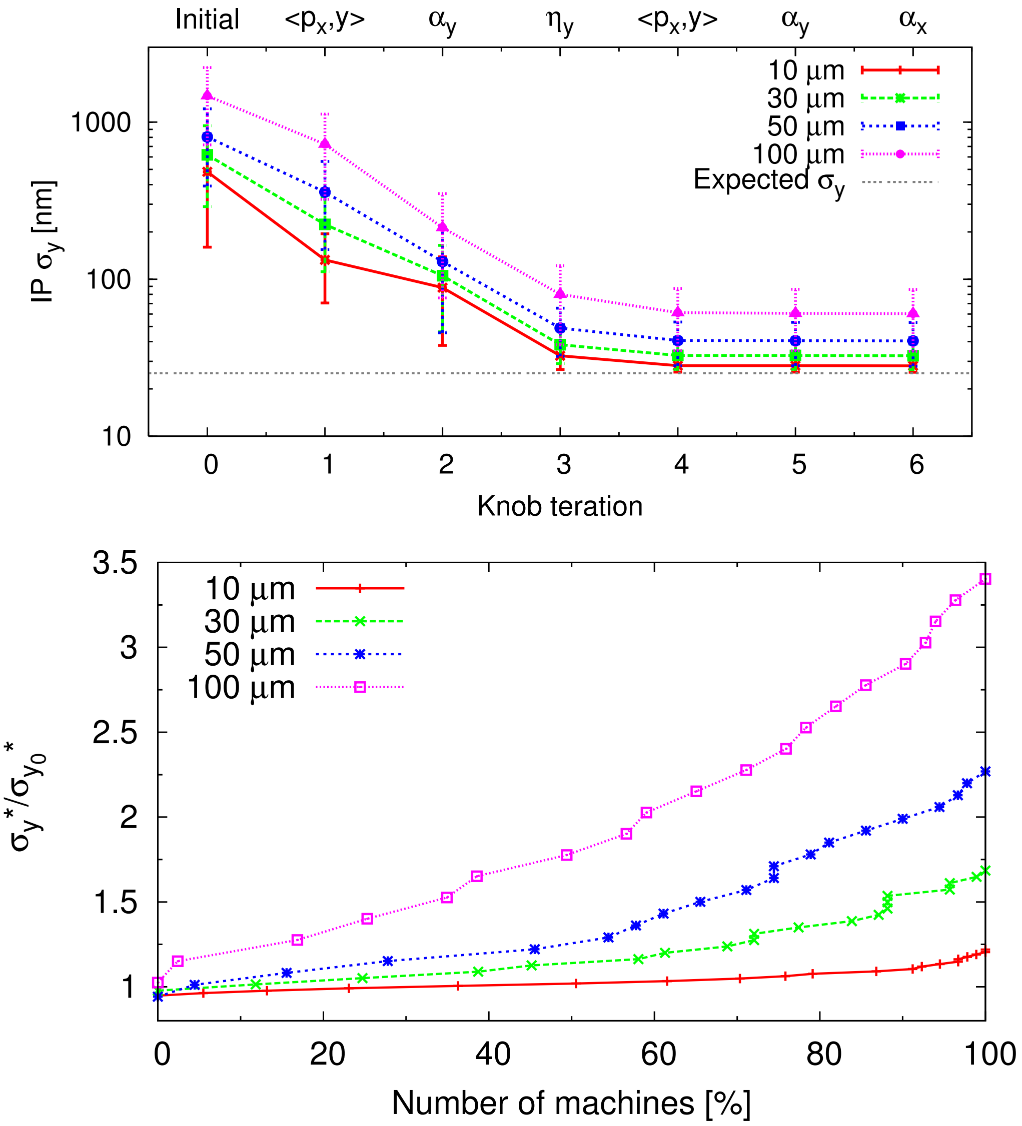

Figure 58: Upper plot: Mean and standard deviation of σ^*_{Shi} over 100 ATF2 Ultra-low β^*_y machines after applying the $<p_x, y>$, α^*_y, $<\eta^*_y>$, $<p_x, y>$, α^*_y and α^*_x. The beam size is calculated according to the Shintake monitor discussed in Section 2.1.2. Red, green, blue and magenta curves show the results according to the value of σ_{offset} equal to 10, 30, 50, and 100 μm, respectively. Lower plot: Confidence level for the different considered scenarios according for different values of σ_{offset}.

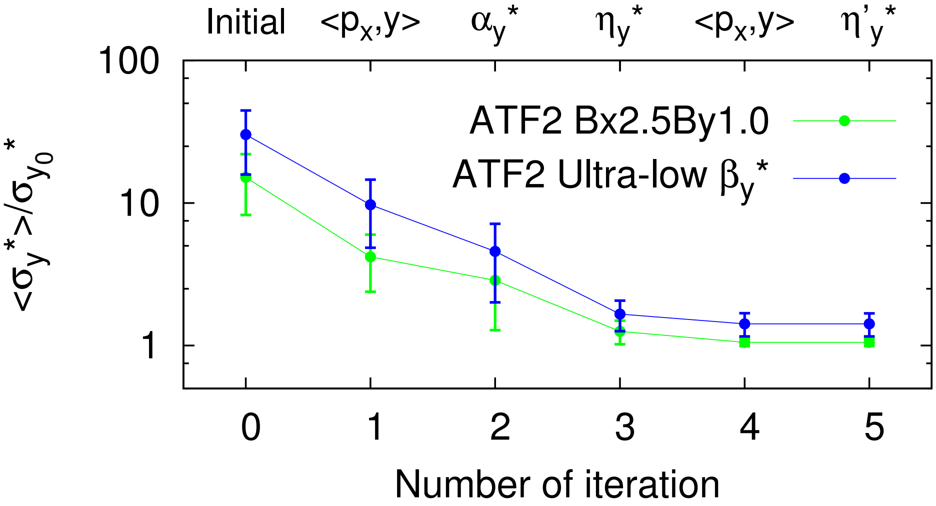

Figure 59: The evolution of the IP vertical beam size from the deviation σ^*_{y0} versus the applied knob iteration when the value of σ_{offset}=30 μm. Green and blue curves show the simulation tuning results the ATF2 Bx2.5By1.0 and ATF2 Ultra-low β^*_y lattices, respectively. Each dot and its error bar are obtained as the mean value and the standard deviation of σ^*_y over 100 machines with different initial conditions. The applied pre-computed knobs are noted at the upper axis of the figure.

6 Beam based alignment results

According to the tuning results presented in Section 5.1.1, the impact of random misalignment of magnets by σ_{offset}= 10 μm for the CLIC BDS with L* = 6 m is severe in terms of number of machines that recover the design luminosity after the tuning process. In contrast, when the value of σ_{offset}= 1 μm is assumed the tuning results significantly improve, as shown in Fig. 52. With respect to the CLIC BDS with L* = 3.5 m the impact of the value of σ_{offset} is not as critical as in the CLIC BDS with L* = 6 m design. Nevertheless reducing the value σ_{offset} would also ease the tuning process.

The error of the beam based alignment arises from a limited resolution of the beam position monitors, errors in magnet movers and power supplies, and the magnetic centre instability when changing the current of a magnet. With the development of BPMs having sub-μm resolution, using the available high stability power supplies for the magnets and implementing high precision magnet movers, the magnetic centre instability becomes a potential limitation to improve the alignment resolution of the quadrupoles in the micrometre regime. The motion of the magnetic centre due to a current variation of the magnet, could be caused by many factors as explained in Ref. [61], being the thermal effect one of the most relevant.

In this section, first two measurements of the magnetic centre position at different currents are discussed in order to illustrate the regime of motion of the magnetic centre. Second, the results of a simulation study are given. This simulation study provides a method to detect and quantify this effect and to determine the BPM resolution and beam orbit jitter, which should be satisfied in order to be sensitive to a magnetic centre motion of the same order as shown in the two magnetic centre measurements. Finally, experimental results obtained at ATF2 and CTF3 test facilities presented in Sections 6.3.1 and 6.3.2 implementing two different beam based techniques are shown. The goal of this section is to determine the limiting factors of the alignment resolution of a quadrupole, in particular characterise the motion of its magnetic centre when changing the current of the magnet.

6.1 Examples of the motion of the magnetic centre

In the initial dedicated magnetic centre measurements of a quadrupole that were conducted by the CERN group in October 2011 and February 2012 and reported in [128], the magnetic centre dependence on the current was obtained for two quadrupole magnets, namely PXMQMAHNAP35 and QFR800 (see Refs. [129] and [130] respectively for their characteristics). The PXMQMAHNAP35 quadrupole measurement consists of ramping up the current from 1 A to 10 A and then ramping it down to 1 A in 12 steps. At each step the magnetic centre position of the magnet is measured by a rotating coil [131]. Similar procedure is applied to the QFR800 quadrupole magnet. Its current is ramped up from 1 A up to 8 A and back to 1 A in 16 steps. At each step the position of the magnetic centre is measured using a vibrating wire [132]. Figures 60 and 61 show the obtained horizontal and vertical magnet centre positions for the PXMQMAHNAP35 and QFR800 magnets, respectively, as a function of the current or equivalently to the normalised integrated gradient. Details of conversion of the magnet current into normalised gradient are given in Appendix C.1.

For the purpose of further comparison we have calculated magnetic centre displacement and its sensitivity to strength variation characteristics for the above results. The obtained $\dot{x}_{\text{mc}}$ and $\dot{y}_{\text{mc}}$ from the measurements of the PXMQMAHNAP35 quadrupole in between k_1=0.17 m^{-1} (2 A) and k_2=0.25 m^{-1} (3 A) are:

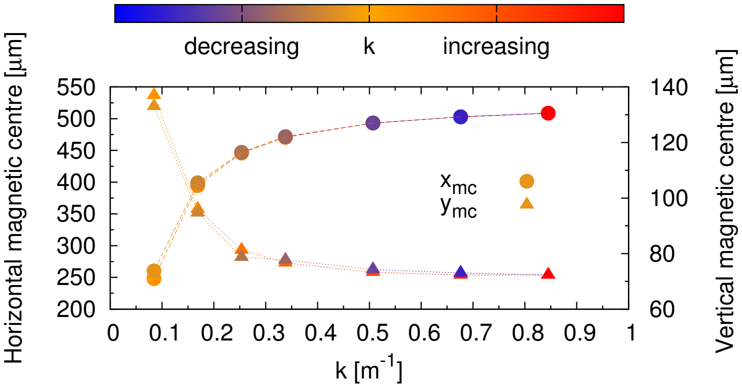

Figure 60: Horizontal (circles) and vertical (triangles) magnetic centre position as a function of the integrated normalised gradient which goes from 0.084 m^{-1} to 0.84 m^{-1} (red) and back to 0.084 m^{-1} (blue). (Data courtesy of J. García Pérez [133]).

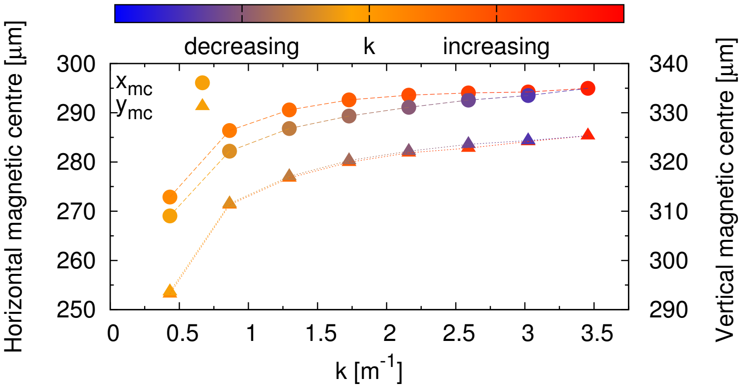

Figure 61: Horizontal (circles) and vertical (triangles) magnetic centre position versus the integrated normalised gradient which goes from 0.44 m^{-1} to 3.56 m^{-1} (red) and back to 0.44 m^{-1} (blue). (Data courtesy of L. Fiscarelli [134]).

$$\text{PXMQMAHNAP35}\quad \begin{cases} x_{k_1} = 394 \pm 4\ \mu\mathrm{m}\ , \quad \mathrm{y}_{\mathrm{k}_1} = 96 \pm 3\ \mu\mathrm{m} \\ x_{k_2} = 447 \pm 2\ \mu\mathrm{m}\ , \quad \mathrm{y}_{\mathrm{k}_2} = 81 \pm 2\ \mu\mathrm{m} \\ \dot{x}_{\mathrm{mc}} = \frac{x_{k_2} - x_{k_1}}{k_2 - k_1} \ = (663 \pm 5)\ \ 10^{-6}\ \mathrm{m}^2 \\ \dot{y}_{\mathrm{mc}} = \frac{y_{k_2} - y_{k_1}}{k_2 - k_1} \ = (-186 \pm 4)\ \ 10^{-6}\ \mathrm{m}^2. \end{cases} \tag{81}$$

The obtained $\dot{x}_{\mathrm{mc}}$ and $\dot{y}_{\mathrm{mc}}$ for the QFR800 magnet in range between k_1=0.89 m^{-1} (2 A) and k_2=1.34 m^{-1} (3 A) are:

$$\text{QFR800}\quad\begin{cases} x_{k_1} = 286.4 \pm 0.2\ \mu\text{m}\ ,\ \ \mathrm{y}_{\mathrm{k}_1} = 311.3 \pm 0.6\ \mu\text{m} \\ x_{k_2} = 290.6 \pm 0.2\ \mu\text{m}\ ,\ \ \mathrm{y}_{\mathrm{k}_2} = 316.8 \pm 0.3\ \mu\text{m} \\ \dot{x}_{\text{mc}} = \frac{x_{k_2} - x_{k_1}}{k_2 - k_1} = (9.3 \pm 0.3)\ \ 10^{-6}\ \text{m}^2 \\ \dot{y}_{\text{mc}} = \frac{y_{k_2} - y_{k_1}}{k_2 - k_1} = (12.2 \pm 0.7)\ \ 10^{-6}\ \text{m}^2. \end{cases} \tag{82}$$

6.2 ATF2 simulation results

In order to apply the BBA quadrupole shunting technique presented in Section 2.3.2 one has to estimate the minimal magnetic centre displacement, which produces a trajectory deviation detectable by the BPMs. With this aim we have performed a simulation study in which a magnetic centre motion is imposed as a function of the current of the magnet. The aim of this study is to estimate the maximum acceptable errors in terms of BPM resolution and beam position jitter that do not preclude to detect the motion of the magnetic centre by the BPMs. The error free ATF2 Bx2.5By1.0 design discussed in 4.2.5 and the QM16FF quadrupole magnet are considered in this study. In the simulation QM16FF quadrupole is moved by 50 μm in the horizontal plane, then the quadrupole current is shunted from -40% to +40% in 9 steps. It is assumed that the magnetic centre of QM16FF moves proportionally to the integrated strength variation $j\ dk$, where j is the step variation and dk is the strength variation. Four different values of $\dot{x}_{\text{mc}}$ have been considered (1, 10, 30, 50 μm·m). Figure 62 shows an example of orbit reading by the downstream monitor MQD4AFF. The different colours represent the 4 different values of $\dot{x}_{\text{mc}}$. Perfect BPM readings and no beam orbit jitter errors are assumed in these calculations. For larger values of $\dot{x}_{\text{mc}}$ the quadratic contribution $(j\ dk)^2$ in Eq. (65) is clearly distinguished from the BPM orbit readings, as Fig. 62 shows. The function $f(j\,dk)$ defined by

$$f(j\ dk) = c_1\ j\ dk + c_2\ j\ dk^2, \tag{83}$$

is used to fit to the orbit readings. The values of $\dot{x}_{\text{mc}}$ and x_0 are determined from the fitted coefficients as follows:

$$\dot{x}_{\text{mc}} = c_2/R_{12}, \tag{84}$$

$$x_0 = c_1/R_{12} - \dot{x}_{\text{mc}}k, \tag{85}$$

where the coefficient R_{12} is the matrix component that maps the x'-coordinate at the QM16FF quadrupole to the x-coordinate at the BPM. The following step is to include BPM errors. A random error with a Gaussian distribution of σ_{orbit} is assigned to all BPM orbit readings. 100 different pulses are used for each configuration of position and current of the magnet. A value of σ_{orbit}= 10 μm is assumed. Figure 63 shows the value of $\dot{x}_{\text{mc}}$ for all BPMs obtained from the fitting coefficients. Each colour represents a different value of $\dot{x}_{\text{mc}}$. A total of 37 cavity BPMs (CBPMs) are installed in the ATF2 beam line, which are attached or close to a quadrupole magnet. The CBPMs are labelled by a prefix M followed by the name of the nearby quadrupole. The BPMs located at positions where the absolute value of R_{12} is larger than 20 m, namely MQM13FF, MQD10AFF, MQF9A/BFF, MQF5A/BFF, MQD4BFF, MQD2AFF and MQF1FF, determine $\dot{x}_{\text{mc}}$ with a good precision. This is due to the fact that higher values of R_{12} amplify the effect on the beam position due to $\dot{x}_{\text{mc}}$, hence, the fitted error is smaller than the orbit variation due to Δk when $\dot{x}_{\text{mc}}$=0. On the contrary, the BPMs located at positions where the absolute value of R_{12} is small, cannot determine $\dot{x}_{\text{mc}}$ with

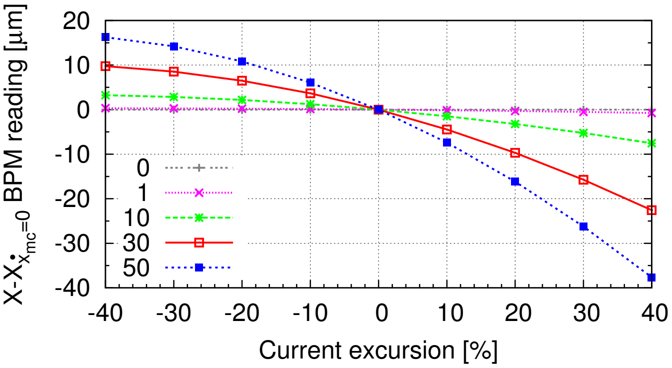

Figure 62: Orbit change in MQD0FF BPM as a function of the strength of QM16FF magnet for different values of $\dot{x}_{\rm mc}$= 1, 10, 30, 50 10^{-6}m^2.

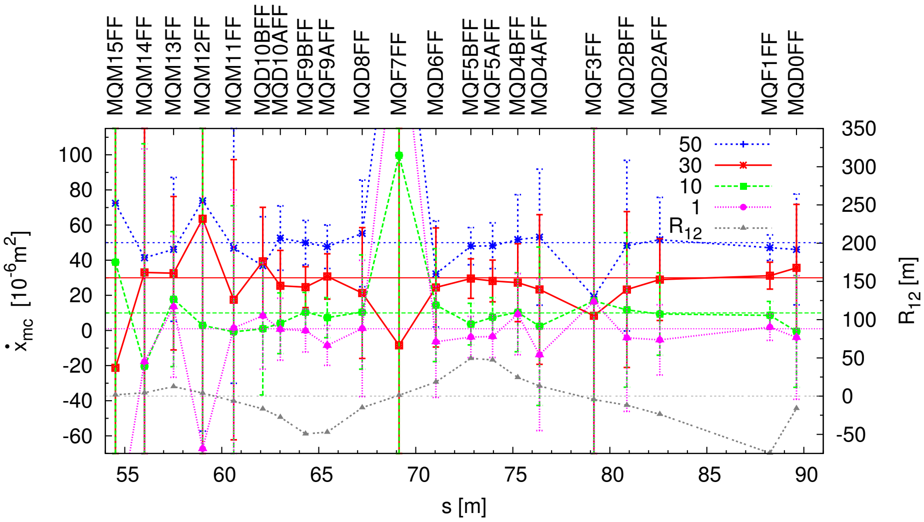

Figure 63: Back reconstructed $\dot{x}_{\rm mc}$ coefficients from the fit coefficients for the downstream BPMs of QM16FF assuming an orbit reading error of 10 μm.

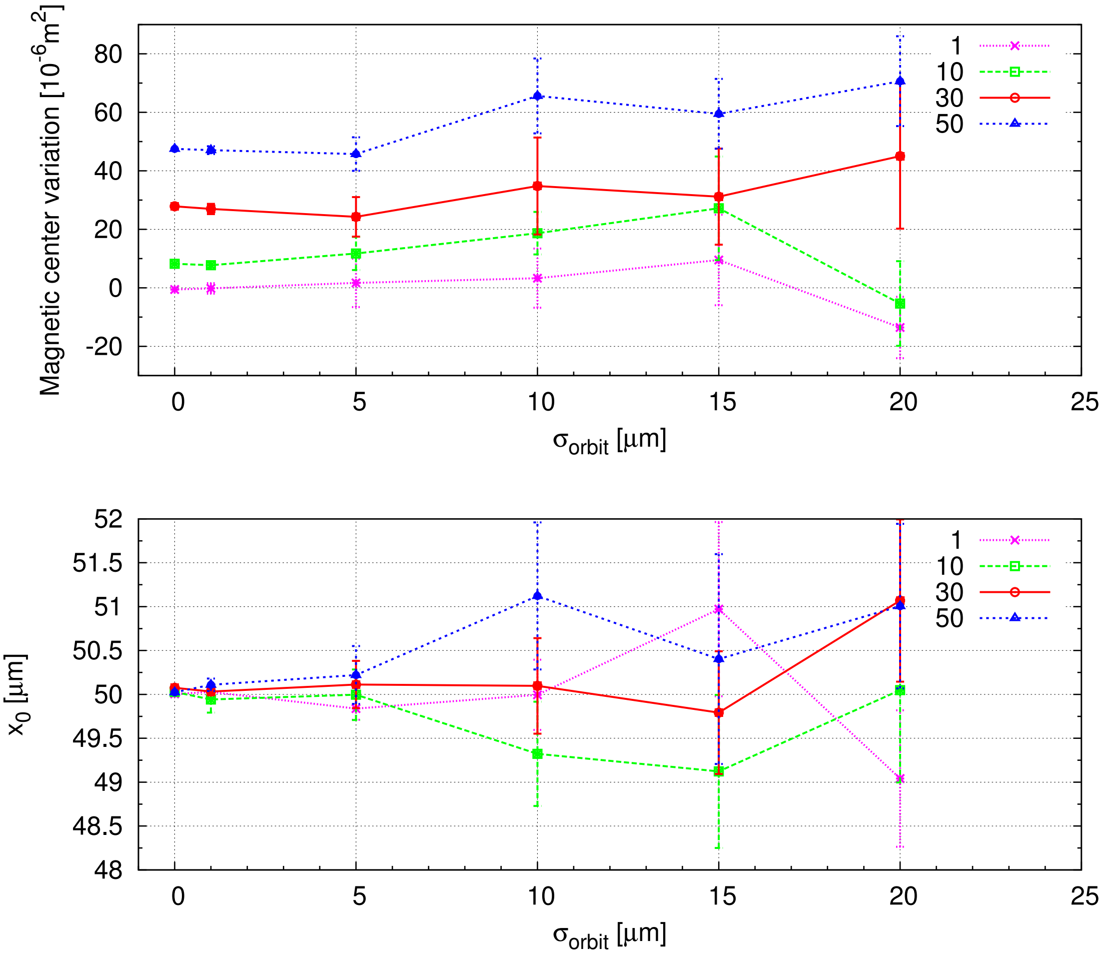

Figure 64: Simulation results obtained for different values of $\dot{x}_{\rm mc}$. Upper plot: Back reconstructed $\dot{x}_{\rm mc}$ coefficients given by the BPMs downstream of QM16FF with $|R_{12}| \geq$10 m as a function of orbit reading errors. Lower plot: Back reconstructed x_0 coefficient given by the BPMs downstream of QM16FF with $|R_{12}| \geq$10 m as a function of the orbit reading error.

sufficient precision because the contribution of $\dot{x}_{\rm mc}$ to the beam position is comparable to the orbit determination error, hence the fitted quadratic coefficient c_2 cannot be precisely measured. The MQM11FF, MQF7FF and MQF3FF BPMs serve as examples since they have values of R_{12} close to 0. Different values of $\sigma_{\rm orbit}$ have been scanned in order to estimate the acceptable orbit reading error to correctly fit $\dot{x}_{\rm mc}$ and x_0. Figure 64 shows the average fitted coefficients using only those BPMs that satisfy the condition $|R_{12}| \geq 10$ m. The upper plot shows the obtained average value of $\dot{x}_{\rm mc}$ over the mentioned BPMs. The back reconstructed coefficient is consistent with the imposed value of $\dot{x}_{\rm mc}$ within the error bars for all values of $\sigma_{\rm orbit}$. The average x_0 coefficient over the mentioned BPMs is correctly determined in all the studied scenarios as the lower plot in Fig. 64 shows.

6.3 Experimental results

Two different measurement campaigns, one at ATF2 in May 2010 and another at CTF3 in July 2011, were conducted with the purpose to study the magnetic centre stability when shunting the quadrupole

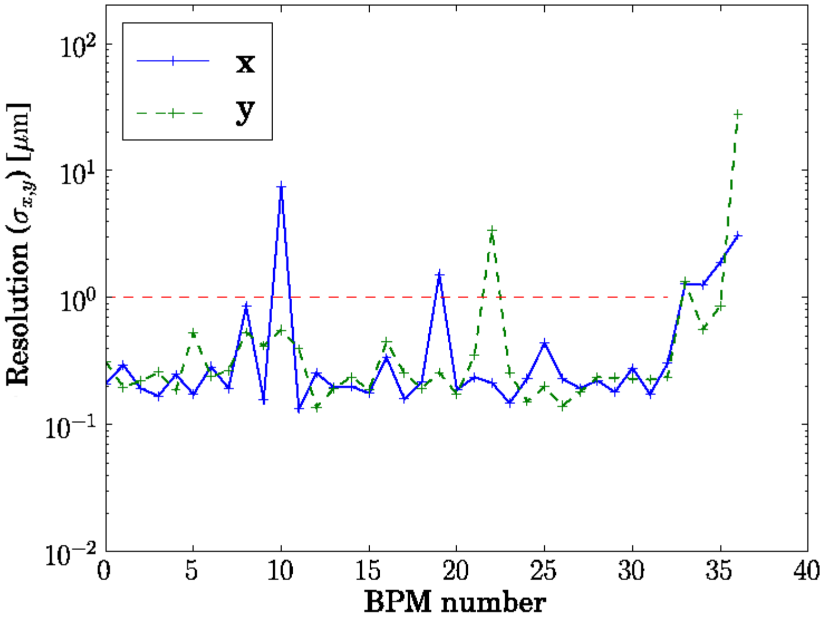

Figure 65: Horizontal and vertical resolution for the ATF2 FFS BPMs, sub-micron resolution is achieved in almost all BPMs for both planes. (Figure courtesy of S. Boogert)

magnet. The first method of determining the motion of the magnetic centre, described in Section 2.3.2, is applied to the measurements at ATF2. The second method described in Section 2.3.2, is used in the second measurement campaign at CTF3.

6.3.1 ATF2

During the measurements at ATF2 the sextupole magnets were switched off in order to avoid non linear response of the beam orbit. The measurement consists of setting different beam orbits at the quadrupole under consideration either by moving the magnet itself to different positions or by shunting the nearest upstream quadrupole magnet. For each orbit the current of the considered magnet is varied within ±20%. It is a nulling technique since no difference in the BPM orbit readings is observed upon the quadrupole current change in case the beam passes through its magnetic centre. Figure 65 shows a typical resolution of the ATF2 cavity BPMs. The average resolution for the 37 CBPMS is of the order of 200 nm, see Ref. [135].
The following three measurements were performed during the ATF2 experimental session in May 2010:

- 1st: QM16FF current is varied from -15% to +15% in 5 steps, to set 5 different orbits at QM15FF. For each orbit the QM15FF current is shunted from -20% to +20% in 5 steps. 20 pulses are recorded for each configuration.
- 2nd: QM15FF is moved from -500 μm to +500 μm in steps of 250 μm, for each position the quadrupole is shunted from -20% to +20% in 5 steps. 20 pulses are recorded for each configuration.

- 3rd: QM13FF is moved from -500 μm to +500 μm in steps of 250 μm, for each position the quadrupole is shunted from -20% to +20% in 5 steps. 20 pulses are recorded for each configuration.

The normalised integrated strength (k) of QM16FF, QM15FF and QM13FF during the measurements are -0.447 m^{-1}, 0.602 m^{-1} and 0.810 m^{-1} respectively. In all measurements 5 different orbits are set either by changing the current of the previous quadrupole magnet (1st measurement) or by moving the quadrupole magnet to 5 different positions (2nd and 3rd measurements) by means of its mover. A description of the precision of the ATF2 quadrupole power supplies and the precision of the ATF2 magnet movers can be found in Refs [71] and [136], respectively.

Figure 66 shows the vertical beam orbit jitter of the beam along the ATF2 beam line for all measurements. The upper plot shows the data of the 1st measurement, which show a larger beam orbit jitter than the 2nd and the 3rd ones, shown in the centre and lower plot, respectively.

The Singular Value Decomposition (SVD) analysis [62] allows to filter out the jitter and enables to reconstruct the orbit with a better precision. For example, in the 1st measurement the orbit reconstruction is a factor 10 more precise, leading to a 10 μm of residual beam orbit jitter in almost all BPMs. The residual orbit jitter for the 2nd measurement is below 10 μm after applying the SVD analysis. The effectiveness of the SVD when applied to the 2nd and 3rd measurement is not so beneficial because the original vertical orbit jitter is already below 10 μm.

In order to determine the value of $\dot{y}_{\mathrm{mc}}$ of a measurement the value of the R_{34} coefficient is required as Eq. (84) shows. The MADX model of ATF2 can provide this coefficient, alternatively it can be determined from the measurement if the offset of the magnet is a known quantity. To this end, the recorded orbit differences Δy of the BPMs when changing the strength of the considered magnet for all five beam trajectories allows to determine the offset of the magnet y_0, as it is explained in Section 2.3.2. As an example Fig. 67 shows the Δy measured by MQD0FF BPM as a function of the mover position where QM13FF is mounted. Figure 68 shows the obtained y_0 by all BPMs for the 3rd measurement.

$<\chi>$ and $\delta\!<\chi>$ are weighted mean and error defined by the following relations:

$$<\chi> = \frac{\sum_i^{\mathrm{BPMs}} \chi_i w_i}{\sum_i^{\mathrm{BPMs}} w_i} \tag{86}$$

$$\delta\!<\chi> = \sqrt{<\chi^2> - <\chi>^2}, \tag{87}$$

where χ_i is the quantity measured by the i^{th} BPM.

The weighted mean of the offset of QM13FF $<y_0>_{\mathrm{QM13FF}}$ and its error $\delta<y_0>_{\mathrm{QM13FF}}$ are obtained according to Eqs. (86) and (87) respectively, identifying χ_i as the offset measured by a BPM and using the weight given by

$$w_i = \frac{|R_{34}|}{(\delta y_0)^2}, \tag{88}$$

The weight w_i is inversely proportional to δy_0 and proportional to the $|R_{34}|$ coefficient because the large absolute value of R_{34} the better resolution is achieved by that BPM. The obtained value of $<y_0>$ for the 3rd measurement is

$$<y_0>_{\mathrm{QM13FF}} = 527 \pm 1.3\ \mu\mathrm{m}.$$

Once the offset of the magnet is determined, the value of the R_{34} coefficient is obtained according to Eq. (61).

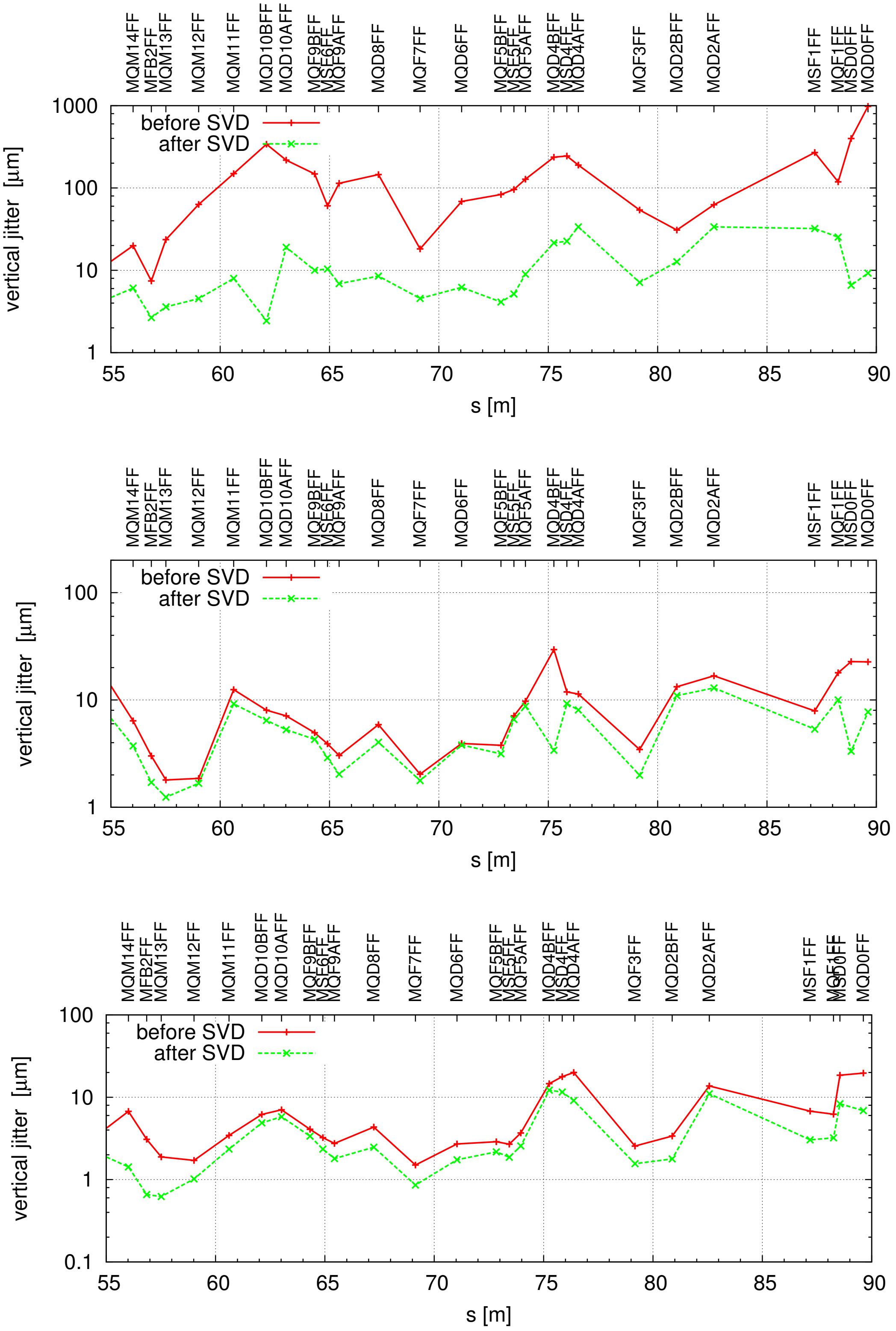

Figure 66: Vertical beam orbit jitter at the BPMs, red and green curves correspond to the data before and after applying the SVD analysis respectively. The upper, centre and lower plots show the jitter for the 1st, 2nd and 3rd measurements, respectively.

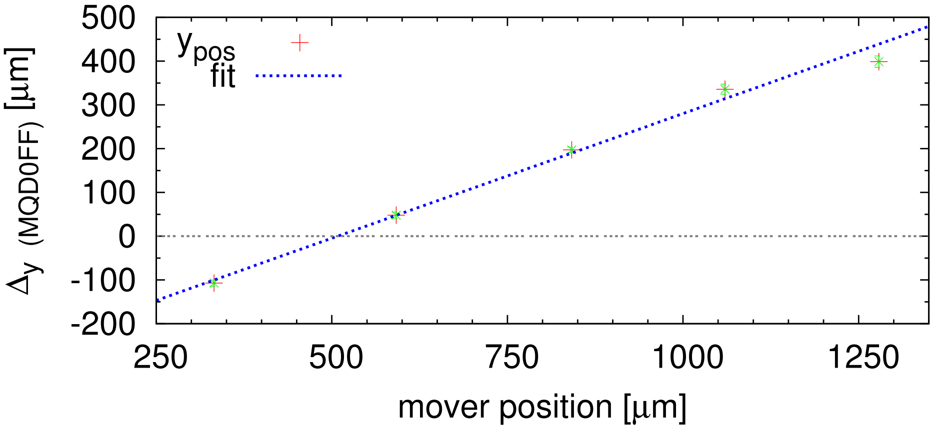

Figure 67: Obtained vertical offset by the MQD0FF BPM for the 3rd measurement.

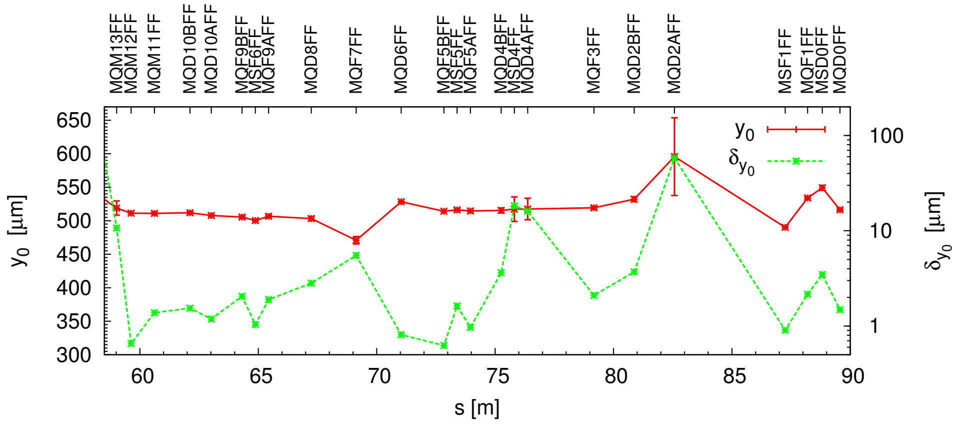

Figure 68: Obtained vertical offset and its error of QM13FF along the beam line for the 3rd measurement.

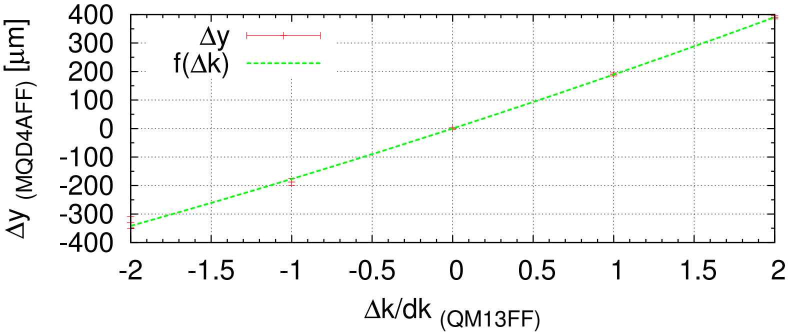

Figure 70: Fit of $\dot{y}_{\mathrm{mc}}$ of QM13FF obtained by MQD4AFF BPM. The data corresponds to the best orbit of the 3rd measurement.

The set of data composed of the five orbits which takes into account the evaluated magnet offset with the BPM orbit reading differences observed at the maximum strength variation ($\Delta k/dk = 2$) of the considered quadrupole, is used to fit the function $f(y)$ defined by:

$$f(y) = c_3\, y, \tag{89}$$

where y represent the five orbits and $f(y)$ the BPM readings. The fitted coefficient c_3 allows to determine the value of R_{34} as

$$R_{34} = \frac{c_3}{\Delta k}, \tag{90}$$

where Δk is the maximum strength variation of the magnet. As an example, Fig. 69 shows the obtained value of R_{34} for the 3rd measurement along the ATF2 beam line.

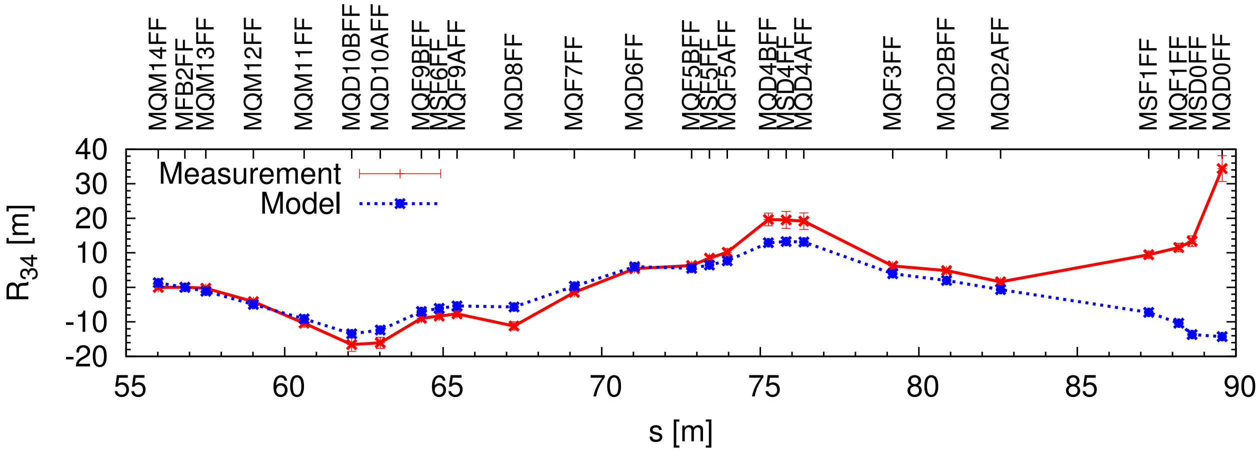

Figure 69: Obtained R_{34} coefficient of QM13FF which corresponds to the 3rd measurement.

Figures 71, 72 and 73 present the obtained $\dot{y}_{\mathrm{mc}}$ coefficients for the 1st, 2nd and 3rd measurements respectively as presented in Section 6.2, but using the values of R_{34} obtained from the measurement instead of using the ones from the model. Only the best orbit out of the 5 is shown, the results for all five orbits for all measurements are given in Appendix B. As an example of fitted $\dot{y}_{\mathrm{mc}}$ coefficient, Fig. 70 shows the parabolic fit of MQD0FF BPM, that corresponds to the best orbit of the 3rd measurement.

Figures 71 and 72 show inconsistent results of the obtained $\dot{y}_{\mathrm{mc}}$ coefficients along the beam line, on

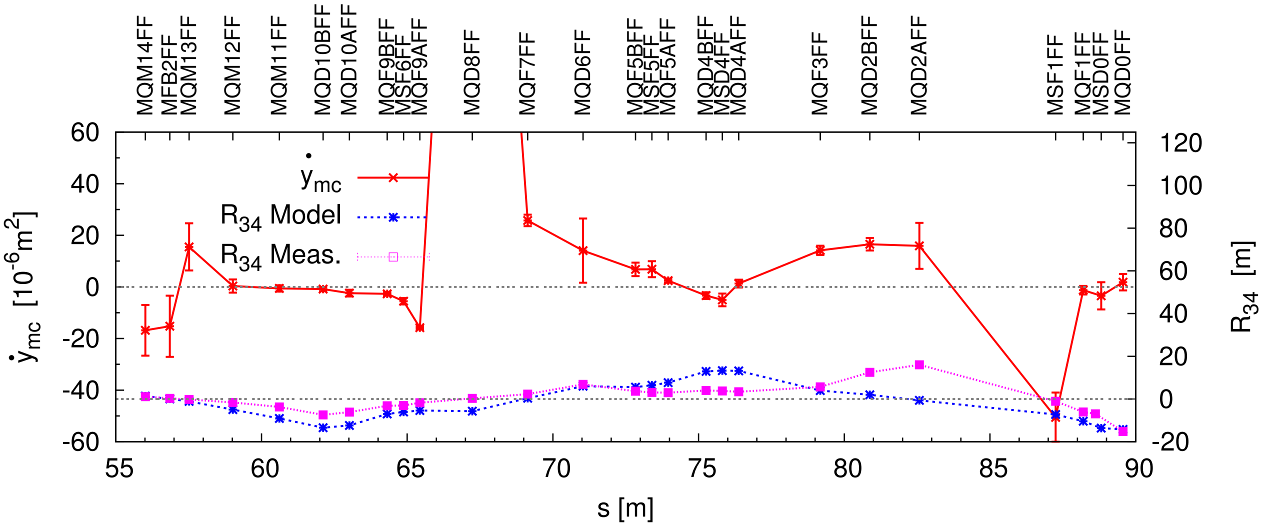

Figure 71: Fitted $\dot{y}_{\rm mc}$ coefficients for the 1st measurement of QM15FF magnet.

Measurement	Magnet	$<\dot{y}_{\rm mc}>$	$\delta<\dot{y}_{\rm mc}>$
		[10^{-6}m^2]	[10^{-6}m^2]
1	QM15FF	1	7
2	QM15FF	-1	1.2
3	QM13FF	-1.6	0.8

Table 25: Weighted average of $\dot{y}_{\rm mc}$ for the 1st, 2nd and 3rd measurements.

the contrary Fig. 73 shows a consistent result along the beam line except the MQD2AFF BPM due to the fact that $R_{34} \approx 0$. The error bar of $\dot{y}_{\rm mc}$ considers two contributions, as Eq. (91) shows, the error from the fit of Eq. (83) to the BPM data δy_0 and the one obtained by the evaluation of the R_{34} coefficient δ_R from the measurement.

$$\delta\dot{y}_{\rm mc} = \sqrt{\left(\frac{\delta y_0}{R_{34}}\right)^2 + \left(\frac{y_0}{R_{34}^2}\delta_R\right)^2}. \tag{91}$$

The observed inconsistent results can be explained by the observed discrepancies between the obtained R_{34} coefficient from the measurement with the one obtained from the model of ATF2, as it is shown by the blue and magenta curves of Figs. 71, 72 and 73.
The mean value and its error is obtained according to Eq. (86) and (87) respectively identifying $\chi = \dot{y}^i_{\rm mc}$ and using as a weight w_i:

$$w_i = \frac{|R^i_{34}|}{(\delta\dot{y}^i_{\rm mc})^2}. \tag{92}$$

Table 25 summarises the values of $<\dot{y}_{\rm mc}>$ and $\delta<\dot{y}_{\rm mc}>$, for all measurements. The error obtained in the 1st measurement is almost an order of magnitude larger than the one of the 2nd and 3rd measurements. In order to understand the impact of using an upstream quadrupole to set different orbits when determining the value of $\dot{y}_{\rm mc}$, further simulation studies and beam based alignment measurements would be necessary.

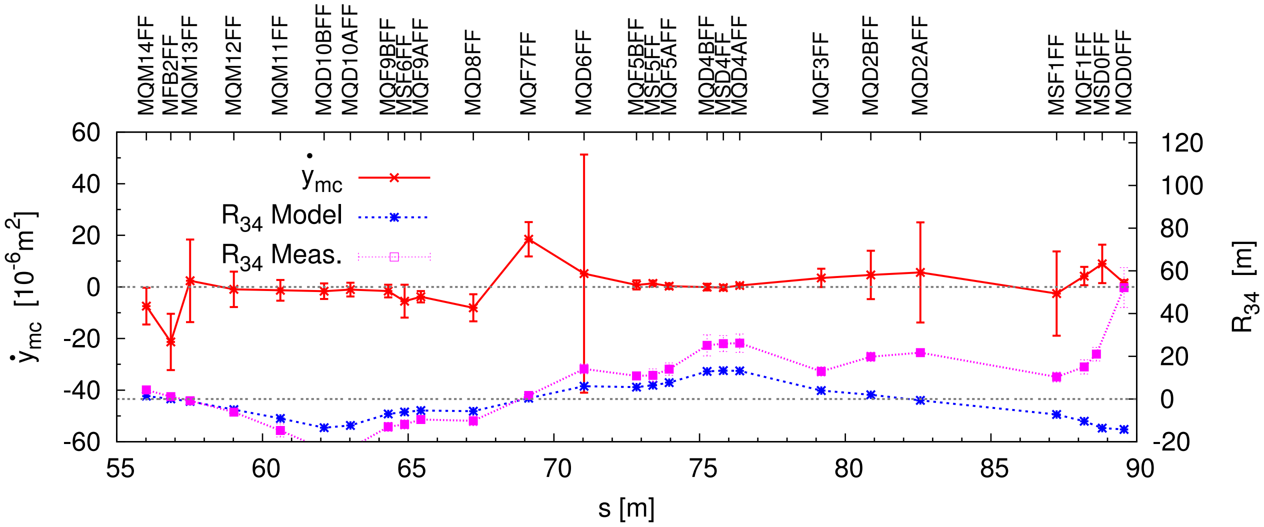

Figure 72: Fitted $\dot{y}_{\mathrm{mc}}$ coefficients for the 2nd measurement of QM15FF.

The value of $\dot{y}_{\mathrm{mc}}$ of the QM15FF magnet is equal to $(0\pm7) \cdot 10^{-6}$ m^2 which is obtained as the mean value of the 1st and 2nd measurements, and the error is the larger of both measurements. The $\dot{y}_{\mathrm{mc}}$ coefficient for QM13FF is $(-1.6\pm0.8) \cdot 10^{-6}$ m^2. This implies that the magnetic centres of QM15FF and QM13FF move 0±0.9 μm and -0.26±0.12 μm respectively for a strength variation of 20% respectively.

6.3.2 CTF3

In this section the results of the magnetic centre measurements and magnetic centre motion characterisation for the QFR300 quadrupole magnet [137] are presented. The QFR300 quadrupole belongs to the Test Beam Line (TBL) located at the CTF3 facility presented in Section 3.3. The technique used to measure and characterise the magnetic centre stability consists of moving the quadrupole to three different positions by means of a mover on which the magnet is mounted. The mover characteristics are detailed in Ref. [138]. At each position the current of the QFR300 quadrupole is initially shunted by ±10%. 20 orbit readings are recorded for each setting of position and current. From the orbit difference recorded by the downstream BPMs [139] the magnetic centre is inferred when the orbit difference is null. The magnet position and the current variation are adjusted at each iteration in order to avoid significant beam losses during the measurement and until the obtained BBA resolution does not further improve. This procedure is applied to measure the position of the magnetic centre at the nominal current of the QFR300 magnet and at a current increased by +20% from the nominal. The coefficient $\dot{y}_{mc}$ is obtained from the difference between the magnetic centre positions measured at nominal current and the one measured at a current increased by +20%.

The beam intensity at the entrance of TBL during the experimental session of the 21st of July was about 13 A as it is shown in Fig. 75. This intensity is produced by factor 4 pulse recombination as it is described in Section 3.3. On one hand this high intensity produces a clear signal on the BPMs, but on the other hand, beam losses may occur during its transport through the TBL, due to an increase of the transverse beam size as a result of a non perfect recombination of the bunches.

The data recorded by 17 BPMs of TBL are used to perform the SVD analysis. The beam orbit jitter is calculated as the standard deviation of the 20 orbit reading pulses that correspond to the same orbit.

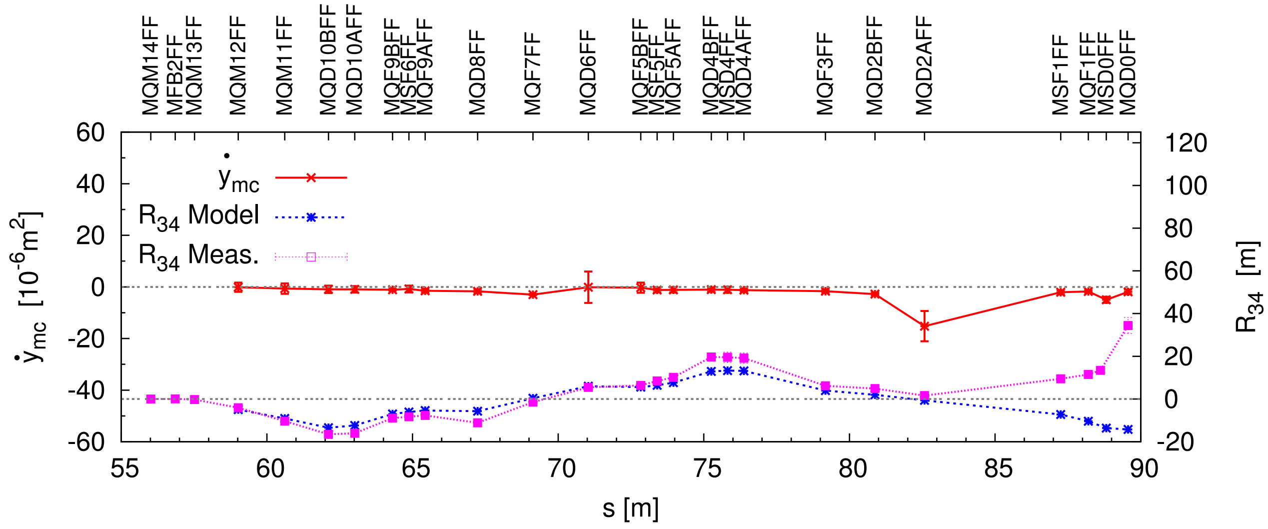

Figure 73: Fitted $\dot{y}_{\rm mc}$ coefficients of magnet QM13FF.

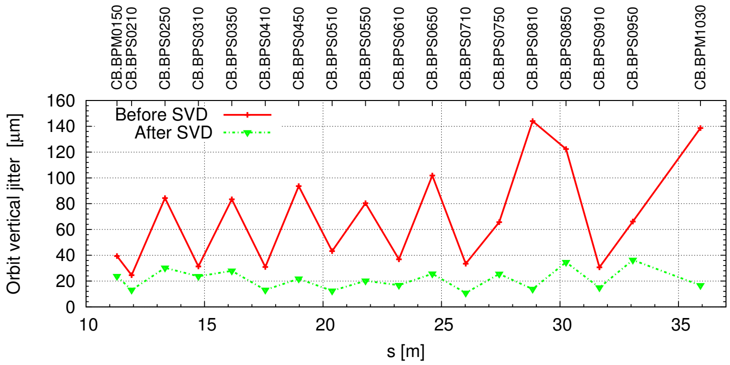

Figure 74: Vertical orbit precision before and after applying the SVD.

Figure 74 shows the incoming vertical orbit jitter (red) and the reconstructed orbit jitter (green) after applying the SVD analysis [62] along the entire TBL beam line. This approach allows to reconstruct the orbit with on average factor 4 better precision comparing to the regular mean.

Measurement of the magnetic centre of QFR300 was done for two different currents, I_1=2.56 A and I_2=2.95 A. For each current the position of the magnetic centre is determined by moving the quadrupole magnet to 3 different positions, at each position the variation of the quadrupole strength is set to ±20%. Figure 76 shows the BPMs reading variation Δy between the orbit when the current is -20% and 20% for the three positions. The value of Δy and its error $\delta_{\Delta y}$ are obtained as

$$\Delta y = < y_{+20\%} > - < y_{-20\%} >, \tag{93}$$

$$\delta_{\Delta y} = \sqrt{\delta^2_{-20\%} + \delta^2_{+20\%}}, \tag{94}$$

where $< y_{-20\%} >$ and $< y_{+20\%} >$ are obtained as the mean over 20 pulses for each orbit and the errors $\delta_{-20\%}$ and $\delta_{+20\%}$ are evaluated as the rms of the 20 pulses. The magnetic centre position obtained for some BPMs differ by more than 3 σ from the weighted mean defined in Eq. (86). This discrepancy

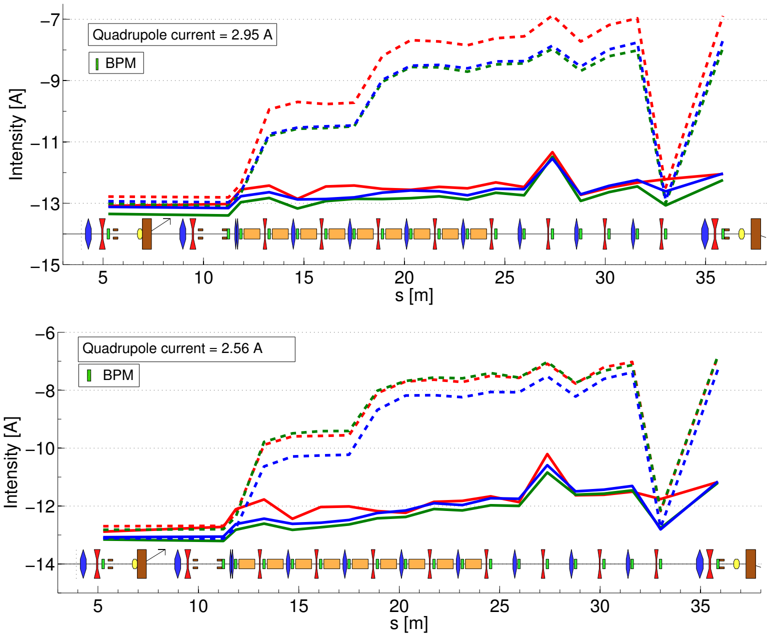

Figure 75: Measured beam intensity by all TBL BPMs. Each colour represents a different quadrupole magnet position. Continuous and dashed lines refer to ±20% current variation. Upper and lower plots show the measurement for the currents I_1 and I_2 respectively.

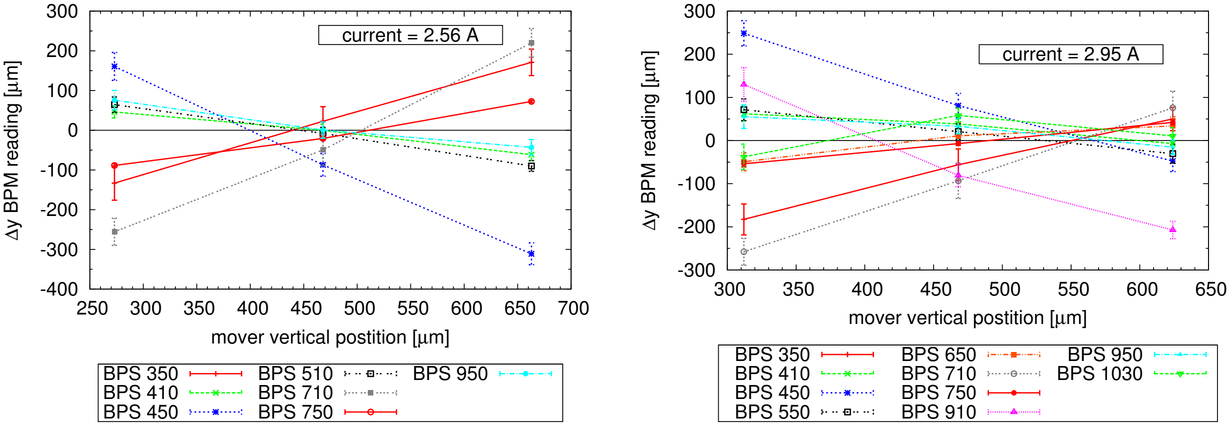

Figure 76: Change of the vertical BPM orbit readings as a function of the QFR300 vertical position. Each colour represents a different BPM. Left and right plots show the results when the magnet current is set to 2.56 A and 2.95 A, respectively.

could be explained by the beam losses that eventually occur during the measurement, as Fig. 75 shows. Those BPMs results are neglected in the analysis.

Using the weighted average definition in Eqs. (86) and (87) and the inverse of the quadratic fit error as the weight, the following values of vertical magnetic centre position of the quadrupole QFR300 for currents k_1 and k_2 are obtained:

$$\begin{aligned} < y_{0,k_1} > = &\ 531 \pm 25 \ \ \mu\text{m}, \\ < y_{0,k_2} > = &\ 427 \pm 47 \ \ \mu\text{m}. \end{aligned} \tag{95}$$

One can see that the magnetic centre of QFR300 moves -104 ± 53 μm for a current variation of 0.39 A that is equal to a Δk of 1.8 m^{-1} as it is derived in Appendix C.1. The obtained $\dot{y}_{mc}$ coefficient is:

$$\dot{y}_{mc} = \frac{< y_{0,k_2} > - < y_{0,k_1} >}{k_2 - k_1} \ = \ (-57 \pm 29) \ \ 10^{-6}\text{m}^2. \tag{96}$$

The results of the magnetic centre stability measurement of the PXMQMAHNAP35 quadrupole magnet differs from that of the QFR300 quadrupole magnet measured at TBL because they differ in many relevant properties such as gradient, length, aperture and lamination thickness, although there are also some similarities such as weight, cooling system and the manufacturer. On the contrary, the QFR800 quadrupole presented in Section 6.1 belongs to the same family of magnets that the QFR300, so that they are equivalent in design. A detailed comparison of the three quadrupoles is given in Appendix C.

6.3.3 Discussion of experimental results

The achieved resolution in the BBA measurements conducted at ATF2 is of the order of the μm. These high resolution measurements allows us to conclude that the motion of the magnetic centre of the ATF2 magnets is less than 1 μm when shunting the quadrupole magnet by ±20%. From both measurement campaigns it can be concluded that FFS dedicated quadrupole magnets at the ATF2 in comparison with the re-cycled CTF3 magnets, show a much better performance in terms of magnetic centre stability.

When comparing the result $\dot{y}_{\text{mc}} = (12.0 \pm 1.2)\ 10^{-6}\ \text{m}^2$ obtained by using a wire to measure the magnetic centre position of the QFR800 magnet, presented in Section 6.1 with the result $\dot{y}_{mc} = (-57 \pm 29)\ 10^{-6}\text{m}^2$ obtained at TBL with a magnet of similar characteristics QFR300, turn out to be quite different. This discrepancy may be caused by the fact that the $\dot{y}_{mc}$ coefficient varies from magnet to magnet due to construction differences. However repetition of magnet measurements to clarify the situation are necessary.

7 Conclusions

In the thesis we have studied the design and optimization of Final Focus System lattice of future lepton linear colliders (LC) and their test facilities. With the aim of achieving the nano-metric scale vertical beam sizes at the IP envisaged in the conceptual designs. Also the convergence of tuning of their FFSs, based on the new local chromaticity correction scheme has been studied, in particular for the Nominal lattice of ATF2 the tuning simulations are compared with experiments. The studies have been done in the framework of the CLIC and ILC projects and scientific programs of the ATF2 and CTF3.

The first problem that has been addressed is the reduction of the luminosity at the IP in the CLIC baseline design. For a FFS with a single crab cavity and the beam crossing angle at the IP equal to 20 mrad the observed luminosity loss is about 5%. We have shown that it is caused by a travelling waist phenomenon induced by the FD sextupoles. The following solutions allowing to recover the LC luminosity have been proposed and analysed in detail:

- Optimization of the crab cavity location, namely placing it in front of the SD4 sextupole,
- Insertion of a second crab cavity 5 m upstream from the original one,
- Keeping the single crab cavity, foreseen in the baseline design, but changing the beam crossing angle to -20 mrad.

These solutions allow an almost full recovery the design luminosity. For this study we have modified the MAPCLASS code by extending it from 5 to 6 variables, so that the longitudinal coordinate can also be included in the simulations and, for example, the travelling waist at the IP can be studied.

The second set of problems studied in the thesis is the design of new ATF2 lattices that minimize the impact of the measured multipole components of the FFS magnets on the IP beam sizes. MAPCLASS with 5 variables has been extensively used together with a code that simulates the beam size measurement with the Shintake monitor. This later code has been developed in the thesis. As a result of the analysis of high order aberrations the following solutions have been proposed:

- Replacing the Final Doublet magnet by a new FD,
- Sorting the ATF2 quadrupole magnets according to their sextupole component,
- Optics modification by increasing the value of β_x^*.

We have shown that the vertical IP beam size of the ATF2 Nominal lattice is recovered by replacing the FD quadrupoles by a new FD and sorting the remaining quadrupole magnets according to their skew sextupole component. An alternative solution for the ATF2 Nominal lattice consists in increasing the IP β_x-function by a factor 2.5. This design, called the ATF2 Bx2.5By1.0 lattice, allows to achieve the vertical IP beam size σ_y^*= 41 nm, however the horizontal one σ_x^* increases by a factor $\sqrt{2.5}$. We conclude that this solution is not the preferred one because the horizontal beam size growth amounts to a luminosity reduction of about 40% for the ILC. The ATF2 Bx2.5By1.0 lattice was used during the ATF2 experimental tuning study that was carried out in December 2010.

In the case of the ATF2 Ultra-low β^* lattice the vertical IP beam size is partially recovered by replacing the FD magnets, sorting the quadrupole magnets according to their skew sextupole component and increasing β_x^* by a factor 3/2 from its nominal value. We have shown that for this new lattice, called

ATF2 Ultra-low β_y^* lattice, the Shintake vertical beam size at the IP is 25.6±0.2 nm. This solution is of interest for the CLIC project because the vertical chromaticity of this lattice is comparable to that of the CLIC 3 TeV design. Consequences of increasing β_x^* in terms of tuning convergence are still to be analysed.

The third set of issues addressed in the present thesis have been the tuning study of the CLIC FFS and ATF2 lattices. In the case of the CLIC the applied tuning algorithm combines a beam based correction and the scan of pre-computed orthogonal knobs. The results obtained for the CLIC BDS with L^*= 6 m show that 97% of the machines achieve 80% of the design luminosity $\mathcal{L}_0$ for the magnetic centre offset value σ_{offset}=3 μm. For larger values of σ_{offset}, the percentage of tuned machines drops dramatically, reaching only 21% for σ_{offset}=10 μm. By comparison with the previous tuning studies of the CLIC BDS baseline design, it has been observed that larger tuning difficulties are observed when increasing the value of L^*. In order to reach the challenging tuning target for CLIC luminosity $\mathcal{L} \geq 1.1\mathcal{L}_0$ for 90% of the machines further improvements of the tuning algorithm are required.
In the case of the ATF2 lattices the studied tuning procedure is based on a set of orthogonal knobs. We have shown that for the ATF2 Bx2.5By1.0 lattice 80% of the machines reach a final vertical beam size at the IP $\sigma_y^* \leq 1.1\sigma_{y0}^*$, where σ_{y0}^* is the design vertical beam size at the IP. The result of simulations has been compared to the experimental one obtained during the ATF2 experimental tuning session in December 2010. The comparison shows that both results are in qualitative agreement within the range that spans from 1.2 μm to 300 nm, however the speed of convergence in the tuning simulations is faster than the experimental one. The tuning simulations in the case of the ATF2 Ultra-low β_y^* lattice show that 80% of the machines reach a final $\sigma_y^* \leq 1.35\sigma_{y0}^*$ with σ_{y0}^*= 25.6 nm. On the basis of the comparison of the results of the tuning simulations for the ATF2 lattices we have concluded that a slower tuning convergence takes place for lattices with larger chromaticity like the ATF2 Ultra-low β_y^*. This result implies that more experimental measurements would be required for larger chromaticity lattices.
With respect to the ATF2, two new lattices the ATF2 Bx2.5By1.0 and ATF2 Ultra-low β_y^* that preserve the design spot sizes have been proposed. The tuning experimental verification of these lattices would validate the feasibility of the FFS based on the local chromaticity correction scheme and in addition the feasibility of higher chromaticity lattices. Presently intense work is ongoing at ATF2, as a result of it in February 2010 it was measured a σ_y^*= 168±2 nm. We hope that in the near future, the design and optimisation methods proposed and developed in the thesis will be used for further reduction of the IP vertical spot size, down to values of 40 nm and even below 30 nm when experiencing with the ultra-low β_y lattice.
Finally, the problem of magnetic centre motion of quadrupoles when using shunting alignments techniques has been addressed in the thesis. The achieved resolution in the BBA measurements conducted at ATF2 is of the order of the μm. On the basis of these high resolution measurements we have concluded that the motion of the magnetic centre of a dedicated FFS quadrupole is less than 1 μm when the strength of the magnet is shunted by ±20%. In addition the beam based alignment measurements carried out at the CTF3 facility have shown the importance of dedicated magnets to meet the challenging magnetic centre motion requirements of a FFS.
However the tuning procedure of the CLIC lattices proposed in the thesis does not allow to reach the envisioned tuning target in terms of percentage of machines nor in terms of the achieved luminosity $\mathcal{L}$ for values of $\sigma_{\text{offset}} \geq 3$ μm. Further improvements of the tuning algorithm are still required, for example the study of the 2^{nd} order tuning knobs should be explored. Nevertheless according to the experimental measurements at ATF2 the assumption of level of misalignment of the FFS magnets by less than 1 μm is justified. This result in combination with possible improvements of the tuning

algorithm may help to reach the challenging tuning goal of CLIC when performing a statistical tuning study that includes the additional errors as tilts and miss-powering of the magnets.
As far as the new ATF2 lattices proposed in the thesis are concerned, it is planned to implement the ATF2 Bx2.5By1.0 design to reach the 38 nm hopefully in the near future. The results on the tolerance calculations for the FD of ATF2 are currently used as a basis for a new FD which is under development at CERN. After replacing the FD at ATF2, the ATF2 Ultra-low β_y^* lattice could be used for experiments with a larger chromaticity lattice. In addition the algorithm for simulating the Shintake measurement developed in the thesis is currently used by the ATF2 collaborators for further studies.
The results obtained in this thesis have been published in the following paper:

- R. Tomás, H. Braun, J.P. Delahaye, E. Marín, D. Schulte, F. Zimmermann, "ATF2 Ultra-Low IP Betas Proposal", Proceedings of PAC'09, Vancouver, May 2009, pp. 2540-2542, `http://accelconf.web.cern.ch/AccelConf/PAC2009/papers/we6pfp024.pdf`.

- G. White,..., E. Marín,..., et al. "Operational Experiences Tuning the ATF2 Final Focus Optics Towards Obtaining a 37 nanometer Electron Beam IP Spot Size", Proceedings of IPAC'10, Kyoto, May 2010, pp. 2383-2385, `http://accelconf.web.cern.ch/AccelConf/IPAC10/papers/weobmh01.pdf`.

- R. Tomás,..., E. Marín,..., et al. "The CLIC BDS Towards the Conceptual Design Report". Proceedings of IPAC'10, Kyoto, May 2010, pp. 3419-3421, `http://accelconf.web.cern.ch/AccelConf/IPAC10/papers/wepe030.pdf`.

- B. Parker,..., E. Marín,..., et al, "A Superconducting Magnet Upgrade of the ATF2 Final Focus", Proceedings of IPAC'10, Kyoto, May 2010, pp.3440-3442, `http://accelconf.web.cern.ch/AccelConf/IPAC10/papers/wepe041.pdf`.

- E. Marin et al. "Scenarios for the ATF2 Ultra-Low Betas Proposal". Proceedings of IPAC'10, Kyoto, May 2010, pp.4554-4556, `http://accelconf.web.cern.ch/AccelConf/IPAC10/papers/thpe020.pdf`.

- Yu.A. Kubyshin,..., E. Marín,..., et al. "Simulations of Emittance Measurement at CLIC", Proceedings of PAC'11, New York, March 2011, pp. 2270-2772, `http://accelconf.web.cern.ch/AccelConf/PAC2011/papers/thp073.pdf`.

- E. Marin et al. "Status of the ATF2 lattices". Proceedings of IPAC'11, San Sebastián. September 2011. pp. 1027-1029, `http://accelconf.web.cern.ch/AccelConf/IPAC2011/papers/tupc016.pdf`.

- G. Sterbini,..., E. Marín,..., et al. "Beam-Based Alignment in CTF3 Test Beam Line". (To be CERN-ATS-2012-144. May 2012. p.4.

- B. Dalena, J. Barranco, A. Latina, E. Marin, J. Pfingstner, D. Schulte, J. Snuverink, R. Tomás and G. Zamudio, "Beam delivery system tuning and luminosity monitoring in the Compact Linear Collider". Phys. Rev. ST Accel. Beams, vol 15, no 5 (2012).

- J. Barranco, E. Marin and R. Tomás, "Luminosity studies in a crab cavity scheme in the CLIC Final Focus." submitted to PRST-AB.

References

[1] P. Kalmus. “Particle physics at the turn of the century”. *CONTEMP. PHYS.* 41, (2000), p. 129.

[2] O. S. Brüning, P. Collier, P. Lebrun, S. Myers, *et al.* “LHC Design Report”. *CERN-2004-003, (2004).* Webpage: `http://lhc.web.cern.ch/lhc/lhc-designreport.html`

[3] A. Datta, B. Mukhopadhyaya, and A. Raychaudhuri. “Physics at the large hadron collider”. *Springer India*, (2011).

[4] S. Khalil and C. Muñoz. “The Enigma of the Dark Matter”. *CONTEMP.PHYS.* 43, (2002), p. 51.

[5] K. A. Olive. “Introduction to supersymmetry: Astrophysical and phenomenological constraints”. *hep-ph/9911307*, (1999), pp. 221–293. Webpage: `http://arxiv.org/pdf/hep-ph/9911307`

[6] L. Linssen, A. Miyamoto, M. Stanitzki, and H. Weerts. “Physics and Detectors at CLIC: CLIC Conceptual Design Report”. *CERN–2012–003*, (2012). Webpage: `https://edms.cern.ch/file/1180032/4/cliccdr_PhysicsDetectors_onlineversion.pdf`

[7] M. Peskin. “Physics of (very) high energy e^+e^- colliders”. *SLAC-Pub-3496*, (1984).

[8] F. Zimmermann. “Beam delivery”. *In: Accelerator Physics and Technologies for Linear Colliders.* Physics 575, (2002). Webpage: `http://hep.uchicago.edu/kwangje/phy575.html`

[9] N. Phinney, N. Toge, and N. Walker. “ILC Reference Design Report Volume 3 - Accelerator”. *arXiv:0712.2361*, (2007). Webpage: `http://www.linearcollider.org/cms/?pid=1000437`

[10] K. Wille. “The physics of particle accelerators: an introduction”. *Oxford University Press, no. 9780198505495*, (1996).

[11] N. J. Walker. “Beam delivery system for pedestrians”. In: 26th Advanced ICFA Beam Dynamics Workshop on Nanometer Size Colliding Beams (Nanobeam 2002), Lausanne, Switzerland, (2002).

[12] O. Napoly. “Beam Delivery System and Beam-Beam Effects”. In: 4^{th} International Accelerator School for Linear Colliders, Beijing, (2009).

[13] P. Lebrun, L. Linssen, A. Lucaci-Timoce, D. Schulte, F. Simon, S. Stapnes, N. Toge, H. Weerts, J. Wells. “The CLIC Programme: towards a staged e+ e- Linear Collider exploring the Terascale, CLIC Conceptual Design Report”. *CERN-2012-005*, (2012), p. 84. Webpage: `https://edms.cern.ch/document/1235960.`

[14] “CLIC Home page”. Webpage: `http://clic-study.org.`

[15] “CTF3 description”. Webpage: `http://ctf3.web.cern.ch/ctf3/New_description.htm.`

[16] P. Raimondi and A. Seryi. “A Novel Final Focus Design for High Energy Linear Colliders”. *Phys. Rev. Lett.* 86, (2001). Webpage: `http://accelconf.web.cern.ch/AccelConf/e00/PAPERS/THP6A11.pdf`

[17] R. Tomás *et al.* "Summary of the BDS and MDI CLIC08 Working Group". *CERN-OPEN-2009-018. CLIC-Note-776*, (2008).

[18] "CLIC BDS lattice repository".
Webpage: `http://clicr.web.cern.ch/CLICr/MainBeam/BDS/v_10_10_11/.`

[19] R. Tomás. "Nonlinear optimization of beam lines". *Phys. Rev. ST Accel. Beams.* 9, (2006), p. 5. Webpage: `http://link.aps.org/doi/10.1103/PhysRevSTAB.9.081001.`

[20] S. Guiducci. "Chromaticity". In: CAS-CERN Accelerator School, CERN-91-04, (1991).

[21] K. L. Brown. "Basic optics of the SLC final focus system". In: International Workshop on the Next Generation of Linear Colliders, Stanford, (1988).

[22] "Final Focus Test Beam: project design report". *SLAC-Note 376*, (1991).

[23] S. Redaelli. "Stabilization of Nanometre-Size Particle Beams in the Final Focus System of the Compact LInear Collider (CLIC)". *Ph.D. Thesis, EPFL*, (2003).

[24] J. Snuverink *et al.* "Status of Ground Motion Mitigation Techniques for CLIC". *EuCARD-CON-2011-034.* (2011).

[25] C. Collette *et al.* "Nano-motion control of heavy quadrupoles for future particle colliders: An experimental validation." *Nucl. Instrum. Methods Phys. Res., A.* 643, EuCARD-PUB-2011-004, (2011), pp. 95–101.

[26] A. Gaddi *et al.* "Dynamic analysis of the final focusing magnets pre-isolator and support system". *LCD-Note-2010-011*, (2010). Webpage: `http://edms.cern.ch/file/1098581/3/LCD-2010-011.pdf`

[27] K. Artoos *et al.* "Status of a study of stabilization and fine position of CLIC quadrupoles to the nanometre level". *EuCARD-CON-2011-030.* (2011).

[28] L. Gatignon. "CLIC MDI overview". *CLIC-Note-937.* (2011), p. 11. Webpage: `http://cdsweb.cern.ch/record/1448256/files/CERN-OPEN-2012-010.pdf?subformat=pdfa`

[29] A. Seryi. "Near IR FF design including FD and longer L* issues". In: CLIC'08 Workshop, Geneva, 14-17 October (2008).

[30] Tomás *et al.* "The CLIC BDS Towards the Conceptual Design Report". In: Proceedings of IPAC'10, Kyoto, May 2010, p. 3419-3421. Webpage: `http://accelconf.web.cern.ch/AccelConf/IPAC10/papers/wepe030.pdf`

[31] G. Zamudio and R. Tomás. "Optimization of the CLIC 500 GeV final focus system and design of a new 3 TeV final focus system with L*=6". *Clic-Note-882*, (2010).

[32] "CLIC BDS L*= 6 m lattice repository".
Webpage: `http://clicr.web.cern.ch/CLICr/MainBeam/BDS/v_10_07_09/`

[33] P. and T. Ehrenfest. "The conceptual foundations of the statistical approach in mechanics". (1959).

[34] T. Shintake. "Proposal of a nanometer beam size monitor for e^+e^- linear colliders". *Nucl. Instr. and Meth. Section A.* 311, no. 3, (1992), pp. 453 - 464. Webpage: `http://www.sciencedirect.com/science/article/pii/016890029290641G`

[35] T. Shintake, H. Hayano, A. Hayakawa, Y. Ozaki, *et al.* "Design of laser Compton spot size monitor". *Int.J.Mod.Phys.Proc.Suppl.* 2A. SLAC-PUB-6098, KEK-PREPRINT-92-65, C92-07-20, (1993), pp. 215-218.

[36] H. Wiedemann. "Particle accelerator physics". *Springer, no. 9783540490432*, (2007)

[37] N. Walker. "Beam-Beam effects". In: Physics and technologies of linear colliders facilities, Santa Barbara, (2003). Webpage: `http://www.desy.de/njwalker/uspas/`

[38] R. Tomás. "MAPCLASS: a code to optimize high order aberrations". *CERN-AB, AB-Note-2006-017 (ABP)*, (2006), p. 4

[39] J. Yan *et al.* "Shintake Monitor Nanometer Beam Size Measurement and Beam Tuning". In: Technology and Instrumentation in Particle Physics 2011 Chicago. Webpage: `http://conferences.fnal.gov/tipp11/.`

[40] M. Sands. "In Physics with intersecting storage rings". ed. by B. Touschek, Academic Press, New York (1971)

[41] Y. Kubyshin *et al.* "Simulations of Emittance Measurement at CLIC". In: Proceedings of PAC'11, New York, March (2011), pp. 2270-2772. Webpage: `http://accelconf.web.cern.ch/AccelConf/PAC2011/papers/thp073.pdf`

[42] "The tracking code PLACET". Webpage: `https://savannah.cern.ch/projects/placet/`

[43] "Guinea-pig++ summary". Webpage: `https://savannah.cern.ch/projects/guinea-pig`

[44] L. Rivkin. "Beamstrahlung and Disruption". In: CAS - CERN Accelerator School : 5th Advanced Accelerator Physics Course, Rhodes, Greece (1993), pp. 557-572.

[45] K. Oide. "Synchrotron-Radiation Limit on the Focusing of Electron Beams". *Phys. Rev. Lett.*, Oct. 61, (1988), pp. 1713–1715. Webpage: `http://link.aps.org/doi/10.1103/PhysRevLett.61.1713`

[46] K. Yokoya and P. Chen. "Beam-beam phenomena in linear colliders". *Frontiers of Particle Beams: Intensity Limitations, Springer Berlin / Heidelberg.* 400, (1992), pp. 415–445. Webpage: `http://dx.doi.org/10.1007/3-540-55250-2_37`

[47] D. Schulte. "Machine-Detector Interface at CLIC". *CERN-PS 2001-002 (AE), CLIC Note-469*, (2001).

[48] M. Jacob and T. T. Wu. "Quantum approach to beamstrahlung". *Physics Letters B.* 197, 1-2, (1987), pp. 253 – 258. Webpage: `http://www.sciencedirect.com/science/article/pii/0370269387903777`

[49] D. Schulte. "Beam-Beam Interaction". In: International Accelerator School for Linear Colliders, Sokendai, Japan (2006).
Webpage: `http://www.linearcollider.org/GDE/school/2006--Sokendai/Program-Calendar`

[50] S. Lee. “Accelerator physics”. *World Scientific, no.9789812562005*, (2004).

[51] K. L. Brown. “A First- and Second-Order Matrix Theory for the Design of Beam Transport Systems and Charged Particle Spectrometers”. *Physical Review D.* , 10, (1968), p. 2738. Webpage: `http://www.osti.gov/energycitations/product.biblio.jsp?osti_id=4492169`

[52] É. Forest. “Beam dynamics: a new attitude and framework”. *Harwood Academic Publishers, no. 9789057025587*, (1998).

[53] É. Forest, E. McIntosh, and F. Schmidt. “Introduction to the polymorphic tracking code: fibre bundles, polymorphic taylor types and "exact tracking"”. *High Energy Accelerator Research Organization, KEK*, (2002).

[54] É. Forest and F. Schmidt. “PTC User’s Reference Manual”. *CERN-BE 2010 report*, (2010). Webpage: `http://frs.web.cern.ch/frs/PTC_reference_manual/PTC_reference_manual.html`

[55] BE/ABP Accelerator Physics Group. “Mad-x home page”. Webpage: `http://frs.home.cern.ch/frs/Xdoc/mad-X.html`

[56] E. Forest and R. D. Ruth. “Fourth-order symplectic integration”. *Physica D: Nonlinear Phenomena.* 43, 1, (1990), pp. 105–117. Webpage: `http://linkinghub.elsevier.com/retrieve/pii/016727899090019L`

[57] F. Becker, W. Coosemans, R. Pittin, and I. Wilson. “An active pre-alignment system and network for CLIC”. *CERN-OPEN-2003-011, CLIC-Note-553*, (2003), p. 77. Webpage: `http://cdsweb.cern.ch/record/604004/files/open-2003-011.pdf`

[58] P. Eliasson, M. S. Korostelev, D. Schulte, R. Tomás, and F. Zimmermann. “Luminosity Tuning at the Interaction Point”. *CERN, CLIC-Note-669 ; EUROTEV-REPORT-2006-039*, (2006). In: 10th European Particle Accelerator Conference, Edinburgh, UK, 26 - 30 Jun 2006, p. 774.

[59] F. Zimmermann. “Tutorial on linear colliders”. *American Institute of Physics*, (2001). , 0-7354-0034-2. Webpage: `http://link.aip.org/link/doi/10.1063/1.1420428`

[60] D. Schulte. “Beam-Beam Simulations with GUINEA-PIG”. *CERN-PS-99-014-LP ; CLIC-Note-387,*, pp. 127-131, (1999). Webpage: `http://cdsweb.cern.ch/record/382453/files/ps-99-014.pdf`

[61] P. Tenenbaum and T. O. Raubenheimer. “Resolution and systematic limitations in beam-based alignment”. *Phys. Rev. ST Accel. Beams, 3*, (2000).

[62] C. Wang and S. U. D. of Applied Physics. “Model independent analysis of beam centroid dynamics in accelerators”. *SLAC-R-547*, (1999). Webpage: `http://www.slac.stanford.edu/pubs/slacreports/slac-r-547.html`

[63] J. A. Nelder and R. Mead. “A Simplex Method for Function Minimization”. *Computer Journal.* 7, (1965), pp. 308–313. Webpage: `http://www.bibsonomy.org/bibtex/2053fb791805bd1debd80a198e8f3e45c/brian.mingus`

[64] Y. Chung, G. Decker, and J. Evans, K. “Closed orbit correction using singular value decomposition of the response matrix”. *Particle Accelerator Conference, Dallas, Texas, (1993)*, pp. 2263 – 2265.

[65] C. Fischer and G. Parisi. "Trajectory Correction Algorithms on the latest Model of the CLIC Main LINAC". *CERN-SL-96-065-BI ; CLIC-Note-315*, (1996), pp. 740-742. Webpage: `http://cdsweb.cern.ch/record/311232/files/sl-96-065.pdf`.

[66] V. Alexandrof *et al.* "Results of final focus test beam". *Particle accelerators and high-energy accelerators.* 4, (1996), pp. 2742–2746. Webpage: `http://hal.in2p3.fr/in2p3-00005387/PDF/in2p3-00005387.pdf`.

[67] ATF International collaboration. "What is the ATF?" Webpage: `http://atf.kek.jp/twiki/bin/view/Main/ATFIntroduction`.

[68] SLAC. "Final focus test beam: project design report". *SLAC-r-376 report*, (1991).

[69] G. J. Roy. "Analysis of the optics of the final focus test beam using Lie algebra based techniques". *SLAC-0397*, (1992), p. 132.

[70] W. Schwartz *et al.* "Wire Measurements for the Control of the FFTB-Magnets", In: 2nd International Workshop on Accelerator Alignment at Hamburg, (1990).

[71] G. Bowden, P. Holik, S. Wagner, G. Heimlinger, and R. Settles. "Precision magnet movers for the Final Focus Test Beam". *Nucl. Instr. and Meth.* 368, 3, (1996), pp. 579 – 592. Webpage: `http://www.sciencedirect.com/science/article/pii/0168900295006931`.

[72] P. G. Tenenbaum, D. Burke, R. Helm, J. Irwin, *et al.* "Beam-based magnetic alignment of the final focus test beam". *SLAC-PUB-6769*, (1995), p. 3.

[73] H. Hayano, J.-L. Pellegrin, S. Smith, and S. Williams. "High resolution BPM for FFTB". *Nucl. Instr. and Meth.* 320, 1–2, (1992), pp. 47 – 52. Webpage: `http://www.sciencedirect.com/science/article/pii/016890029290768Y`.

[74] P. G. Tenenbaum *et al.* "Beam based optical tuning of the final focus test beam". *SLAC-PUB-6770.* (1995), p. 3.

[75] M. Woods, T. Kotseroglou, and T. Shintake. "Vertical position stability of the FFTB electron beam measured by the KEK BSM monitor ". *FFTB Note 98-03 (1998)*, p. 11.

[76] K. Kubo *et al.* "Extremely Low Vertical-Emittance Beam in the Accelerator Test Facility at KEK." *Phys. Rev. Lett.* 88, (2002), p. 4. Webpage: `http://link.aps.org/doi/10.1103/PhysRevLett.88.194801`

[77] H. Braun *et al.* "ATF2 Proposal. Vol. 1". *CERN-AB-2005-035, CLIC-Note-636, DESY-05-148, DESY-2005-148, ILC-ASIA-2005-22, JAI-2005-002, KEK-REPORT-2005-2, SLAC-R-771, UT-ICEPP-2005-02.* (2005), p. 107.

[78] B. Grishanov *et al.* "ATF2 Proposal. Vol. 2". *CERN-AB-2006-004 ; physics/0606194 , DESY-06-001 , DESY-2006-001 , ILC-ASIA-2005-26 , JAI-2006-001 , KEK-2005-9 , SLAC-R-796 , UT-ICEPP-2005-04.* Webpage: `http://hal.in2p3.fr/in2p3-00309474`.

[79] P. Bambade *et al.* "ATF2 Ultra-Low IP Betas Proposal". *CERN-ATS-2009-092. CLIC-Note-792.* (2009), p. 4.

[80] D. Angal-Kalinin *et al.* “Exploring ultra-low β^* values in ATF2 - R&D Programme proposal”. *CARE/ELAN Document-2008-002*, (2008). Webpage: `http://hal.in2p3.fr/in2p3-00308662/en/`.

[81] M. Woodley *et al.* “Coupling correction in ATF2 Extraction Line”. In: Proceedings of PAC’09, Vancouver, (2009), pp. 4314-4316.

[82] H. Hayano. “Wire Scanners for Small Emittance Beam Measurement in ATF”. In: 20th International Linear Accelerator Conference, Monterey, CA, USA, 21 - 25 Aug (2000), pp. 146-148.

[83] A. Faus-Golfe *et al.* “The Multi Optical Transition Radiation System”. *ICFA Beam Dyn. Newslett.* 54, (2011), pp. 96–106.

[84] Y. Renier. “Implementation and validation of the linear collider final focus prototype: ATF2”. *Ph.D. Thesis*, (2010). Webpage: `http://tel.archives-ouvertes.fr/tel-00523218/PDF/Y._Renier.pdf`.

[85] S. Taikan *et al.* “A nanometer beam size monitor for ATF2”. *Nucl. Instr. and Meth.* 616, 1, 2010, pp. 1–8. Webpage: `http://www.sciencedirect.com/science/article/pii/S0168900210002639`.

[86] A. Jérémie. “Installation of FD in September”. In: 7th ATF2 Project Meeting, (2008). Webpage: `http://ilcagenda.linearcollider.org/conferenceDisplay.py?confId=3003`.

[87] B. Bolzon *et al.* “Impact of flowing cooling water on ATF2 FD vibrations”. *ATF-Report 09-01*, (2001).

[88] G. Geschonke and A. Ghigo. “CTF3 Design Report”. *CERN-PS-2002-008-RF, CTF-3-NOTE-2002-047, LNF-2002-008-IR*, (2002).

[89] D. Schulte and I. V. Syratchev. “Considerations on the Design of the Decelerator of the CLIC Test Facility (CTF3)”. *CLIC-Note-634*, (2005), p. 4.

[90] “CTF3 Images”. Webpage: `http://ctf3-tbts.web.cern.ch/ctf3-tbts/images/`.

[91] E. Adli, S. Döbert, R. Lillestol, M. Olvegaard, *et al.* “Commissioning status of the decelerator test beam line in CTF3”. *CERN-ATS-2010-203*, (2010), p. 3.

[92] E. Marin and G. Sterbini. “TBL optics studies and automatic steering”. In: 2nd International Workshop on Future Linear Colliders (LCWS 11), Granada, Spain, (2011).

[93] I. Shinton, G. Burt, C. Glasman, R. Jones, and A. Wolski. “Beam dynamics simulations of the CLIC crab cavity and implications on the BDS”. *Nucl. Instr. and Meth.* 657, 1, (2011), pp. 126–130.

[94] R. PALMER. “Prospects for high energy e^+e^- linear colliders”. *Annu. Rev. Nucl. Part. Sci.* 40, (1990), pp. 529–592.

[95] I. Shinton, G. Burt, C. Glasman, R. Jones, and A. Wolski. “Beam dynamics simulations of the CLIC crab cavity and implications on the BDS”. *Nucl. Instr. and Meth.* 657, 1, (2011), pp. 126–130.

[96] P. Ambattu, G. Burt, A. Dexter, R. Jones, *et al.* "CLIC crab cavity specifications milestone". *EuCARD-REP-2010-003*, (2010).

[97] V. Balakin. "Traveling Focus Regime for Linear Collider VLEPP". Proc. of LC91 Workshop on Linear Colliders, (1991), pp. 330–333.

[98] D. Schulte and R. Tomás. "Beam-Beam Issues in the ILC and in CLIC". *ICFA Beam Dynamics Newsletter.* 52, (2010), pp. 149–165.

[99] A. Seryi. "Crab cavity effects on y-beam size for ILC". Talk in: 3rd CLIC-ILC BDS+MDI meeting, (2005).

[100] J. Barranco. "Luminosity loss in a Crab Cavity scheme". In: International Workshop on future linear colliders Granada (Spain), (2011).

[101] M. Masuzawa. "QEA Magnet Measurements at KEK and Comparison with IHEP Results". In: 11th ATF2 Project meeting (2011). Webpage: `http://ilcagenda.linearcollider.org/conferenceDisplay.py?confId=4904`.

[102] E. Marín. "ATF2 Bx25By1.0 lattice repository". Webpage: `http://clicr.web.cern.ch/CLICr/ATF2/New_Multipoles2/ATF2_Bx25By1`.

[103] E. Marín. "ATF2_Ultra_low_betay lattice repository". Webpage: `http://clicr.web.cern.ch/CLICr/ATF2/New_Multipoles2/ATF2_Ultra_low_betay`.

[104] C. Spencer, R. Sugahara, M. Masuzawa, B. Bolzon, and A. Jeremie. "A project to design and build the magnets for a new test beamline, the ATF2, at KEK". *IEEE Transactions on Applied Superconductivity.* 20, (2010), pp. 250–253. Webpage: `http://hal.in2p3.fr/in2p3-00536399`.

[105] L. Walckiers. "Magnetic measurement with coils and wires". *arXiv:1104.3784*, In: CAS - CERN Accelerator School: Specialised course on Magnets (2011), pp. 357–385. Webpage: `https://cdsweb.cern.ch/record/1340995`.

[106] M. Masuzawa and R. Sugahara. "Field Measurements of the ATF2 Quadrupole Magnets Manufactured by IHEP". *IEEE Transactions on Applied Superconductivity.* 20, (2010), pp. 1969–1972.

[107] M. Masuzawa, K. Egawa, T. Kawamoto, Y. Ohsawa, *et al.* "Installation of skew sextupole magnets at kekb". Proceedings of IPAC'10, Kyoto, (Japan), (2010), pp. 1533–1535. Webpage: `http://accelconf.web.cern.ch/accelconf/IPAC10/papers/tupeb009.pdf`.

[108] M. Woodley. "Repository of the multipole component measurements of the ATF2". Webpage: `http://www.slac.stanford.edu/mdw/ATF2/v4.4`.

[109] E. Marin *et al.* "Scenarios for the ATF2 Ultra-Low Betas Proposal". In: Proceedings of IPAC'10, Kyoto, (2010), pp. 4554-4556. Webpage: `http://accelconf.web.cern.ch/AccelConf/IPAC10/papers/thpe020.pdf`.

[110] B. Parker *et al.* "A superconducting magnet upgrade of the ATF2 final focus". *CERN-ATS-2010-046.* (2010).

[111] A. Vorozhtsov. “A new QF1 magnet for ATF3”. In: International Workshop on Future Linear Colliders, Granada, (Spain), (2011).

[112] B. Parker. “ATF2 magnet field quality”. In: 2nd CLIC-ILC BDS+MDI WG meeting, March, (2010).

[113] E. Marin *et al.* “Status of the ATF2 lattices”. In: Proceedings of IPAC’11, San Sebastián, (2011), pp. 1027-1029. Webpage: `http://accelconf.web.cern.ch/AccelConf/IPAC2011/papers/tupc016.pdf`.

[114] P. G. Tenenbaum. “Lucretia: A Matlab-Based Toolbox for the Modeling and Simulation of Single-Pass Electron Beam Transport Systems”. In: 21st IEEE PAC’05, (2005), p. 4197. Webpage: `http://accelconf.web.cern.ch/accelconf/p05/PAPERS/FPAT086.PDF`.

[115] MAD-8, webpage: `http://frs.web.cern.ch/frs/Xdoc/mad8web/mad8.html`.

[116] G. White and M. Woodley. , Private communication, (2010).

[117] B. Dalena, J. Barranco, A. Latina, E. Marin, *et al.* “Beam delivery system tuning and luminosity monitoring in the Compact Linear Collider”. *Phys. Rev. ST Accel. Beams.* 15, 5, (2012), p. 11. Webpage: `http://link.aps.org/doi/10.1103/PhysRevSTAB.15.051006`.

[118] A. Latina, D. Schulte, and R. Tomás. “Alignment of the CLIC BDS”. In: 11th EPAC’08, Genoa MOPP037, (2008), p. 4.

[119] A. Latina and P. Raimondi. “A novel alignment procedure for the final focus of future linear colliders”. “Linear Accelerator Conference LINAC2010”, MOP026, (2010). pp. 109–111. Webpage: `http://epaper.kek.jp/LINAC2010/html/keyw0061.htm`.

[120] G. White *et al.* “Operational Experiences Tuning the ATF2 Final Focus Optics Towards Obtaining a 37 nanometer Electron Beam IP Spot Size”. In: Proceedings of IPAC’10, Kyoto, (2010), pp. 2383-2385. Webpage: `http://accelconf.web.cern.ch/AccelConf/IPAC10/papers/weobmh01.pdf`.

[121] M. Woodley. “Sumamry of activities, software development and tuning performance pertaining to the extraction line system”. In: 11th ATF2 Project Meeting, (2011).

[122] C. e. a. Rimbault. “Coupling Correction”. In Proceedings of PAC09, FR5PFP005, Vancouver, BC, (Canada), (2008).

[123] J. Alabau-Gonzalvo *et al.* “Optical Transition Radiation System for ATF2”. In: Proceedings of IPAC’11, San Sebastian, (2011), p. 1317. Webpage: `http://epaper.kek.jp/IPAC2011/papers/tupc127.pdf`.

[124] G. White, S. Molloy, and M. Woodley. “Beam-Based Alignment, Tuning and Beam Dynamics Studies for the ATF2 Extraction Line and Final Focus System”. “Proc. of EPAC08”, MOPP039 SLAC-PUB-13303, LAL 08-244. Genoa, Italie, (2008), pp. 634–636. Webpage: `http://hal.in2p3.fr/in2p3-00450236/PDF/mopp039.pdf`.

[125] T. Yamanaka *et al.* “Shintake Monitor in ATF2 : Present Status”. In: Proc. of LCWS/ILC 2010 , (2010).

[126] M. Oroku. "IP-BSM measurement in the 2010 autumn continuous operation". In: 11th ATF2 Project Meeting. Webpage: `http://ilcagenda.linearcollider.org/conferenceDisplay.py?confId=4904.`

[127] J. Yan. "IP-BSM Beamtime Performance and Error Evaluations". In: 14th ATF2 Project Meeting, (2012).

[128] G. Sterbini. "Magnetic measurements of tbl quadrupole". In: CLIC beam physics meeting at CERN on the 25th of April. (2012).

[129] PXMQMAHNAP35 Magnet characteristics.
Webpage: `http://norma-db.web.cern.ch/cern_norma/magnet/idcard/?id=7622.`

[130] QFR800 Magnet characteristics.
Webpage: `https://indico.cern.ch/conferenceDisplay.py?confId=183406.`

[131] C. M. Spencer, D. Anderson, Scott, D. R. Jensen, and Z. R. Wolf. "A rotating coil apparatus with sub-micrometer magnetic center measurement stability". *IEEE Trans. Appl. Supercond.* 16, (2006), pp. 1334–1337.

[132] Alexander and Temnykh. "Vibrating wire field-measuring technique". *Nucl. Instr. and Meth.* 399, 2–3, (1997), pp. 185 – 194. Webpage: `http://www.sciencedirect.com/science/article/pii/S0168900297009728.`

[133] J. García Pérez. Private communication (2011).

[134] L. Fiscarelli, M. Modena, A. Bartalesi, and J. García Perez. Private communication (2012).

[135] S. Boogert, R. Ainsworth, G. Boorman, S. Molloy, and M. "Cavity beam position monitor system for ATF2". , IPAC2010, 227579, (2010), pp. 1140–1142. Webpage: `http://webbuild.knu.ac.kr/ accelerator/ppt/mope070.pdf.`

[136] A. Bellomo, C. d. Lira, B. Lam, D. MacNair, and G. White. "ATF2 High Availability Power Supplies". In: 11$^{\text{th}}$ EPAC'08, Genoa, Italy, (2008).

[137] PXMQMAHNAP35 Magnet characteristics.
Webpage: `http://norma-db.web.cern.ch/cern_norma/magnet/idcard/?id=1755.`

[138] F. Toral *et al.* "Design, Manufacturing and Tests of a Micrometer Precision Mover for CTF3 Quadrupoles". In: 11$^{\text{th}}$ EPAC'08, Genoa (2008), p. 3. Webpage: `http://accelconf.web.cern.ch/AccelConf/e08/papers/tupd040.pdf.`

[139] J. J. García Garrigós. "Design and Construction of a Beam Position Monitor Prototype for the Test Beam Line of the CTF3". *CERN CLIC-Note-769*, (2008). Webpage: `http://cdsweb.cern.ch/record/1164156/files/CERN-OPEN-2009-002.pdf.`

[140] S. Turner and E. O. for Nuclear Research. "CAS, CERN Accelerator School: fifth general accelerator physics course". *Proc. University of Jyväskylä, Finland, 7-18 September 1992*, (1994).

Appendices

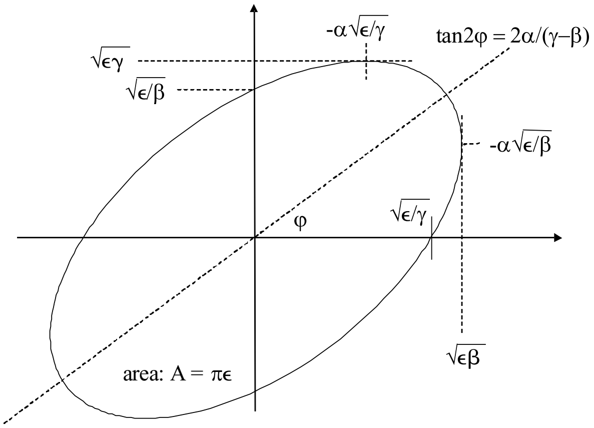

Figure 77: Phase space ellipse. The axis (u, u') correspond either to (x, x') or (y, y') or (z, z'). (Figure taken from [140]).

A Beam dynamics

A.1 Beam emittance

The beam emittance ϵ is defined as A/π where A is the area of the region occupied by the particles of a beam in the phase space which is usually enclosed by an ellipse, see Fig. 77. It is called phase space ellipse and its equation is given by the following relation:

$$\gamma_u(s)u^2 + 2\alpha_u(s)uu' + \beta_u(s)u'^2 = \epsilon_u \tag{97}$$

where u=x, y or z coordinates. The β, α and γ are the ellipse parameters or Twiss parameters [10] that determine the shape and orientation of the ellipse along the s coordinate. Figure 77 shows the relation between the emittance and the Twiss functions at a given location in the machine.

A.2 Magnetic field of guiding magnets

Bending, quadrupole and sextupole magnets are extensively used accelerator components for transporting the beam throughout a machine. The dipole, quadrupole and sextupole magnetic fields in these magnets are described by the following formulas:

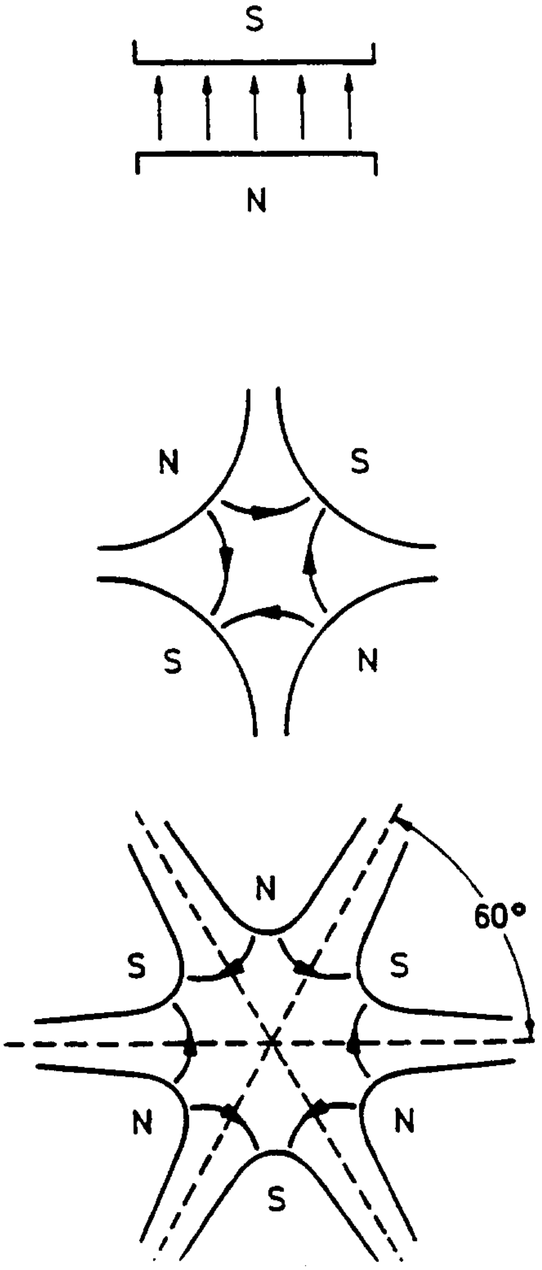

Figure 78: Yoke profiles of a bending (upper plot), normal quadrupole (middle plot) and normal sextupole (lower plot) magnets. (Figure taken from [140]).

Bending magnet

$$B_x = 0 \tag{98}$$

$$B_y = B_0 \;\text{ where }\quad B_0 = \frac{\mu_0 n_c I}{h} \tag{99}$$

$$\rho_r = \frac{B_0}{p/e}. \tag{100}$$

There h is the gap between the poles and ρ_r is the bending radius.

Normal quadrupole magnet

$$B_x = -gy \tag{101}$$

$$B_y = -gx \;\text{ where }\quad g = \frac{2\mu_0 n_c I}{R_c^2} \tag{102}$$

$$K = \frac{g}{p/e}, \tag{103}$$

R_c is the shortest distance from the quadrupole center to the pole face, g and K are the gradient and the normalised gradient of the quadrupole, respectively.

Normal sextupole magnet

$$B_x = s \cdot xy \tag{104}$$

$$B_y = -\frac{s}{2} \cdot (x^2 - y^2) \;\text{ where }\; s = \frac{6\mu_0 n_c I}{R_s^3} \tag{105}$$

$$K_s = \frac{s}{p/e}, \tag{106}$$

R_s is the distance from the sextupole center to the pole face, s and K_s are the gradient and the normalised gradient of the sextupole, respectively.

In the formulas above μ_0 is the permeability, n_c is the number of turns of the coils which transport the current I, p is the particle momentum and e is the electron charge. The normalisation factor p/e is usually referred to as the magnetic rigidity, in case of relativistic electrons it is equal to:

$$p/e = B\rho_r, \tag{107}$$

where ρ_r is the bending radius.

A.3 Matrix representation of linear accelerator components

The transport matrix (R) of the linear elements of an accelerator are the following:

Drift space

The linear map of a drift space or field free region of length l_d is given by the following R_d matrix:

$$\begin{pmatrix} u \\ u' \end{pmatrix}_{s+l_d} = R_d \begin{pmatrix} u \\ u' \end{pmatrix}_s = \begin{pmatrix} 1 & l_d \\ 0 & 1 \end{pmatrix} \begin{pmatrix} u \\ u' \end{pmatrix}_s .$$

Bending magnet

The map of a bending magnet of length l_b and bending radius ρ_c is given by R_b as follows:

$$\begin{pmatrix} u \\ u' \end{pmatrix}_{s+l_b} = R_b \begin{pmatrix} u \\ u' \end{pmatrix}_s = \begin{pmatrix} \cos(\frac{l_b}{\rho_c}) & \rho_c \sin(\frac{l_b}{\rho_c}) \\ -\frac{1}{\rho_c}\sin(\frac{l_b}{\rho_c}) & \cos(\frac{l_b}{\rho_c}) \end{pmatrix} \begin{pmatrix} u \\ u' \end{pmatrix}_s .$$

Normal quadrupole magnet

The maps of a focusing and defocusing quadrupole magnets of length l_q and normalised gradient K are given by $R_{q,f}$ and $R_{q,d}$ respectively, as:

$$\begin{pmatrix} u \\ u' \end{pmatrix}_{s+l_q} = R_{q,f} \begin{pmatrix} u \\ u' \end{pmatrix}_s = \begin{pmatrix} \cos(l_q\sqrt{K}) & \frac{1}{\sqrt{K}}\sin(l_q\sqrt{K}) \\ -\sqrt{K}\sin(l_q\sqrt{K}) & \cos(l_q\sqrt{K}) \end{pmatrix} \begin{pmatrix} u \\ u' \end{pmatrix}_s$$

$$\begin{pmatrix} u \\ u' \end{pmatrix}_{s+l_q} = R_{q,d} \begin{pmatrix} u \\ u' \end{pmatrix}_s = \begin{pmatrix} \cosh(l_q\sqrt{K}) & \frac{1}{\sqrt{K}}\sinh(l_q\sqrt{K}) \\ \sqrt{K}\sinh(l_q\sqrt{K}) & \cosh(l_q\sqrt{K}) \end{pmatrix} , \begin{pmatrix} u \\ u' \end{pmatrix}_s .$$

In the thin lens approximation ($l_q \to 0,\ Kl_q = k$ finite) the matrices $R_{q,f}$ and $R_{q,d}$ are given by:

$$R_{q,f}^{l\to 0} = \begin{pmatrix} 1 & 0 \\ -k & 1 \end{pmatrix} \quad \text{and} \quad R_{q,d}^{l\to 0} = \begin{pmatrix} 1 & 0 \\ k & 1 \end{pmatrix} .$$

B Magnetic centre measurements at ATF2

In this section the plots of the obtained $\dot{y}_{\mathrm{mc}}$ coefficients for each orbit of the three measurements at ATF2 discussed in Section 6.3.1 are shown. Each plot of Fig. 79 contains the values of $\dot{y}_{\mathrm{mc}}$ calculated for the different trajectories obtained either by shunting the previous quadrupole magnet or by moving the quadrupole magnet itself. The computed results are summarised in Table 25.

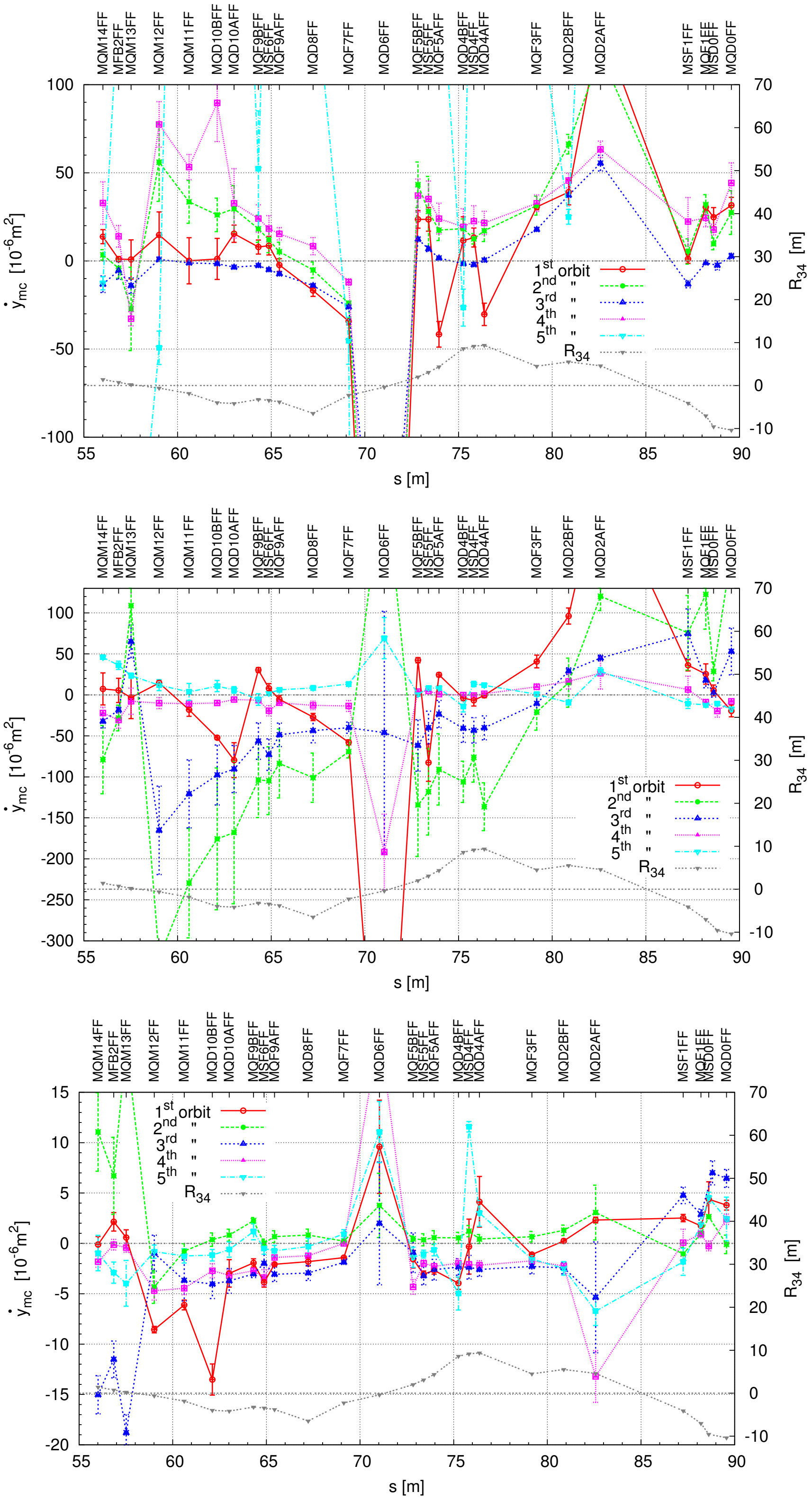

Figure 79: Obtained $\dot{y}_{\rm mc}$ coefficients for the 1st, 2nd and 3rd measurements.

	Unit	QFR300	QFR800	PXMQMAHNAP35
Function		Normal	Normal	Normal
Cooling system		air	air	air
Aperture width	[mm]	38.0	38.0	58.0
Aperture height	[mm]	38.0	38.0	58.0
Iron length	[mm]	170.0	170.0	104.0
Magnetic length	[mm]	193.3	193.3	120.0
Total width	[mm]	317.0	317.0	274.0
Total height	[mm]	236.0	236.0	274.0
Weigth	[Kg]	50	50	51
Lamination thickness	[mm]	0.65	0.65	1.5
Peak current	[A]	8.0	8.0	10.0
RMS current	[A]	8.0	8.0	10.0
Number of turns per pole		128	128	85
Resistance 20 °C	[mΩ]	1000	1000	340
Gradient at peak current	[T/m]	7.14	7.14	2.5
Integrated Gradient at peak current	[T]	1.38	1.38	0.3

Table 26: Main characteristics of the QFR300, QFR800 and PXMQMAHNAP35 quadrupole magnets.

C Magnets characteristics

Table 26 compares the main characteristics of the QFR300, QFR800 and the PXMQMAHNAP35 quadrupole magnets used in the beam based alignment study discussed in Section 6.3.2.

C.1 Conversion from current to gradient

In order to compare the $\dot{y}_{\text{mc}}$ coefficient for different magnets, it is necessary to convert the current intensity of the magnet (I) into integrated normalised strength (k). The results of the measurements of the magnetic field of the QFR300, QFR800 and PXMQMAHNAP35 quadrupole magnets for several currents, discussed in Section 6.3.2, are reported in [129], [130] and [137] respectively. The integrated gradient ($g \cdot l_q$) is the slope of the red, green and blue curves of Fig. 80. The results of the linear interpolation of the data are the following:

$$\text{QFR300}: \; gl_{\text{QFR300}} = 0.1657 \pm 0.0004 \text{ T} \tag{108}$$

$$\text{QFR800}: \; gl_{\text{QFR800}} = 0.1599 \pm 0.0005 \text{ T} \tag{109}$$

$$\text{HNAP35}: \; gl_{\text{HNAP35}} = 0.03128 \pm 0.00002 \text{ T} \tag{110}$$

Assuming that the TBL beam energy (E) is about 111 MeV the integrated normalised gradient is obtained by using Eq. (103). One gets:

$$\text{QFR300}: \; k_{\text{QFR300}} = 0.448 \pm 0.001 \text{ m}^{-1} \tag{111}$$

$$\text{QFR800}: \; k_{\text{QFR800}} = 0.432 \pm 0.0013 \text{ m}^{-1} \tag{112}$$

$$\text{HNAP35}: \; k_{\text{HNAP35}} = 0.08450 \pm 0.00005 \text{ m}^{-1} \tag{113}$$

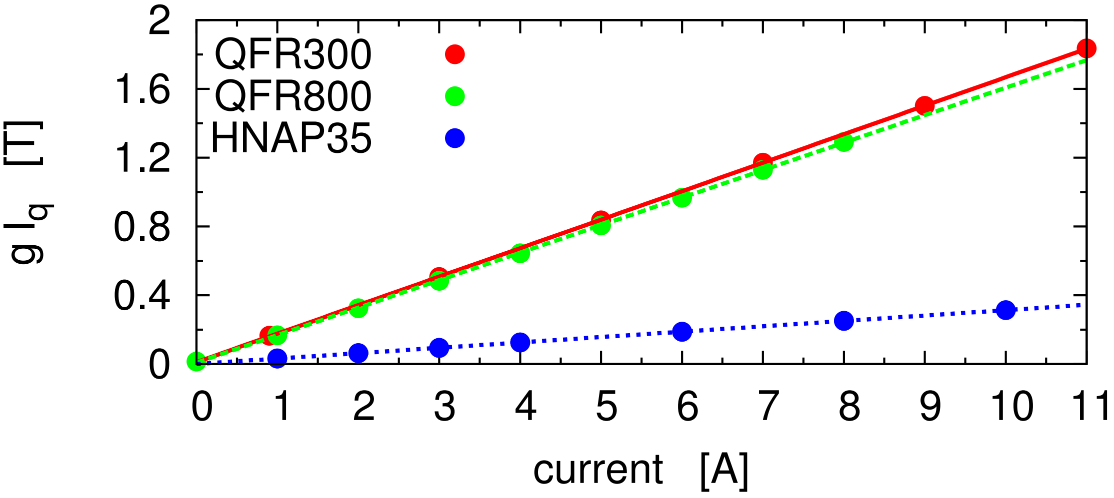

Figure 80: Integrated gradient versus quadrupole current. Red, green and blue dots show the measurement of the magnetic field of the QFR300, QFR800 and PXMQMAHNAP35 (HNAP35) quadrupole magnets respectively as a function of the current of the magnet.